

Study on Energy Storage and Electrocaloric Effect of  
NaNbO<sub>3</sub> Based Ceramics

Tao Zhang

June 2022

Department of Intelligent Systems Design Engineering  
Toyama Prefectural University

## ABSTRACT

Sodium niobate (NN)-based lead-free ceramics are regarded as promising candidates in energy storage area due to their anti-ferroelectricity and high polarization values. However, the low energy storage density and unstable anti-ferroelectric (AFE) phase restrict the further applications. Therefore, stabilizing the AFE phase and enhancing energy storage properties in NN-based ceramics are the cornerstones for further development of NN-based ceramics.

In addition, the phase structure of NN ceramics is still under debate. Therefore, based on previous theoretical research and the unique characteristics, it is also referred to as AFE phase herein.

This research is divided into four main parts. First, AFE phase was stabilized in  $\text{NaNbO}_3\text{-La}(\text{Nb}_{1/3}\text{Mg}_{2/3})\text{O}_3$  (NN-LNM) binary bulk ceramics, achieving improved recoverable energy storage density ( $W_{\text{rec}}$ ) at room temperature (RT) (Chapter 3). Second,  $\text{MnO}_2$  was introduced as an effective additive to improve  $W_{\text{rec}}$  and thermal stability of the NN-LNM binary ceramics (Chapter 4). Third,  $\text{CaZrO}_3$  (CZ) was applied to form ternary NN-LNM-CZ ceramics with higher efficiency ( $\eta$ ) and  $W_{\text{rec}}$  at RT (Chapter 5). In addition, the phase diagrams and electrocaloric effect (ECE) were investigated (Chapter 6). Chapter 7 is the conclusion.

$\text{La}(\text{Nb}_{1/3}\text{Mg}_{2/3})\text{O}_3$  (LNM) with a lower theoretical tolerance factor  $t$  (0.93230) could form solid solutions with NN. The  $t$  was reduced from 0.96707 to 0.96525 when LNM amount increased from 0 to 5.25%. The width of hysteresis loops (WHL) was well narrowed and the breakdown electric field strength ( $E_b$ ) was also improved. As a result, the energy storage properties with  $W_{\text{rec}}$  of  $1.45 \text{ J/cm}^3$  and  $\eta$  of 69.6% were achieved for 0.955NN-0.045LNM ceramics.

Sintering aid  $\text{MnO}_2$  is commonly used to improve the sintering performance of lead-based and lead-free materials because of its lower melting point and sliding valences. When 1.5%  $\text{MnO}_2$  was added in 0.955NN-0.045LNM ceramics, the optimum sintering temperature was reduced from  $1270 \text{ }^\circ\text{C}$  to  $1220 \text{ }^\circ\text{C}$ , while the relative density

was improved from 98.36% to 98.98%. Accordingly, the  $E_b$  value was improved from 18.7 kV/mm to 25.2 kV/mm. As a result,  $W_{\text{rec}}$  of 2.58 J/cm<sup>3</sup> with  $\eta = 66.8\%$  was obtained at RT when 1.5% MnO<sub>2</sub> was employed. It also presented attractive thermal stability in energy storage at 30-60 °C, revealing a slight reduction of 4.86% and 2.75% for  $W_{\text{rec}}$  and  $\eta$ , respectively.

As the  $\eta$  is inversely proportional to the WHL, CZ was exploited to construct (0.955- $z$ )NN-0.045LNM- $z$ CZ ternary systems in order to improve  $\eta$ . As CZ was applied,  $\eta$  rapidly increased from 69.6% to over 80% with reduced WHL. The optimum  $W_{\text{rec}}$  of 1.90 J/cm<sup>3</sup> with  $\eta$  of 84.5% was obtained for 0.945NN-0.045LNM-0.01CZ ceramics under a low electric field of 21.3 kV/mm.

Both the binary NN-LNM and ternary NN-LNM-CZ systems were investigated for the first time. It is essential to construct the phase diagrams, which are used for energy storage investigation. Within the AFE range, a reduction in tolerance factor was beneficial for the improvement of  $\eta$  through narrowing the WHL. In addition, a special phenomenon was observed, revealing as a coexistence of positive ECE and negative ECE, which was only found in a few materials. The optimum negative ECE was observed at 60 °C with the temperature change ( $\Delta T$ ) of -1.48 K for 0.955NN-0.045LNM ceramics, while the best positive ECE ( $\Delta T = 1.42$  K) was observed at 110 °C.

As a conclusion, the optimum  $W_{\text{rec}}$  of 2.58 J/cm<sup>3</sup> with  $\eta = 66.8\%$  was obtained for 1.5% MnO<sub>2</sub> doped 0.955NN-0.045LNM ceramics. The attractive  $\eta$  of 84.5% with  $W_{\text{rec}}$  of 1.90 J/cm<sup>3</sup> was achieved for 0.945NN-0.045LNM-0.01CZ ceramics. Meanwhile, the ECE with negative  $\Delta T = -1.48$  K and positive  $\Delta T = 1.42$  K was observed for 0.955NN-0.045LNM ceramics. And, the phase diagrams for energy storage were summarized. Overall, this study has opened up a new ceramic system for energy storage and solid refrigeration equipment.

**Keywords:** NaNbO<sub>3</sub>-based ceramics, lead-free, energy storage, electrocaloric effect, phase transition, thermal hysteresis, anti-ferroelectric phase

# Contents

<b>Chapter 1 Introduction.....</b>	<b>1</b>
1.1 Background and Significance of Research.....	1
1.2 Energy Storage Principles .....	3
1.2.1 Ferroelectricity and anti-ferroelectricity .....	3
1.2.2 Principle and calculation of energy storage property.....	4
1.2.3 The influencing factors of energy storage property .....	6
1.3 Energy Storage Dielectric Capacitors .....	8
1.3.1 Relaxor-ferroelectrics.....	10
1.3.2 Para-electrics.....	12
1.3.3 Anti-ferroelectrics .....	12
1.4 The Research Status of NaNbO <sub>3</sub> -Based Energy Storage Ceramics .....	13
1.4.1 Crystal structure of NaNbO <sub>3</sub> ceramics.....	13
1.4.2 Phase transition behavior of NaNbO <sub>3</sub> ceramics.....	15
1.4.3 Modification of NaNbO <sub>3</sub> -based energy storage ceramics.....	16
1.5 Electrocaloric Effect and Research Status.....	18
1.5.1 The refrigeration principle of electrocaloric effect .....	18
1.5.2 Development of electrocaloric effect.....	20
1.6 Thesis Objectives and Organization .....	20
1.6.1 Thesis objectives .....	20
1.6.2 Thesis organization .....	22
References .....	23
<b>Chapter 2 Experiment and Characterization.....</b>	<b>30</b>
2.1 Preparation of NaNbO <sub>3</sub> -Based Bulk Ceramics .....	30
2.1.1 Experimental reagent .....	30
2.1.2 Preparation of ceramics by a solid-state method .....	30
2.1.3 Electrode preparation .....	31
2.2 Characterization.....	32
2.2.1 Measurement of particle size distribution.....	32

2.2.2 Density determination .....	32
2.2.3 X-ray diffraction (XRD) analysis .....	33
2.2.4 Scanning electron microscope (SEM) analysis.....	34
2.2.5 Temperature-dependent dielectric performance measurement .....	34
2.2.6 Frequency-dependent dielectric performance measurement .....	34
2.2.7 Conductivity measurement .....	35
2.2.8 Ferroelectricity measurement.....	35
References .....	36
<b>Chapter 3 Preparation and Study of <math>\text{NaNbO}_3\text{-La}(\text{Nb}_{1/3}\text{Mg}_{2/3})\text{O}_3</math> Ceramics.....</b>	<b>37</b>
3.1 Introduction .....	37
3.2 Performance of $\text{NaNbO}_3\text{-La}(\text{Nb}_{1/3}\text{Mg}_{2/3})\text{O}_3$ Ceramics.....	38
3.2.1 Sintering performance of NN-LNM ceramics .....	38
3.2.2 Phase structure and microstructure of NN-LNM ceramics.....	41
3.2.3 Dielectric and phase transition behavior of NN-LNM ceramics .....	43
3.2.4 Energy storage performance of NN-LNM ceramics.....	48
3.3 Influences of Tolerance Factor on Phase Transition in Another System.....	53
3.4 Summary .....	54
References .....	56
<b>Chapter 4 Effect of <math>\text{MnO}_2</math> Dopant on Properties of NN-LNM Ceramics.....</b>	<b>58</b>
4.1 Introduction .....	58
4.2 Performance of $\text{MnO}_2$ -Doped NN-LNM Ceramics .....	59
4.2.1 Effect of $\text{MnO}_2$ dopant on sintering performance.....	59
4.2.2 Effect of $\text{MnO}_2$ dopant on phase structure and microstructure.....	62
4.2.3 Effect of $\text{MnO}_2$ dopant on dielectric and phase transition behavior .....	64
4.2.4 Effect of $\text{MnO}_2$ dopant on energy storage properties .....	68
4.3 Summary .....	73
References .....	74
<b>Chapter 5 Preparation of <math>\text{NaNbO}_3\text{-La}(\text{Nb}_{1/3}\text{Mg}_{2/3})\text{O}_3\text{-CaZrO}_3</math> Ceramics.....</b>	<b>76</b>
5.1 Introduction .....	76
5.2 Performance of Ternary NN-LNM-CZ Ceramics .....	77

5.2.1 Sintering performance of NN-LNM-CZ ceramics.....	77
5.2.2 Phase structure and microstructure of NN-LNM-CZ ceramics .....	79
5.2.3 Dielectric and phase transition behavior of NN-LNM-CZ ceramics.....	81
5.2.4 Energy storage performance of NN-LNM-CZ ceramics .....	85
5.2.5 Energy storage efficiency under unipolar electric field .....	91
5.3 Summary .....	92
References .....	94
<b>Chapter 6 Electrocaloric Effect and Phase Diagram.....</b>	<b>96</b>
6.1 Introduction .....	96
6.2 Construction of Phase Diagram.....	97
6.3 Electrocaloric Effect of NaNbO <sub>3</sub> -Based Ceramics.....	101
6.3.1 Electrocaloric effect of 4.5LNM ceramics.....	101
6.3.2 Electrocaloric effect of 1.5MnO <sub>2</sub> ceramics.....	102
6.3.3 Electrocaloric effect of 1.0CZ ceramics .....	103
6.4 Summary .....	105
References .....	107
<b>Chapter 7 Conclusions.....</b>	<b>109</b>
<b>Acknowledgements .....</b>	<b>112</b>
<b>List of Publications .....</b>	<b>113</b>

# Chapter 1

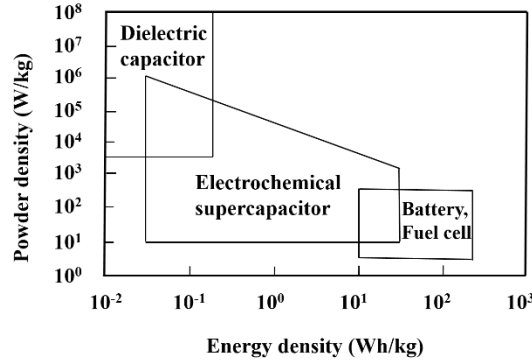
## Introduction

### 1.1 Background and Significance of Research

Due to the rapid development of economy, the environmental problems such as air pollution and global warming are becoming more serious. Therefore, various new energy generation technologies such as solar energy, wind energy and thermal energy are urgently needed, to reduce the dependency on fossil-based energy reserves.<sup>[1]</sup> Generally, the successful production, distribution as well as storage of electricity are the cornerstone for the development and growth of society and technology in years to come. This will lead to the high demand for devices for effectively storing, absorbing, and supplying the electricity.<sup>[2]</sup> Significantly, equal importance is being directed to the development of suitable technologies for efficient storage and distribution of electricity.

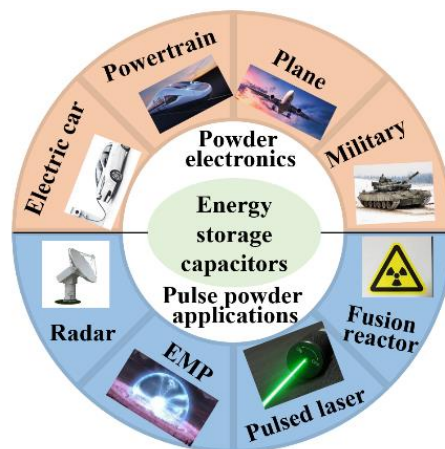
Usually, commercial energy storage devices are divided into four main categories: fuel cells, chemical batteries, electrochemical supercapacitors and dielectric capacitors, as shown in Fig. 1-1.<sup>[1-7]</sup> Among them, fuel cells and chemical batteries possess a lower power density ( $< 500$  W/kg) due to the limitation of charge-carrier moving speed, although their energy density (for instance, that of fuel cells and chemical batteries are 200-1000 and 10-300 W·h/kg, respectively) is much higher.<sup>[1,2]</sup> Electrochemical supercapacitors can supply moderate energy density (0.04-30 W·h/kg) and power density ( $10-10^6$  W/kg), while the charge and discharge processes still need several seconds or more.<sup>[3,4]</sup> Meanwhile, dielectric capacitors possess higher power density ( $> 10^8$  W/kg), extremely fast charge-discharge speed (milliseconds or microseconds).<sup>[5-7]</sup> Recently, most efforts have been channeled to thin-film-based dielectric capacitors due to their superior energy storage density. However, the poor thermal stability and energy capacity restrict their practical applications.<sup>[8,9]</sup> Therefore, ceramic-based dielectric

capacitors are of high concern in recent years, and the energy density of commercial products needs significant improvement to meet the wide demands.



**Fig. 1-1** Powder density and energy density of common energy storage devices.<sup>[1-7]</sup>

Dielectric capacitors are widely applied as passive components in many electronic devices (Fig. 1-2).<sup>[10,11]</sup> They are used to carry out a host of functions in pulse power and power electronic applications in which a low-power, long-time input is transferred into a high-power and short-time output.<sup>[10,11]</sup> These applications include medical defibrillators, transversely excited atmospheric lasers, advanced electromagnetic systems, weapon systems as well as hybrid electric vehicles. Nowadays, the driving force in the applications of capacitors has been attributed to the significantly boomed consumer electronic market.<sup>[11]</sup>



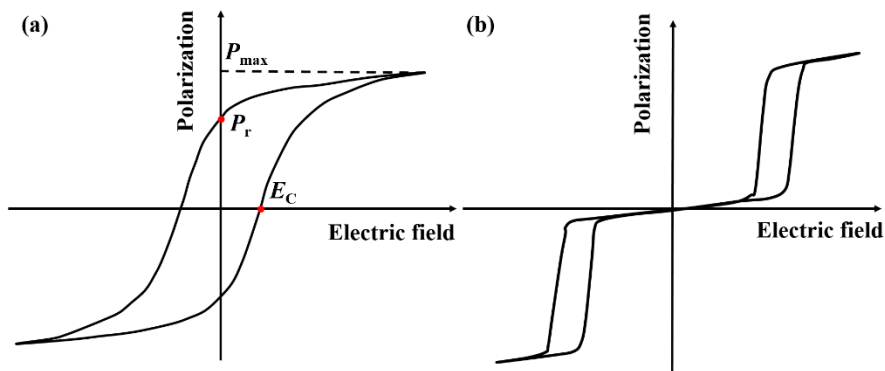
**Fig. 1-2** Wide applications of dielectric capacitors.<sup>[10,11]</sup>



## 1.2 Energy Storage Principles

### 1.2.1 Ferroelectricity and anti-ferroelectricity

The ferroelectric (FE) materials are polarized when an external electric field ( $E$ ) is applied due to the crystal asymmetric aspects.<sup>[12]</sup> The polarization strength ( $P$ ) is directly related to  $E$  strength, which is described by hysteresis  $P$ - $E$  loops, as displayed in Fig. 1-3(a). There exists spontaneous polarization in different directions and the small regions with same direction refer to as the ferroelectric domains.<sup>[13,14]</sup> After the electric field is applied, the domains tend to be orientated in the direction parallel to the external electric field with an increase in polarization value. However, upon the arrangement of all domains, the polarization value reaches its maximum ( $P_{\max}$ ). Meanwhile, when the electric field is withdrawn, the polarization cannot immediately return to the original state but remains in a macroscopic polarization state (defined as residual polarization,  $P_r$ ).<sup>[13]</sup> Furthermore, the corresponding electric field strength, which is the point where the polarization state returns to zero referred to as the coercive electric field ( $E_c$ ).<sup>[13]</sup>



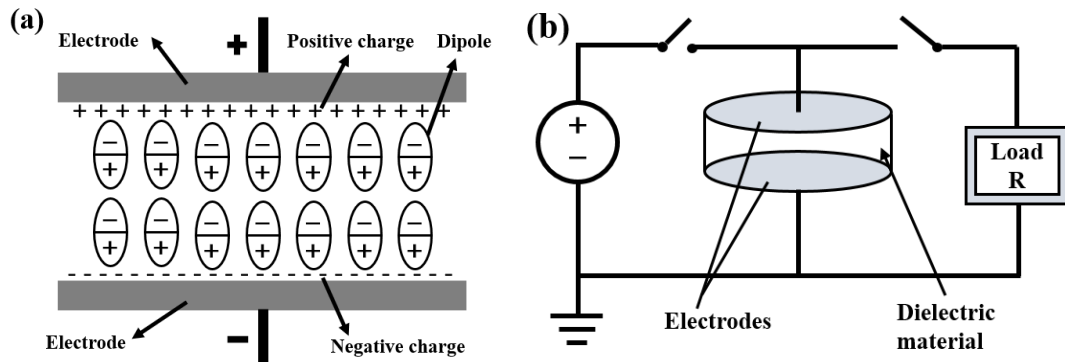
**Fig. 1-3** Schematic representation of hysteresis loop for (a) ferroelectric ceramics<sup>[12]</sup>, (b) double hysteresis loop<sup>[15]</sup>.

Anti-ferroelectric (AFE) material belongs to a class of FEs with similar crystal structure and free-energy, where the dipoles in the same domains are antiparallel. Thus,

AFEs demonstrate no residual polarization in the macro view.<sup>[15,16]</sup> When a strong external electric field is employed, the AFE phase is transformed to FE phase, producing a typical double  $P$ - $E$  loops (Fig. 1-3(b)).<sup>[15,16]</sup> Although the definition and mechanism of anti-ferroelectricity are still vague without unified standards, the unique characteristics of AFEs are attractive for energy storage.

### 1.2.2 Principle and calculation of energy storage property

The energy storage ceramics can be simply understood as capacitors that are composed of two parallel electrodes and internal insulating materials. The internal bound charges (dipoles) will deviate from original equilibrium location and orientate along the direction of electric field when an external electric field is applied (Fig. 1-4). This is referred to as the polarization process, in which electric energy is stored in the capacitors through binding of charges on the surface of capacitors. The polarization mechanism is divided into four categories including dipole polarization, ion polarization, electron polarization, and space charge polarization.<sup>[17-20]</sup>



**Fig. 1-4** (a) Schematic of dielectrics between electrodes where dipoles are oriented and polarized with respect to external electric field, (b) circuit diagram of dielectric capacitors.<sup>[20]</sup>

Dipole polarization is produced by oriented arrangement of permanent dipoles aligned in the direction of external electric field, which is called molecular polarization. This contributes a lot to the polarization process; however, a relatively long response

time of  $10^{-9}$  s is produced with a frequency range of  $10^3$ - $10^8$  Hz. The polarization derived from electron clouds deformation under an electric field is called ion polarization, which responds much faster with response time and frequency of  $10^{-13}$  s and  $10^9$ - $10^{13}$  Hz, respectively. Electron polarization is caused by the misalignment of atomic nucleus and extra-nuclear electron centers. It possesses the fastest response time of  $10^{-15}$  s and highest frequency of  $10^{14}$ - $10^{16}$  Hz, while a little influence is returned to the polarization process. The charges located at the interface migrate directionally under the influence of external electric field, leading to a space-charged polarization (internal polarization) and the slowest response time of  $10^{-4}$ - $10^4$  s coupled with lowest frequency of  $10^{-5}$ - $10^2$  Hz.

For nonlinear dielectric capacitors (Fig. 1-5), when an electric field  $E$  is applied, the stored electric energy can be calculated using the Eq. (1-1):<sup>[21,22]</sup>

$$W = \int E dD \quad (1-1)$$

where  $D$  is the electric displacement.

For dielectric capacitors,  $D$  is a function of  $E$  and  $P$  as shown in the Eq. (1-2):<sup>[21,22]</sup>

$$D = \varepsilon_0 E + P \quad (1-2)$$

And  $P$  is dependent on  $E$  and susceptibility ( $\chi_e$ ):<sup>[21,22]</sup>

$$P = \varepsilon_0 \chi_e E = \varepsilon_0 (\varepsilon_r - 1) E \quad (1-3)$$

where,  $\varepsilon_r$  and  $\varepsilon_0$  ( $8.85 \times 10^{-12}$  F/m) are dielectric constant of capacitors and vacuum, respectively.

For dielectric materials,  $\varepsilon_r \gg 1$ , means:

$$D = \frac{P}{\varepsilon_r - 1} + P \approx P \quad (1-4)$$

Therefore, the energy density can be computed as:

$$W = \int E dP \quad (1-5)$$

Based on the aforementioned, the charged energy storage density ( $W_{ch}$ , J/cm<sup>3</sup>) can be calculated with the integral of  $P$ - $E$  loops:

$$W_{ch} = \int_0^{P_{max}} E dP \quad (1-6)$$

For nonlinear dielectric materials, the thermal hysteresis is inevitable; the relationship between  $P$  and  $E$  is also nonlinear. Thus, the recoverable energy storage

density ( $W_{rec}$ , J/cm<sup>3</sup>) can be calculated through the integral of  $P$ - $E$  loops:

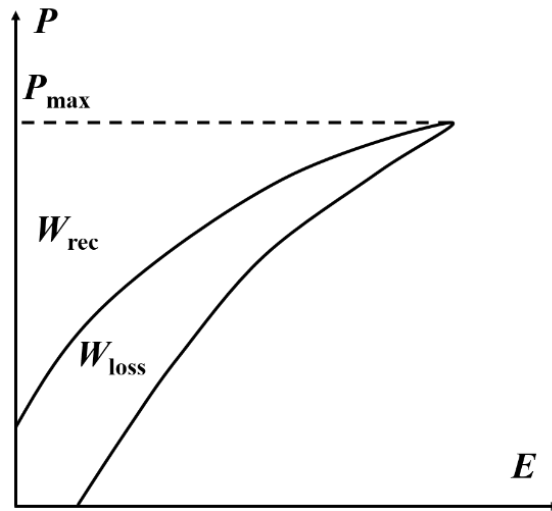
$$W_{rec} = \int_{P_r}^{P_{max}} E dP \quad (1-7)$$

As a result, the energy loss ( $W_{loss}$ , J/cm<sup>3</sup>) and energy storage efficiency ( $\eta$ ) can be expressed as follows:

$$W_{loss} = W_{ch} - W_{rec} \quad (1-8)$$

$$\eta = \frac{W_{rec}}{W_{ch}} \times 100\% \quad (1-9)$$

The existence of  $W_{loss}$  and  $\eta$  is produced by hysteresis behavior and electric leakage during charge-discharge process, which is negative for stability and service life due to the calorification phenomenon. Therefore,  $\eta$  can be considered of equal importance as  $W_{rec}$ .

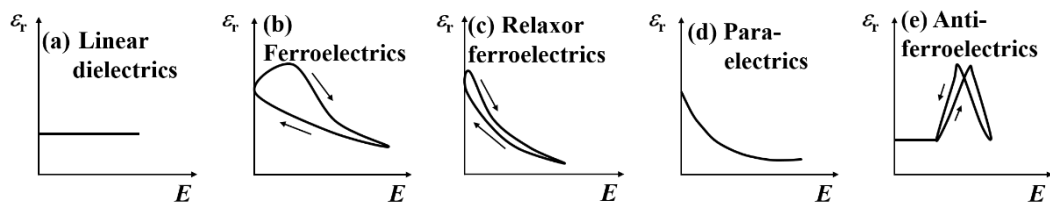


**Fig. 1-5** Polarization hysteresis loops of nonlinear dielectrics under external electric field.

### 1.2.3 The influencing factors of energy storage property

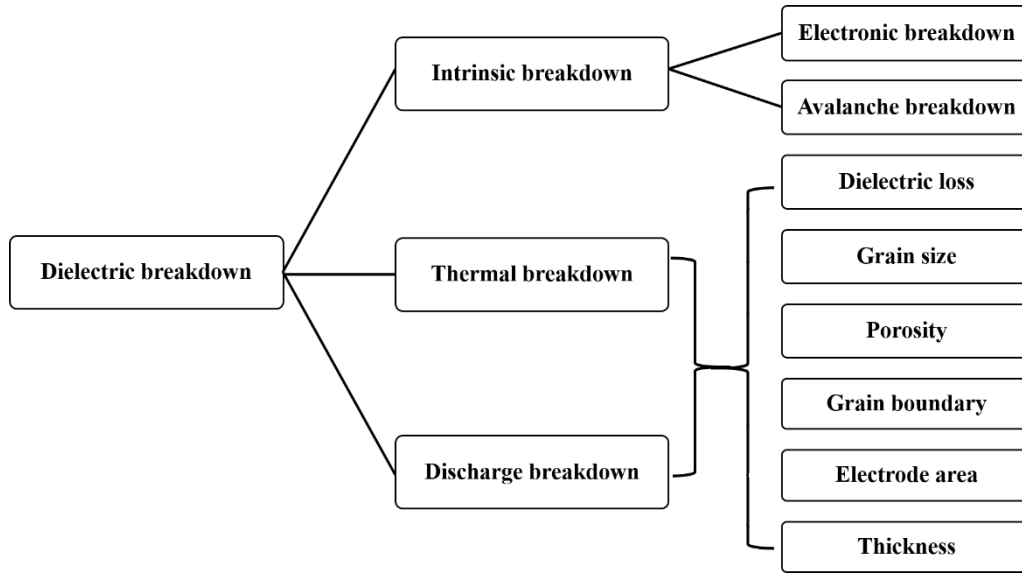
From the above analysis,  $W_{rec}$  and  $\eta$  are directly related to the breakdown electric field strength ( $E_b$ ), polarization strength  $P$  and the shape of  $P$ - $E$  loops. In another word, higher  $E_b$ ,  $P_{max}$ , lower  $P_r$ , and a slimmer  $P$ - $E$  loop are instrumental for the improvement of  $W_{rec}$  and  $\eta$ .

The value of  $\epsilon_r$  is a key parameter used to measure the polarization performance, especially in macroscopic aspect, which shows a positive correlation with charge storage property. Different dielectrics show unique relationships between  $\epsilon_r$  and applied electric fields, as shown in Fig. 1-6.<sup>[23]</sup> Based on Eqs. (1-3) and (1-7), a higher  $\epsilon_r$  contributes to enhanced energy storage properties, however, this often shows a negative influence on the improvement of  $E_b$ . Thus, balancing the values of  $\epsilon_r$  and  $E_b$  is necessary for enhanced performance of energy storage.



**Fig. 1-6** Dielectric constant depended on applied electric field ( $E$ ) for (a) linear dielectrics, (b) ferroelectrics, (c) relaxor ferroelectrics, (d) para-electrics, (e) anti-ferroelectrics.<sup>[23]</sup>

The break-over of dielectrics derived from external electric field is called breakdown process, and the critical electric field strength before breakdown is defined as breakdown electric field strength  $E_b$ . As shown in Fig. 1-7, the breakdown of solid dielectrics can be divided into three types according to different mechanisms including intrinsic breakdown, thermal breakdown and discharge breakdown.<sup>[24,25]</sup> Although, the dielectrics usually exhibit a high intrinsic breakdown strength, however, the thermal breakdown and discharge breakdown usually occur before the realization of the intrinsic breakdown. The  $E_b$  values are affected by both intrinsic and extrinsic factors. Therefore, it is feasible to improve  $E_b$  by tailoring the dielectric loss, grain size, homogeneity, porosity and grain boundary, *etc.* Additionally, a decrease in electrode area and thickness can reduce the probability of breakdown process.



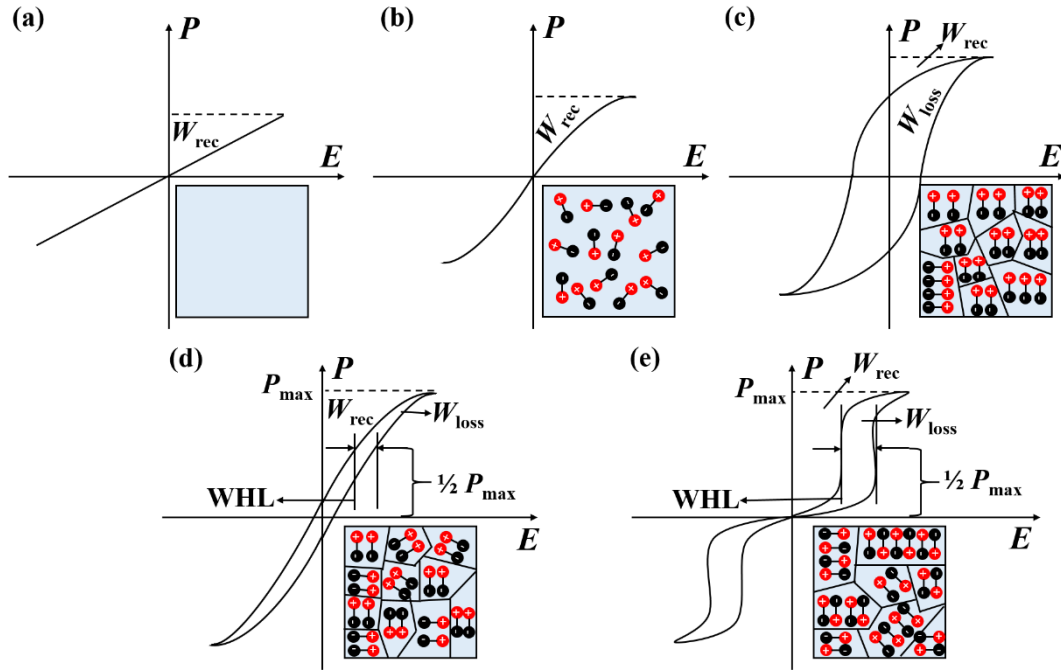
**Fig. 1-7** Illustration of dielectric breakdown types and the influencing factors.<sup>[25]</sup>

The shape of  $P$ - $E$  loops is closely related to the ferroelectricity represented by  $P_r$ ,  $P_{\max}$ , and  $E_C$ , which are critical parameters in the calculation of energy storage density and efficiency as shown above equations.<sup>[21,22,25]</sup> A large  $\Delta P$  ( $P_{\max} - P_r$ ) and lower  $E_C$  can effectively improve energy storage density, while slimmer  $P$ - $E$  loops are responsible for high efficiency. Hence, reducing ferroelectricity is beneficial for energy storage, and element dopant is a primary approach towards realization.

### 1.3 Energy Storage Dielectric Capacitors

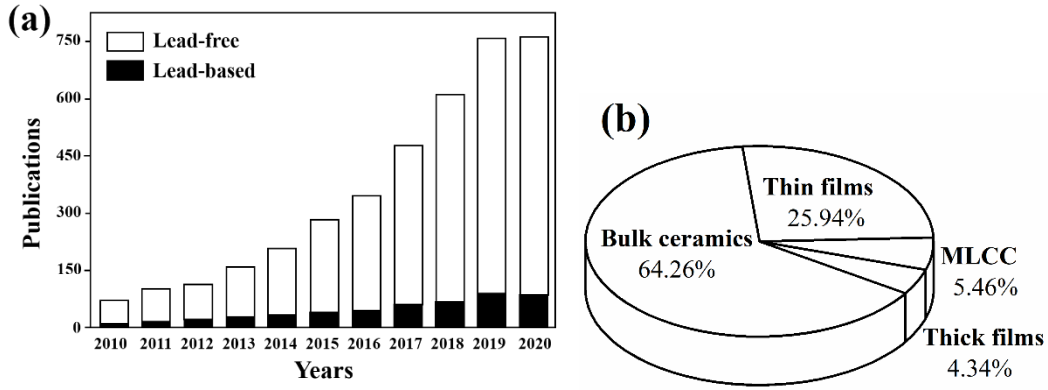
As demonstrated in Fig. 1-8, based on the principle and unique hysteresis  $P$ - $E$  loops, the dielectric capacitors used for energy storage can be divided into five categories:<sup>[22,26]</sup> linear dielectric (LD)<sup>[27,28]</sup>, para-electric (PE)<sup>[29-31]</sup>, ferroelectric (FE)<sup>[32]</sup>, relaxor ferroelectric (RFE)<sup>[33-35]</sup> and anti-ferroelectric (AFE)<sup>[36-40]</sup> materials. Although a higher  $E_b$  can be achieved in LDs, the smaller  $\epsilon_r$  values will result in poor performance of energy storage. Typical FEs present a large  $P_r$  and wide  $P$ - $E$  loops, which are disadvantageous to energy storage. Therefore, these two materials are rarely studied in recent years in energy storage applications. Alternatively, due to the higher  $P_{\max}$ , lower  $P_r$  and much slimmer  $P$ - $E$  loops, the PE, RFE and AFE systems are the most commonly investigated energy storage ceramics so far.

In addition, the width of hysteresis loops (WHL) located at  $\frac{1}{2}P_{\max}$  is introduced in this study, as shown in Figs. 1-8(d, e). The WHL is applied to qualitatively describe  $\eta$ , and a reduced WHL is beneficial for improving  $\eta$ .



**Fig. 1-8**  $P$ - $E$  loops and domain structures of different dielectric materials for (a) linear dielectrics, (b) para-electrics, (c) ferroelectrics, (d) relaxor-ferroelectrics, (e) anti-ferroelectrics.<sup>[22,26]</sup>

In the past, researches on energy storage are mainly focused on lead-based materials, especially  $\text{PbZrO}_3$ -based materials due to their enhanced electrical properties. However, this material is detrimental to the environment and human health as the Pb content is commonly above 60% in lead-based ceramics. Considering the aforementioned limitation, there is a strong demand for the development of lead-free ceramic-based dielectric capacitors. Therefore, researches on lead-free energy storage materials, especially ceramics, has gradually become the key research direction, as shown in Fig. 1-9, according to the “ISIS Web of Science”.

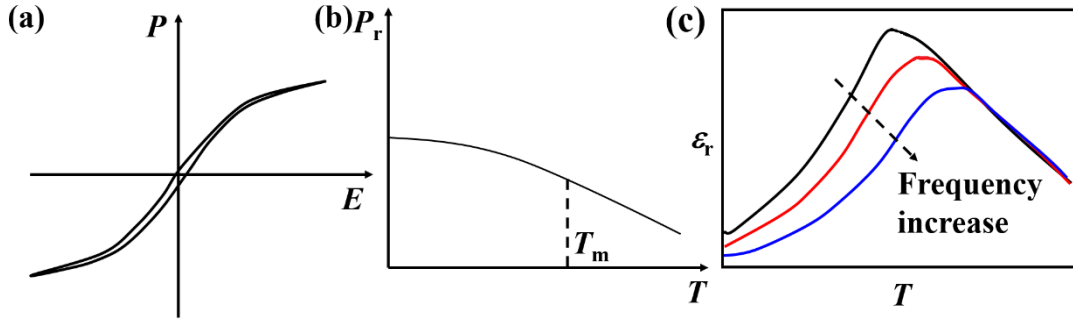


**Fig. 1-9** (a) The statistical data on publications from 2010 to 2020 years by searching the keywords of “dielectric” and “energy storage” in “ISIS Web of Science”, (b) publications on dielectric materials for energy storage with the form of bulk ceramics, thin films, thick films and multi-layer ceramic capacitors (MLCC) in refereed journals in a time period of 2010-2020.

### 1.3.1 Relaxor-ferroelectrics

Since the discovery, RFEs have attracted much attention in scientific researches and applications due to its peculiar properties such as distinctive dielectric properties, large field-induced strain, and excellent thermal stability.<sup>[41]</sup> In RFEs, the effect of external electric field on dipole orientation is weaker than that of thermal motion, which allows the dipoles to distribute chaotically, leading to a different dipole orientation as compared with FEs.<sup>[41-43]</sup> When the electric field is removed, the weakly oriented dipoles will return to a chaotic state due to thermal motion, which is referred to as the relaxation polarization.<sup>[41-43]</sup> These unique behaviors are displayed in Fig. 1-10, demonstrating as slim  $P$ - $E$  loops, local polarization at high temperatures, and frequency diffusion behavior in  $\epsilon_r$ - $T$  curves.<sup>[42-44]</sup> The relaxor behaviors are assumed to originate from the nano-sized polar regions and their answers to surrounding stimulus.<sup>[42,43]</sup> A decay in temperature-dependent polarization is beneficial in obtaining a high  $W_{\text{rec}}$  and  $\eta$ , which is resulted from diffused phase transition.<sup>[45]</sup> In the past decades, several lead-free relaxor systems have been investigated such as  $\text{BaTiO}_3$  (BT)-<sup>[46,47]</sup>,  $(\text{Bi}_{0.5}\text{Na}_{0.5})\text{TiO}_3$  (BNT)-<sup>[37,48,49]</sup> based ceramics.





**Fig. 1-10** Typical RFE characteristics for (a)  $P$ - $E$  loops, (b)  $P_r$  versus  $T$ , and (c) frequency diffusion behavior.<sup>[42-44]</sup>

Ferroelectric BNT ceramics with a polar rhombohedral  $R3c$  phase caused by the long-pair  $6S^2$  electronic configuration of  $Bi^{3+}$  can be transformed into a RFE weakly tetragonal  $P4bm$  phase.<sup>[50,51]</sup> To improve its energy storage properties, composition modification is adopted to tailor  $P$ - $E$  loops of BNT ceramics by constructing morphotropic phase boundary (MPB).<sup>[52]</sup>  $(1-x)BNT-xBT$  ( $x = 6-7\%$ ) binary solid solution near MPB presents an excellent electrical properties, and is a promising candidate for energy storage.<sup>[52]</sup> Therefore, many endeavors have been applied to induce relaxor phase and enhance energy storage properties by forming binary or ternary solutions.<sup>[53-55]</sup> For example, Xu *et al.*<sup>[56]</sup> studied the energy storage properties of  $NaNbO_3$  (NN)-doped  $0.92BNT-0.08BT$  ceramics. In their study, the optimum energy storage density could reach  $0.71 \text{ J/cm}^3$  at  $7.0 \text{ kV/mm}$  when 1% NN was added, which was induced by the concentration variation of defect dipole and reduction in rhombohedral and tetragonal phase. In addition, BT with a simple perovskite structure shows a moderate Curie temperature ( $T_C$ ) of  $120 \text{ }^\circ\text{C}$  with a high  $\epsilon_r$  of 10000, and it becomes a common dielectric material in passive capacitors.<sup>[57]</sup> After modification, the phase transition temperature of BT shifts to lower temperatures leading to broad and weakly coupled relaxor behaviors.<sup>[57-59]</sup> Furthermore, an enhanced energy storage performance was obtained in Mn-modified  $0.9BaTiO_3-0.1Bi(Mg_{2/3}Nb_{1/3})O_3$  ceramics with  $W_{rec}$  of  $1.70 \text{ J/cm}^3$  and  $\eta$  of 90%.<sup>[59]</sup>

### 1.3.2 Para-electrics

PEs possess higher  $E_b$  ranges from 0.3-1.2 MV/mm, moderate  $\epsilon_r$ , lower dielectric loss ( $\tan\delta$ ) and weak nonlinear slim  $P$ - $E$  hysteresis loops, which make them promising for energy storage applications.<sup>[60]</sup> In this regard, improvement for PE ceramics has been centered on increasing  $\epsilon_r$  and improving polarization behaviors on the basis of maintaining higher  $E_b$ .

SrTiO<sub>3</sub> (ST) is the most representative material for PE ceramics with a cubic phase and space group of  $Pm\bar{3}m$ , having  $T_C$  of -168 °C. Its advantages of lower  $\tan\delta$ , moderate  $\epsilon_r$  (~250) as well as good thermal-, frequency-independent dielectric properties have been recognized by researchers.<sup>[61]</sup> In their work, doped Ba<sub>0.4</sub>Sr<sub>0.6</sub>TiO<sub>3</sub> (BST) ceramics with grain size of 0.5  $\mu\text{m}$  were produced, achieving a moderate  $W_{\text{rec}}$  of 1.28 J/cm<sup>3</sup> under 24.3 kV/mm electric field. The influence of ZnO and MgO nanopowders on energy storage properties of BST ceramics has also been significantly investigated.<sup>[62,63]</sup> Both additives were found to show positive effects on energy storage performance. The ZnO-doped ceramics presented a maximum  $W_{\text{rec}}$  of 3.9 J/cm<sup>3</sup> at 40 kV/mm, while MgO-doped ceramics revealed  $W_{\text{rec}}$  of 1.14 J/cm<sup>3</sup> at 33.1 kV/mm. Other researches have also shown that the doping of rare earth elements can promote the energy storage properties of PEs by increasing  $P_{\text{max}}$  and  $E_b$ .<sup>[61,64,65]</sup>

### 1.3.3 Anti-ferroelectrics

In classic AFE materials, adjacent dipoles in the same domain are initially aligned in the opposite directions, leading to a zero  $P_r$  from the macro point of view.<sup>[66]</sup> Under sufficient electric field, the initially anti-parallel dipoles can be re-arrayed in the parallel state along the direction of electric field, changing into FE state with a relatively large polarization, which is known as the electric field-induced AFE-FE phase transition.<sup>[66]</sup> After the removal of external electric field, these dipoles will return to its anti-parallel state and the induced FE phase will also return to initial AFE state due to the similar free energy between AFE and FE phase.<sup>[15,16]</sup> As a result, the  $P$ - $E$  curves show a double hysteresis loop under external electric field, which enables large amounts of energy to

be stored and released. The large  $\Delta P$ , moderate  $E_C$  and double  $P-E$  loops make them a promising candidate for energy storage applications. Various approaches have been introduced to investigate the energy storage performance of AFE materials, with emphasis on  $\text{PbZrO}_3$  (PZ),  $\text{AgNbO}_3$  (AN), and  $\text{NaNbO}_3$  (NN) systems.

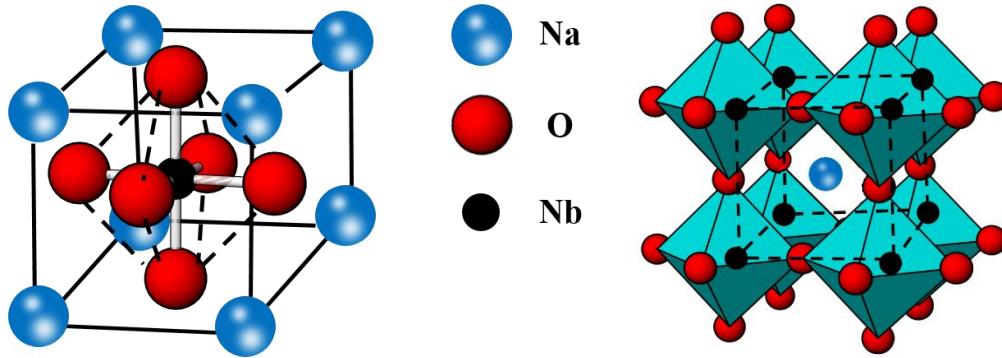
In 1951, Kittel<sup>[67]</sup> was the first to conduct a study on the AFE theory and predicted the thermodynamic dielectric anomaly, but the energy storage performance was not widely studied until 1961.<sup>[68]</sup> Nowadays, various PZ-based systems have been studied by decreasing AFE-FE phase transition electric field strength and improving  $E_b$ , especially via the chemical modification with  $\text{La}^{3+}$ ,  $\text{Ti}^{4+}$ ,  $\text{Nb}^{5+}$ ,  $\text{Sn}^{4+}$ ,  $\text{Mg}^{2+}$ .<sup>[69-73]</sup> Because of the pollution of lead-based materials, lead-free AFE materials have become the core focus in recent researches. Since 2007, AN-based systems have drawn strong interests when Fu *et al.*<sup>[74]</sup> prepared high purity AN ceramics and observed characteristic double  $P-E$  hysteresis loops at RT. Since then, lots of attempts have been focused on improving the energy storage properties of AN-based ceramics.<sup>[75-77]</sup> Although  $W_{\text{rec}}$  can be enlarged to above  $2.0 \text{ J/cm}^3$  induced by the presence of submicron polar regions. However, poor  $\eta$  values lower than 60% are usually discovered due to the fat  $P-E$  loops.<sup>[76,77]</sup> The lower  $\eta$  and higher phase transition electric field strength greatly restrict their industrial applications. In addition, traditional perovskite NN ceramics have always been regarded as promising alternatives.<sup>[78-80]</sup> Although characteristic double  $P-E$  hysteresis loops usually disappear near RT, the AFE-like slimmer  $P-E$  loops induced by the coexistence of AFE and FE phase are beneficial to energy storage.

## 1.4 The Research Status of $\text{NaNbO}_3$ -Based Energy Storage Ceramics

### 1.4.1 Crystal structure of $\text{NaNbO}_3$ ceramics

It is well known that sodium niobate possesses a typical perovskite structure with a chemical composition of  $\text{ABO}_3$ , in which the coordination numbers of  $\text{Na}^+$ ,  $\text{Nb}^{5+}$ ,  $\text{O}^{2-}$  are 12, 6, 6, respectively. The ion arrangement of an ideal cubic perovskite NN structure is illustrated in Fig. 1-11.<sup>[81]</sup> The Na atom is shown at the 8 apexes of the cube unit cell

with a larger ion radius, while Nb atom is located at the center of the cube with a smaller ion radius. The oxygen occupies the 6 face-centered positions, giving corner-shared strings of NbO<sub>6</sub> octahedral, which extends infinitely in three dimensions.<sup>[81]</sup>



**Fig. 1-11** Typical cubic perovskite NaNbO<sub>3</sub> unit cell, where blue spheres represent Na cation, black spheres represent Nb anions and red spheres represent oxygen cation forming an oxygen octahedron.<sup>[81]</sup>

The ions applied in perovskite ABO<sub>3</sub> ceramics satisfy the following relationship with Goldschmidt tolerance factor  $t$ :<sup>[82]</sup>

$$t = \frac{(R_A + R_O)}{\sqrt{2}(R_B + R_O)} \quad (1-10)$$

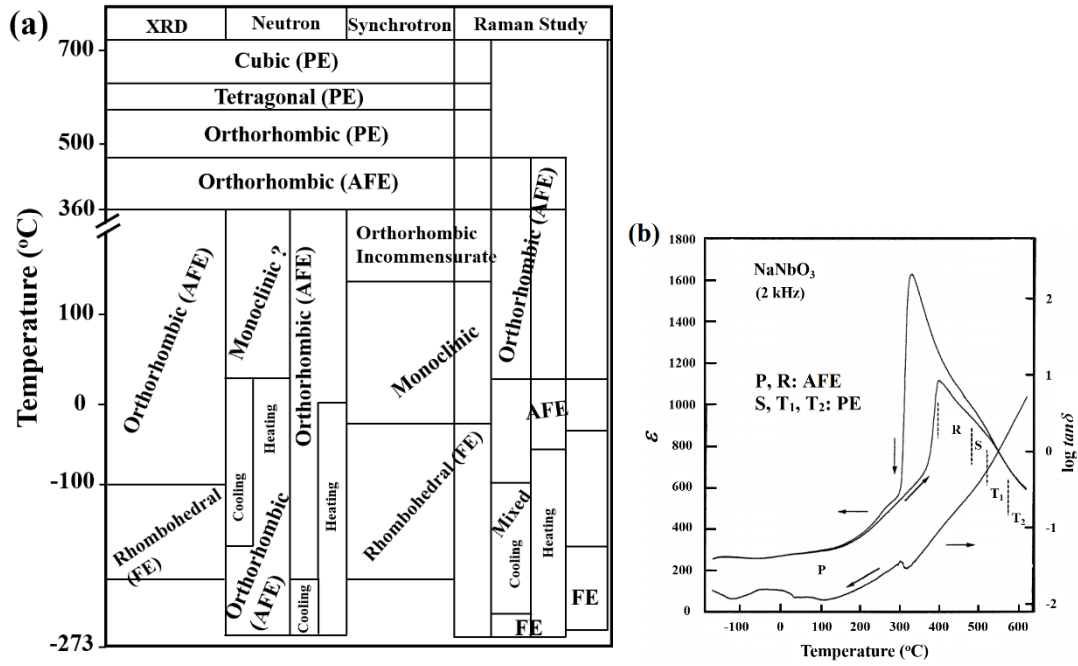
where  $R_A$ ,  $R_B$ , and  $R_O$  are ionic radii of A- and, B-site cations, and oxygen ions, respectively. When  $t$  falls within 0.77-1.1, the crystals tend to exist in a perovskite structure.<sup>[82]</sup>

For perovskite NN ceramics, except for appropriate ion radius, the valence sum of A-site and B-site cations should be +6.<sup>[78-82]</sup> For example, the valences of A-site and B-site cations are +1 and +5, respectively. This tenability of the perovskite structure will cause structural distortions, forming a composite perovskite structure. The composite perovskite materials are not only possess traditional FE or AFE properties of the ideal perovskite structure, but also show many new electrical functions, and have become a research hotspot recently.<sup>[78-80,82]</sup>

#### 1.4.2 Phase transition behavior of $\text{NaNbO}_3$ ceramics

For several decades, researches on the phase transition behavior of NN have been ongoing with existing debates, and discrepancies between different characterization methods have been discovered,<sup>[83]</sup> as displayed in Fig. 1-12(a). These show a fairly complex sequence of thermal-induced structural phase transitions involving antiferrodistortion and ferrodistortion, which are caused by the tilting of oxygen octahedron and displacement of Nb ion from the center position.<sup>[84,85]</sup> The phase structures observed by different techniques vary greatly, including X-ray diffraction (XRD)<sup>[86-88]</sup>, neutron diffraction<sup>[89,90]</sup>, synchrotron XRD<sup>[91]</sup>, and Raman scattering study<sup>[91-95]</sup>. Until now, the phase structure, space group, and phase transition processes remain uncertain. However, all studies have proved that NN ceramics possess an AFE phase at RT. Among these, XRD is the most commonly used, especially for dielectric applications. The previous XRD analysis was obtained through calculating in the 1970s, and no specific diffraction peaks were demonstrated.<sup>[86-88]</sup> Generally, from the calculated XRD results, there exist several structural phases as temperature decreases from 640 °C to -190 °C, as shown in Fig. 1-12(b), it successively demonstrates cubic PE phase, tetragonal PE phase, orthorhombic PE phase, orthorhombic AFE phase, and rhombohedral FE phase.<sup>[96]</sup> Although NN ceramics exist several phase transitions, the AFE phase transition around 360 °C is usually observed as the dielectric anomaly from the dielectric temperature spectrum, involving different space groups and unit cell dimensions. Furthermore, different phases can also coexist in a wide temperature range.

At ambient conditions, pure NN is well known to adopt an AFE *P* phase with an orthorhombic *Pbma* symmetry. However, a polar FE polymorph, which is generally referred to as orthorhombic *Q* phase (*P2<sub>1</sub>ma*), usually coexists with the AFE phase in several ways owing to their similar free energies.<sup>[89,97]</sup> This tends to bring pure NN ceramics square shaped *P-E* hysteresis loops, resulting from a electric field-induced irreversible AFE to FE phase transition instead of a double *P-E* hysteresis loops, leading to a low  $W_{\text{rec}}$  and low  $\eta$ .<sup>[98]</sup>



**Fig. 1-12** (a) Temperature-dependent phase transition diagram of NaNbO<sub>3</sub><sup>[86-95,99]</sup> and (b) variation of dielectric constant and loss of NaNbO<sub>3</sub> with temperature<sup>[100]</sup>.

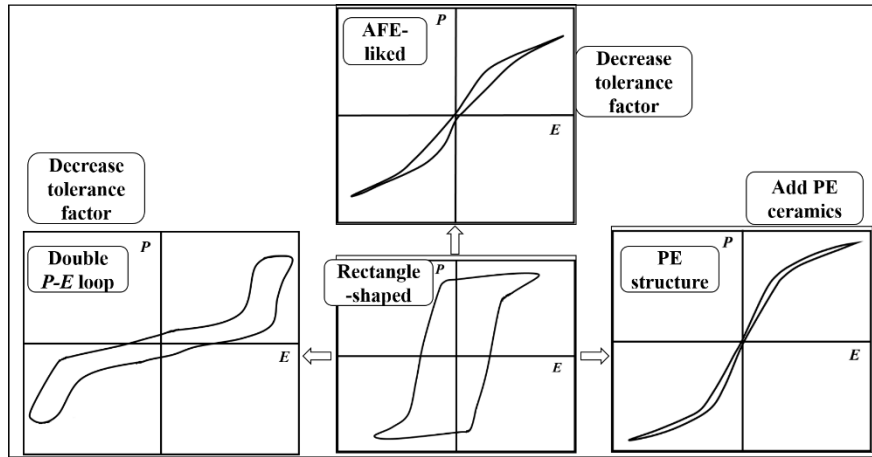
### 1.4.3 Modification of NaNbO<sub>3</sub>-based energy storage ceramics

Over the past decades, various attempts have been devoted to the improvement in piezoelectric properties for NN-based ceramics regarded as piezoelectric candidates. Conversely, only a little attention has been paid to investigating the energy storage properties and mechanisms. However, the relatively high polarization (30 μC/cm<sup>2</sup>) should be considered as a favorable parameter for energy storage.<sup>[101]</sup>

Initially, pure NN was formerly regarded as an AFE non-polar material by researchers, but the *P-E* loops showed an opposite result.<sup>[83,102]</sup> The characteristic double *P-E* loops were only observed in high quality NN single crystals during several initial cycles when an external electric field perpendicular to the orthorhombic *c* axis was applied, while square shaped *P-E* loops were manifested in polycrystalline NN ceramics at RT due to the existence of metastable FE phase.<sup>[103,104]</sup> Recently, the energy storage potential and stabilized AFE domains in NN-based ceramics have been studied. Various conclusions reveal that the chemical modification is a flexible way to tailor and

stabilize the AFE domains in NN ceramics.<sup>[82,105,106]</sup> For example, Ag and K were introduced to substitute Na in A-site, an AFE/FE phase boundary was constructed.<sup>[105]</sup>

According to the characteristic temperature dependence of  $\epsilon_r$  and  $P$ - $E$  loops, NN-based energy storage ceramics can be divided into three categories, as displayed in Fig. 1-13. In the first category, with the addition of second compound, a stabilized AFE phase can be constructed induced by a reduction in tolerance factor, showing double hysteresis  $P$ - $E$  loops.<sup>[82]</sup> However, these materials usually possess lower  $W_{\text{rec}}$  and  $\eta$  due to the large hysteresis and low  $E_b$ . For example, double  $P$ - $E$  loops were observed at RT with a tolerance factor of 0.9644 for 0.96NN-0.04CaZrO<sub>3</sub> ceramics. However, both  $W_{\text{rec}}$  (0.55 J/cm<sup>3</sup>) and  $\eta$  (63.0%) were scant.<sup>[107]</sup> Similar behavior was observed for CaZrO<sub>3</sub> and BaZrO<sub>3</sub> co-doped NN ceramics.<sup>[108]</sup> The second category is obtained by incorporating PE components, especially SrTiO<sub>3</sub>, which is beneficial for improving  $E_b$  and thinning the  $P$ - $E$  loops.<sup>[7,109]</sup> A stable PE phase could be constructed in SrTiO<sub>3</sub> modified NN ceramics, producing a higher  $W_{\text{rec}}$  (3.02 J/cm<sup>3</sup>) and  $\eta$  (80.7%) under a larger electric field (32.3 kV/mm).<sup>[7]</sup> Nevertheless, the PE phase will deteriorate  $\epsilon_r$  and  $P_{\text{max}}$ , thus a large electric field is required to improve  $W_{\text{rec}}$ , as a consequence leads to high security risks and high cost of insulation technology. The last category is defined as AFE-liked ceramics with slim  $P$ - $E$  loops instead of the typical double hysteresis loops. In this material, the AFE phase can be stabilized, leading to reduced  $P_r$ , while a weaker FE phase (polar nano regions) still exists.<sup>[110]</sup> Therefore, the slim  $P$ - $E$  loops with small but nonzero  $P_r$  are demonstrated induced by a coexistence of AFE and FE phase, which are defined as AFE-liked  $P$ - $E$  loops.<sup>[78,80]</sup> Hence, based on previous research, it is still called AFE phase in this work. The AFE-liked NN ceramics are most promising due to their enhanced electrical properties and moderate  $E_b$ .



**Fig. 1-13** Schematic diagram of three routes of chemical modified NN-based ceramics.

### 1.5 Electrocaloric Effect and Research Status

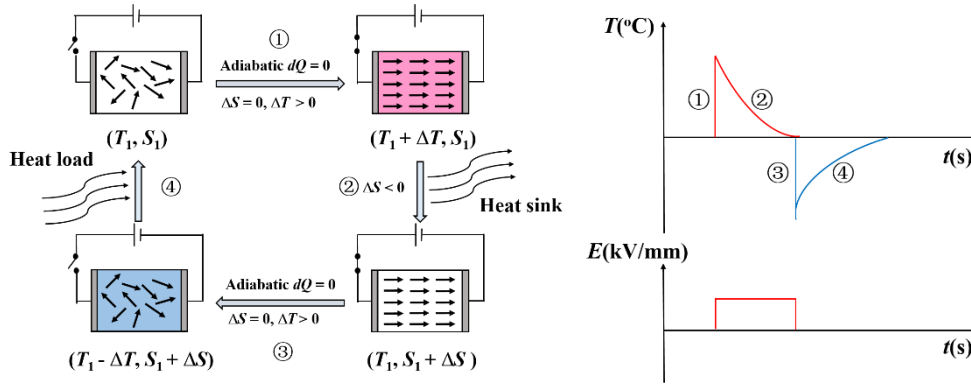
Recently, the electrocaloric effect (ECE) of dielectrics has attracted widespread interest due to their advantages such as refrigeration miniaturization, high efficiency and environmental protection. Although the ECE has been discovered for several decades, the insufficient adiabatic temperature change ( $\Delta T$ ) interrupted the further study.<sup>[111,112]</sup> Recent development in the design of components and refrigeration systems reveals that the ECE cost is superior to conventional devices, which has prompted new attention in ECE.<sup>[113]</sup> The theoretical basis of electrocaloric (EC) refrigeration depends on the fact that the polarized condition of dielectric materials will be altered when external electric field is applied or not applied, resulting in a change in  $\Delta T$  and isothermal entropy change ( $\Delta S$ ).<sup>[112,114]</sup> Compared with other solid refrigeration technics, EC technology possesses the advantages of easy availability, low cost, *etc.*<sup>[114]</sup>

#### 1.5.1 The refrigeration principle of electrocaloric effect

As displayed in Fig. 1-16, a complete refrigeration cycle is composed of four separate parts namely adiabatic polarization, heat transfer, adiabatic depolarization, and endothermic process.<sup>[112,114,115]</sup> First, adiabatic polarization: in an adiabatic condition, dielectric dipoles are transformed from disordered state to ordered state as external electric field is applied, leading to a decrease in entropy and enthalpy. The temperature



of EC materials will increase in order to keep the total entropy constant. Second, heat transfer: with the external electric field applied, the heat in EC system is transferred to the surrounding environment or medium coupled with the decrease in entropy and enthalpy, causing a decrease in temperature of the EC material. Third, in adiabatic depolarization, ordered dipoles will return to the disordered state when the external electric field is removed, giving rise to a further decrease in system temperature. Lastly, in endothermic process, the heat of load system is absorbed by EC materials, leading to temperature decrease in the target system.



**Fig. 1-14** A schematic diagram for an electrocaloric effect solid-state cooling cycle involving two constant-entropy transitions and two at constant-field  $E$ .<sup>[114,115]</sup>

According to the first law of thermodynamics and Maxwell equations, the  $\Delta S$  and  $\Delta T$  can be calculated as:<sup>[116,117]</sup>

$$\Delta S = -\frac{1}{\rho} \int_{E_1}^{E_2} \left( \frac{\partial P}{\partial T} \right)_E dE \quad (1-11)$$

$$\Delta T = -\frac{1}{\rho C_E} \int_{E_1}^{E_2} \frac{T}{C} \left( \frac{\partial P}{\partial T} \right)_E dE \quad (1-12)$$

where,  $T$  is the temperature,  $P$  is polarization value,  $C_E$  is the thermal capacity, and  $\rho$  is density of ceramics,  $E_1$  and  $E_2$  are initial and maximum electric field respectively. Besides, the plus and minus values in above formulas are independent on the EC response intensity, demonstrating a positive ECE ( $\Delta T > 0$ ) and negative ECE ( $\Delta T < 0$ ).

Based on Eqs. (1-11) and (1-12), large  $E_b$  and  $\partial P/\partial T$  values are needed for enhanced  $\Delta T$  and  $\Delta S$ . Usually,  $\partial P/\partial T$  achieves a maximum value when phase

transition occurs. Therefore, it is feasible to improve EC response by locating the phase transition near RT where most of the refrigerators are usually applied. Nowadays, studies on ECE are still at their infancy stage. Therefore, how to improve  $\Delta T$ , refrigeration efficiency and efficient heat dissipation near RT are the primary concerns in ECE studies and applications.

### 1.5.2 Development of electrocaloric effect

The ECE was not attended until 1981 when Tuttle *et al.* observed a relatively large  $\Delta T$  of 2.6 K around  $T_C$  (161 °C) in  $\text{Pb}_{0.99}\text{Nb}_{0.02}(\text{Zr}_{0.75}\text{Sn}_{0.20}\text{Ti}_{0.05})_{0.98}\text{O}_3$  ceramics.<sup>[118]</sup> In the beginning, most studies only focus on the phase transition at  $T_C$ , but  $T_C$  is usually higher than surrounding temperature.<sup>[116,119]</sup> Therefore, other phase transitions such as AFE-FE phase transition have been employed in ECE studies to effectively broaden the research scope in this field.<sup>[120]</sup>

Considering the environmental issues, the EC response of lead-free ceramics has been ardently studied. In 2013, the ECE of  $(1-x)\text{BaZr}_{0.2}\text{Ti}_{0.8}\text{O}_3-x\text{Ba}_{0.7}\text{Ca}_{0.3}\text{TiO}_3$  ceramics was investigated.<sup>[121]</sup> The results manifested that the dipoles could easily flip due to lower energy barrier when rhombohedral, tetragonal and cubic phases coexisted, achieving a  $\Delta T$  of 0.3 K at environmental conditions. Recently,  $(\text{Ba,Ca})(\text{Ti,Zr})\text{O}_3$  lead-free ceramics have been found a promising system.<sup>[122,123]</sup> It can be concluded that the EC response could be adjusted to lower temperatures by altering the Zr/Ti ratio due to the construction of phase boundary. As a result, a maximum  $\Delta T = 1.64$  K was obtained at 130 °C when  $\text{Zr/Ti} = 0.05/0.95$ , corresponding to  $\Delta S = 1.78$  J/(kg·K). However, the EC response of NN-based ceramics has been barely studied.

## 1.6 Thesis Objectives and Organization

### 1.6.1 Thesis objectives

Nowadays, dielectric capacitors have been widely applied in various areas such as electrical vehicles, pulsed laser, radar and so on in daily, industry and military fields.

However, the major materials are Pb-based materials with lead content above 60%. With the improvement in human health and environmental protection, the development of lead-free dielectric capacitors is urgently needed. Generally, lead-free ceramic-based dielectric capacitors are of high priority due to their distinctive mechanical and thermal stability. NN-based ceramic is deemed as one of the most promising substitutions for lead-based materials owing to its initial AFE nonpolar structure and high polarization. However, the square-shaped  $P$ - $E$  loops are manifested in polycrystalline NN ceramics due to the existence of metastable FE phase, restricting the improvement in energy storage properties. In addition, the phase structure and complex phase transition behavior of NN ceramics also obstruct their applications.

Stabilizing the AFE phase through chemical modification can induce slim  $P$ - $E$  loops. Therefore, the energy storage properties,  $W_{\text{rec}}$  and  $\eta$ , can be effectively improved. Also, an attractive ECE performance can be observed in different NN-based systems, which is superior to most lead-free ceramics. Therefore, chemical modification was employed in perovskite NN ceramics. The main objectives of this research are presented below:

1. To stabilize the AFE phase in NN ceramics through adding  $\text{La}(\text{Nb}_{1/3}\text{Mg}_{2/3})\text{O}_3$  (LNM) ceramics. LNM can break the long-range ordered FE phase and stabilize AFE phase in NN ceramics, improving energy storage properties and ECE performance, which is better than most lead-free ceramics.
2. To further improve  $W_{\text{rec}}$  by adding a sintering aid  $\text{MnO}_2$  in AFE-liked 0.955NN-0.045LNM ceramics. The introduction of  $\text{MnO}_2$  can improve the electrical and energy storage properties effectively through inhibiting element volatilization. Furthermore, the thermal stability of energy storage is also improved with the addition of  $\text{MnO}_2$ .
3. To further improve  $W_{\text{rec}}$  and  $\eta$  simultaneously under a lower electric field by adding LNM and  $\text{CaZrO}_3$  (CZ). The stabilized AFE phase and enhanced dielectric properties can advance energy storage performance, especially  $\eta$ , which can be compared with RFE and PE ceramics. An attractive ECE behavior is observed, presenting superior positive and negative ECE.

### 1.6.2 Thesis organization

The thesis is organized into seven chapters. Chapter 1 introduces the research background and objectives of this research. Chapter 2 describes the reagents, equipment, and experimental procedures. Chapter 3 expounds on the AFE structure induced by LNM ceramics and the effects on dielectric properties, phase transition behavior and energy storage performance. Chapter 4 discusses the effects of  $\text{MnO}_2$  on dielectric properties and energy storage performance in AFE-liked 0.955NN-0.045LNM ceramics. Chapter 5 reveals the improved energy storage performance in LNM and CZ doped NN ceramics under moderate conditions. Chapter 6 expounds on the electrocaloric effect and phase diagrams of NN-based ceramics. Finally, chapter 7 presents the conclusions of this research.

## References

- [1] V. Etacheri, R. Marom, R. Elazari, G. Salitra and D. Aurbach. *Energy Environ. Sci.*, **4**, 3243, 2011.
- [2] J. H. Seo, Z. M. Fan, H. Nakaya, R. Rajagopalan, E. D. Gomez, M. Iwasaki and C. A. Randall. *Jpn. J. Appl. Phys.*, **60**, 037001, 2021.
- [3] W. S. Li, K. C. Chuang, Y. S. Li, J. D. Luo, M. L. Chang and H. C. Cheng. *Jpn. J. Appl. Phys.*, **58**, 056502, 2019.
- [4] S. Rawal, B. Joshi and Y. Kumar. *J. Energy Storage*, **20**, 418, 2018.
- [5] I. Hadjipaschalis, A. Poullikkas and V. Efthimiou. *Renew. Sustain. Energy Rev.*, **13**, 1513, 2009.
- [6] E. Karden, S. Ploumen, B. Fricke, T. Miller and K. Snyder. *J. Power Sources*, **168**, 2, 2007.
- [7] M. Zhou, R. Liang, Z. Zhou, S. Yan and X. Dong. *ACS Sustain. Chem. Eng.*, **6**, 12755, 2018.
- [8] F. Wang, C. Zhu and S. F. Zhao. *J. Alloys Compd.*, **869**, 159366, 2021.
- [9] H. Pan, F. Li, Y. Liu, Q. H. Zhang, M. Wang, S. Lan, Y. P. Zheng, J. Ma, L. Gu, Y. Shen, P. Yu, S. J. Zhang, L. Q. Chen, Y. H. Lin and C. W. Nan. *Science*, **365**, 578, 2019.
- [10] Prateek, V. K. Thakur and R. K. Gupta. *Chem. Rev.*, **116**, 4260, 2016.
- [11] Q. Li, F. Z. Yao, Y. Liu, G. Z. Zhang, H. Wang and Q. Wang. *Annu. Rev. Mater. Res.*, **48**, 219, 2018.
- [12] E. Hollenstein, M. Davis, D. Damjanovic and N. Setter. *Appl. Phys. Lett.*, **87**, 182905, 2005.
- [13] Y. P. Guo, K. Kakimoto, and H. Ohsato. *Jpn. J. Appl. Phys.*, **46**, 6662, 2004.
- [14] V. A. Isupov. *Phys. Solid State*, **45**, 1107, 2003.
- [15] D. Viehland, M. Wuttig, and L. E. Cross. *Ferroelectrics*, **120**, 71, 1991.
- [16] Z. Yin, X. T. Chen, X. Song, and J. W. Feng. *Ceram. Int.*, **15**, 311, 1989.
- [17] T. Liu, Y. Pang, M. Zhu and S. Kobayashi. *Nanoscale*, **6**, 2447, 2014.

- [18] B. Quan, X. Liang, G. Ji, Y. Cheng, W. Liu, J. Ma, Y. Zhang, D. Li and G. Xu. *J. Alloys Compd.*, **728**, 1065, 2017.
- [19] N. H. Ahmed, N. N. Srinivas. *IEEE Trans. Dielectr. and Electr. Insul.*, **4**, 13, 1997.
- [20] P. B. Ishai, M. S. Talary, A. Caduff, E. Levy and Y. Feldman. *Meas. Sci. Technol.*, **24**, 102001, 2013.
- [21] H. Palneedi, M. Peddigari, G. T. Hwang, D. Y. Jeong and J. Ryu. *Adv. Funct. Mater.*, **28**, 1803665, 2018.
- [22] G. H. Haertling and C. E Land. *J. Am. Ceram. Soc.*, **54**, 1, 1971.
- [23] S. Tong, B. Ma, M. Narayanan, S. Liu, R. Koritala, U. Balachandran and D. Shi. *ACS Appl. Mater. Interfaces.*, **5**, 1474, 2013.
- [24] K. H. Stark and C. G. Garton. *Nature*, **176**, 2, 1955.
- [25] Z. T. Yang, H. L. Du, L. Jin and D. Poelman. *J. Mater. Chem. A*, **9**, 18026, 2021.
- [26] N. Ortega, A. Kumar, J. F. Scott, D. B. Chrisey, M. Tomazawa, S. Kumari, D. G. B. Diestra and R. S. Katiyar. *J. Phys.: Condens. Matter*, **24**, 445901, 2012.
- [27] J. Chen, Y. F. Wang and W. X. Chen. *J. Mater. Chem. C*, **9**, 5000, 2021.
- [28] C. Wang, G. H. He, S. Chen, D. Zhai, H. Luo and D. Zhang. *J. Mater. Chem. A*, **9**, 8674, 2021.
- [29] G. Liu, L. Y. Zhang, Z. Y. Wang, W. T. Jiang, J. Cai, X. K. Liu, Y. Chen, C. L. Song and Y. Yan. *Ferroelectrics*, **531**, 122, 2018.
- [30] G. F. Zhang, H. X. Liu, Z. H. Yao, M. H. Cao and H. Hao. *J. Mater. Sci. Mater. El.*, **26**, 2726, 2015.
- [31] Y. Wang, Z. Y. Shen, Y. M. Li, Z. M. Wang, W. Q. Luo and Y. Hong. *Ceram. Int.*, **41**, 8252, 2015.
- [32] G. H. Haertling. *J. Am. Ceram. Soc.*, **82**, 797, 1999.
- [33] X. Zhang, F. Yang, W. J. Miao, Z. Su, J. H. Zhao, L. M. Tang, Y. H. Shen, D. Hu, Y. Y. Chen, P. Li, J. J. Liu and Z. B. Pan. *J. Alloys Compd.*, **883**, 160837, 2021.
- [34] L. Zheng, P. C. Sun, P. Zheng, W. F. Bai, L. L. Li, F. Wen, J. J. Zhang, N. N. Wang and Y. Zhang. *J. Mater. Chem. C*, **9**, 5234, 2021.
- [35] X. Y. Zhao, C. Y. Li, J. K. Liu, Y. Q. Ding, W. F. Bai, P. Zheng, P. Li, J. J. Zhang and J. W. Zhai. *Ceram. Int.*, **47**, 25800, 2021.

- [36] J. J. Guo and T. Q. Yang. *J. Alloys Compd.*, **888**, 161539, 2021.
- [37] Y. J. Zhang, P. Liu, Y. F. Qin, K. R. Kandula, G. Z. Zhang, Y. Y. Wu, H. B. Zhang and S. L. Jiang. *J. Eur. Ceram. Soc.*, **41**, 4138, 2021.
- [38] M. H. Zhang, L. Carstensen, C. Zhao, L. Fulanovi, W. Donner and J. Koruza. *J. Am. Ceram. Soc.*, **105**, 451, 2021.
- [39] X. J. Meng, Y. Zhao, Y. Li and X. H. Hao. *J. Am. Ceram. Soc.*, **104**, 2170, 2021.
- [40] X. H. Liu, T. Q. Yang and W. P. Gong. *J. Mater. Chem. C*, **9**, 12399, 2021.
- [41] V. V. Shvartsman, D. C. Lupascu and D. J. Green. *J. Am. Ceram. Soc.*, **95**, 1, 2012.
- [42] I. Grinberg, P. Juhas, P. K. Davies and A. M. Rappe. *Phys. Rev. Lett.*, **99**, 267603, 2007.
- [43] L. E. Cross. *Ferroelectrics*, **151**, 305, 1994.
- [44] T. F. Zhang, X. G. Tang, X. X. Huang, Q. X. Liu, Y. P. Jiang and Q. F. Zhou. *Energy Technol.*, **4**, 633, 2016.
- [45] A. A. Bokov and Z. G. Ye. *J. Mater. Sci.*, **41**, 31, 2006.
- [46] J. H. Lv, H. Hao, X. W. Jiang, Z. Liu, M. Emmanuel, M. H. Cao, Z. H. Yao and H. X. Liu. *J. Am. Ceram. Soc.*, **103**, 5129, 2020.
- [47] F. Yang, Y. Chen, X. Li, W. Huang, G. S. Wang and X. L. Dong. *Ceram. Int.*, **47**, 25785, 2021.
- [48] G. L. Xue, X. F. Zhou, Z. N. Yan, G. Liu, H. Luo and D. Zhang. *J. Alloys Compd.*, **882**, 160755, 2021.
- [49] S. S. Bian, Z. X. Yue, Y. Z. Shi, J. Zhang and W. Feng. *J. Am. Ceram. Soc.*, **104**, 936, 2021.
- [50] H. P. Kim, C. W. Ahn, Y. Hwang, H. Y. Lee and W. Jo. *J. Korean Ceram. Soc.*, **54**, 86, 2017.
- [51] W. Jo, S. Schaab, E. Sapper, L. A. Schmitt, H. J. Kleebe, A. J. Bell and J. Rödel. *J. Appl. Phys.*, **110**, 074106, 2011.
- [52] H. R. Ye, F. Yang, Z. B. Pan, D. Hu, X. J. Lv, H. X. Chen, F. F. Wang, J. S. Wang, P. Li, J. W. Chen, J. J. Liu and J. W. Zhai. *Acta. Mater.*, **203**, 116484, 2021.
- [53] M. K. Bilal, J. Wang, R. Bashir, H. Liu, S. U. Asif, J. Y. Xie and W. B. Hu. *J. Am. Ceram. Soc.*, **104**, 3982, 2021.

- [54] A. Jain, Y. G. Wang, H. Guo and N. Wang. *J. Am. Ceram. Soc.*, **103**, 6308, 2020.
- [55] L. Zhang, Y. P. Pu and M. Chen. *J. Alloys Compd.*, **775**, 342, 2019.
- [56] Q. Xu, T. M. Li, H. Hao, S. J. Zhang, Z. J. Wang, M. H. Cao, Z. H. Yao and H. X. Liu. *J. Eur. Ceram. Soc.*, **35**, 545, 2015.
- [57] M. Y. Tang, L. J. Yu, Y. F. Wang, J. W. Lv, J. Dong, B. Guo, F. K. Chen, Q. Ai, Y. Luo, Q. Li, K. Yu, F. Wu and G. Liu. *Ceram. Int.*, **47**, 3780, 2021.
- [58] Y. Hou, J. C. Li, S. Guo, T. T. Ye and J. F. Ding. *J. Electroceram*, **46**, 141, 2021.
- [59] W. B. Li, D. Zhou and L. X. Pang. *Appl. Phys. Lett.*, **110**, 132902, 2017.
- [60] M. Peddigari, H. Palneedi, G. T. Hwang and J. Ryu. *J. Korean Ceram. Soc.*, **56**, 1, 2019.
- [61] R. V. Shende, D. S. Krueger, G. A. R. Jr and S. J. Lombardo. *J. Am. Ceram. Soc.*, **84**, 3, 2001.
- [62] G. Dong, S. Ma, J. Du and J. Cui. *Ceram. Int.*, **35**, 2069, 2009.
- [63] Q. Zhang, L. Wang, J. Luo, Q. Tang and J. Du. *Int. J. Appl. Ceram. Technol.*, **7**, E124, 2009.
- [64] Y. Zhou, Q. Zhang, J. Luo, Q. Tang, J. Du and E. P. Gorzkowski. *J. Am. Ceram. Soc.*, **96**, 372, 2013.
- [65] J. Song and G. Chen. *J. Mater. Sci.: Mater. Electron.*, **25**, 349, 2013.
- [66] J. Zhai, X. Li and H. Chen. *Thin Solid Films*, **446**, 200, 2004.
- [67] C. Kittel. *Phys. Rev.*, **82**, 729, 1951.
- [68] B. Jaffe. *Proc. IRE*, **49**, 1264, 1961.
- [69] Q. S. Zhu, K. Zhao, R. Xu, Y. J. Feng, Z. Xu and X. Y. Wei. *J. Alloys Compd.*, **877**, 160108, 2021.
- [70] X. J. Meng, Y. Zhao, Y. Li and X. H. Hao. *J. Alloys Compd.*, **868**, 159149, 2021.
- [71] Z. Y. Fu, Y. C. Zhang, L. Li, X. J. He, X. Y. Zhang, J. Zhang, Z.B. Gu and S.T. Zhang. *J. Alloys Compd.*, **873**, 159768, 2021.
- [72] Y. Yang, P. Liu, Y. J. Zhang, K. R. Kandula, J. W. Xu, G. Z. Zhang and S. L. Jiang. *Ceram. Int.*, **46**, 18106, 2020.
- [73] P. F. Zhao, S. B. Wang, H. Tang, X. D. Jian, X. B. Zhao, Y. B. Yao, T. Tao, B. Liang and S. G. Lu. *Scripta Mater.*, **200**, 113920, 2021.



- [74] D. Fu, M. Endo, H. Taniguchi, T. Taniyama and M. Itoh. *Appl. Phys. Lett.*, **90**, 252907, 2007.
- [75] L. Zhao, Q. Liu, S. Zhang and J. F. Li. *J. Mater. Chem. C*, **4**, 8380, 2016.
- [76] A. Song, J. Song, Y. Lv, L. Liang, J. Wang and L. Zhao. *Mater. Lett.*, **237**, 278, 2019.
- [77] Y. Tian, L. Jin, H. Zhang, Z. Xu, X. Wei, E. D. Politova, S. Y. Stefanovich, N. V. Tarakina, I. Abrahams and H. Yan. *J. Mater. Chem. A*, **4**, 17279, 2016.
- [78] K. Beppu, F. Funatomi, H. Adachi and T. Wada. *Jpn. J. Appl. Phys.*, **60**, SFFB01, 2021.
- [79] M. H. Zhang, N. Hadaeghi, S. Egert, H. Ding, H. B. Zhang, P. B. Groszewicz, G. Buntkowsky, A. Klein and J. Koruza. *Chem. Mater.*, **33**, 266, 2021.
- [80] Y. Jiang, C. Q. Zhu, P. Y. Zhao, K. Bi, J. M. Liu, L. M. Guo, X. H. Wang and L. T. Li. *J. Eur. Ceram. Soc.*, **41**, 6465, 2021.
- [81] A. S. Bhalla, R. Y. Guo and R. Roy. *Mater. Res. Innov.*, **4**, 3, 2000.
- [82] H. Shimizu, H. Guo, S. E. Reyes-Lillo, Y. Mizuno, K. M. Rabe and C. A. Randall. *Dalton Trans.*, **44**, 10763, 2015.
- [83] G. Shirane, R. Newnham and R. Pepinsky. *Phys. Rev.*, **96**, 581, 1954.
- [84] S. K. Mishra, M. K. Gupta, R. Mittal, M. Zbiri, S. Rols, H. Schober and S.L. Chaplot. *Phys. Rev. B*, **89**, 184303, 2014.
- [85] M. Tyunina, A. Dejneka, D. Rytz, I. Gregora, F. Borodavka, M. Vondracek and J. Honolka. *J. Phys.: Condens. Mat.*, **26**, 125901, 2014.
- [86] C. N. W. Darlington and H. D. Megaw. *Acta Cryst.*, **B29**, 2171, 1973.
- [87] M. Ahtee, A.M. Glazer, and H.D Megaw. *Phil. Mag.*, **26**, 995, 1972.
- [88] A. M. Glazer, H.D. Megaw. *Phil. Mag.*, **25**, 1119, 1972.
- [89] S. K. Mishra, N. Choudhury, S. L. Chaplot, P. S. R. Krishna and R. Mittal. *Phys. Rev. B*, **76**, 024110, 2007.
- [90] S. K. Mishra, R. Mittal, V. Y. Pomjakushin and S. L. Chaplot. *Phys. Rev. B*, **83**, 134105, 2011.
- [91] Y. I. Yuzyuk, P. Simon, E. Gagarina, L. Hennet, D. Thiaudiere, V. I. Torgashev, S. I. Raevskya, I. P. Raevskii, L. A. Reznitchenko and J. L. Sauvajol. *J. Phys.:*

- Condens. Matter, **17**, 4977, 2005.
- [92] E. Bouizane, M. D. Fontana and M. Ayadi. J. Phys.: Condens. Matter, **15**, 1387, 2003.
- [93] R. J. C. Lima, P. T. C. Freire, J. M. Sasaki, A. P. Ayala , F. E. A. Melo, J. Mendes Filho, K. C. Serra, S. Lanfredi, M. H. Lente and J. A. Eiras. J. Raman Spectrosc., **33**, 669, 2002.
- [94] Z. X. Shen, X. B. Wang, M. H. Kuok, and S. H. Tang. J. Raman Spectrosc., **29**, 379, 1998.
- [95] X. B Wang, Z. X. Shen, Z. P. Hu, L. Qin, S. H. Tang, M. H. Kuok. J. Molecular Structure, **385**, 1, 1996.
- [96] H. D. Megaw. Ferroelectrics, **7**, 87, 1974.
- [97] J. Koruza, P. Groszewicz, H. Breitzke, G. Buntkowsky, T. Rojac and B. Malic. Acta Mater., **126**, 77, 2017.
- [98] H. Z. Guo, H. Shimizu, Y. Mizuno and C. A. Randall. J. Appl. Phys., **118**, 054102, 2015.
- [99] Y. I. Yuzyuk, P. Simon, E. Gagarina, L. Hennet, D. Thiaudiere, V. I. Torgashev, S. I. Raevskaya, I. P. Raevskii, L. A. Reznitchenko and J. L. Sauvajol. J. Phys.: Condens. Mat., **17**, 4977, 2005.
- [100] A. Kania and J. Kwapulinski, J. Phys.: Condens. Matter, **11**, 8933, 1999.
- [101] T. Wada, K. Tsuji, T. Saito and Y. Matsuo. Jpn. J. Appl. Phys., **42**, 6110, 2003.
- [102] A. M. Glazer and H. D. Megaw. Acta Crystallogr. A, **29**, 489, 1973.
- [103] L. E. Cross. Nature, **181**, 2, 1958.
- [104] L. E. Cross and B. J. Nicholson. Lond. Edinb. Dublin Philos. Mag. J. Sci., **46**, 453, 2009.
- [105] Y. Xu, W. Hong, Y. Feng and X. Tan. Appl. Phys. Lett., **104**, 052903, 2014.
- [106] H. Guo, H. Shimizu, Y. Mizuno and C. A. Randall. J. Appl. Phys., **117**, 214103, 2015.
- [107] Z. Y. Liu, J. S. Lu, Y. Q. Mao, P. R. Ren and H. Q. Fan. J. Eur. Ceram. Soc., **38**, 4939, 2018.
- [108] H. Qi, R.Z. Zuo, A.W. Xie, J. Fu and D. Zhang. J. Eur. Ceram. Soc., **39**, 3703,

2019.

- [109] J. M. Ye, G.S. Wang, M. X. Zhou, N. T. Liu, X. F. Chen, S. Li, F. Cao and X. L. Dong. *J. Mater. Chem. C*, **7**, 5639, 2019.
- [110] S. Egert, M. H. Zhang, J. Kuruza, P. B. Groszewicz and G. Buntkowsky. *J. Phys. Chem. C*, **124**, 23852, 2020.
- [111] G. F. Dobrzhansky, N. R. Ivanov and L. F. Kirpichnikova. *Kristallografiya*, **31**, 700, 1986.
- [112] M. Valant. *Prog. Mater. Sci.*, **57**, 980, 2012.
- [113] Y. V. Sinyavsky, G. E. Lugansky and N. D. Pashkov. *Cryogenics*, **32**, 28, 1992.
- [114] J. F. Scott. *Annu. Rev. Mater. Res.*, **41**, 229, 2011.
- [115] S. P. Alpay, J. Mantese, S. Trolrier-McKinstry, Q. Zhang and R. W. Whatmore. *MRS Bull.*, **39**, 1099, 2014.
- [116] A. S. Mischenko, Q. Zhang, J. F. Scott, R. W. Whatmore and N. D. Mathur. *Science*, **311**, 1270, 2006.
- [117] S. G. Lu, X. G. Tang, S. H. Wu and Q. M. Zhang. *J. Inorg. Mater.*, **29**, 6, 2014.
- [118] B. A. Tuttle and D. A. Payne. *Ferroelectrics*, **37**, 603, 1981.
- [119] L. Shebanovs, K. Borman, W. N. Lawless and A. Kalvane. *Ferroelectrics*, **273**, 137, 2002.
- [120] B. Peng, H. Fan and Q. Zhang. *Adv. Funct. Mater.*, **23**, 6, 2013.
- [121] Y. Bai, X. Han and L. Qiao. *Appl. Phys. Lett.*, **102**, 252904, 2013.
- [122] X. Nie, S. Yan, S. Guo, F. Cao, C. Yao, C. Mao, X. Dong and G. Wang. *J. Am. Ceram. Soc.*, **100**, 5202, 2017.
- [123] X. Nie, S. Yan, X. Chen, S. Guo, F. Cao, C. Yao, C. Mao, X. Dong and G. Wang. *Phys. Status Solidi A*, **215**, 1700971, 2018.

## Chapter 2

### Experiment and Characterization

This chapter describes the experimental reagents and procedures used for the conventional solid-state method. Also, the main characterization instruments are introduced.

#### 2.1 Preparation of NaNbO<sub>3</sub>-Based Bulk Ceramics

##### 2.1.1 Experimental reagent

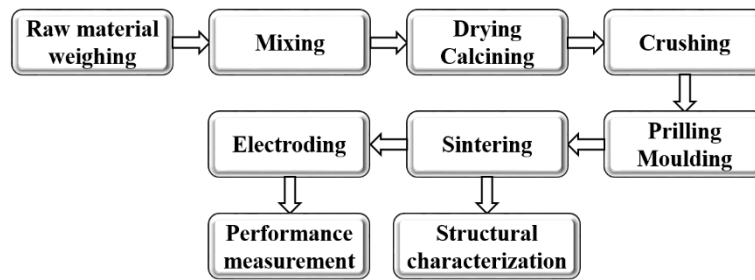
All experiment reagents used in this research are listed in Table 2-1.

**Table 2-1** Experimental reagents used in this research.

Reagent	Formula	Purity	Manufacturer
Sodium carbonate	Na <sub>2</sub> CO <sub>3</sub>	99%	High purity chemicals
Lanthanum oxide	La <sub>2</sub> O <sub>3</sub>	99.9%	High purity chemicals
Magnesium oxide	MgO	99.99%	High purity chemicals
Niobium pentoxide	Nb <sub>2</sub> O <sub>5</sub>	99.9%	High purity chemicals
Bismuth oxide	Bi <sub>2</sub> O <sub>3</sub>	99.99%	High purity chemicals
Calcium carbonate	CaCO <sub>3</sub>	99.99%	Kanto chemical
Zirconium oxide	ZrO <sub>2</sub>	98%	High purity chemicals
Manganese oxide	MnO <sub>2</sub>	99.99%	High purity chemicals

##### 2.1.2 Preparation of ceramics by a solid-state method

All the ceramics were prepared via the conventional solid-state method, the preparation procedures and subsequent processes are shown in Fig. 2-1.



**Fig. 2-1** The preparation process of conventional solid-state method.

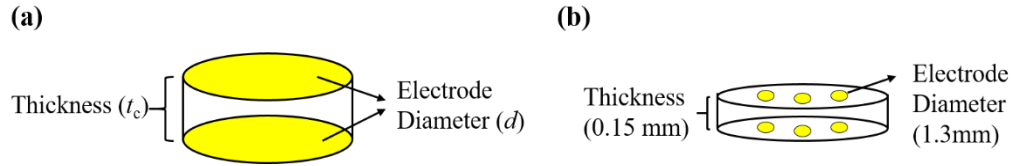
The specific details are described as follows:

- (a) Weighing: raw materials were dried for at least 24 hours at 120 °C in an oven, and subsequently weighed using the electronic scale according to the stoichiometric ratio.
- (b) Mixing: all weighed materials were transferred into zirconia ball milling tanks. The zirconia balls were added at a mass ratio of 1:3, and ethanol was used as media. Planetary ball milling was applied for 6 h.
- (c) Calcining: the obtained pulp after ball milling was dried in an oven at 80 °C. Then, dried powders were pressed into pellets with a diameter of 50 mm and finally calcined at 850-950 °C for 4h.
- (d) Crushing: the calcined blocks were grinded and then ball milled for another 24 h under the same condition as step (b).
- (e) Moulding: dried powders were grinded with 0.5% polyvinyl alcohol (PVA) as binder. The pressed pellets were left for about 12 h at room temperature. These powders were sieved and pressed into pellets with a diameter of 12 mm under a unidirectional pressure of 200 MPa. All green bodies were placed in a furnace at 550 °C for 2 h in order to completely exhaust PVA prior to sintering.
- (f) Sintering: all samples were sintered at air atmospheric condition in a temperature range of 1180-1350 °C in order to produce dense ceramics. The inversion of double crucibles with the same chemical composition powders was employed during the sintering process in order to prevent volatilization.<sup>[1]</sup>

### 2.1.3 Electrode preparation

As demonstrated in Fig. 2-2, the well-sintered ceramics used for dielectric

measurements were polished to about 0.8 mm in thickness. After washing and drying, silver electrodes were coated on both surfaces and subsequently solidified at 650 °C.<sup>[2,3]</sup> Differently, the samples for ferroelectricity measurement are lapped to 0.15 mm in thickness and then plated with gold electrodes by vacuum evaporation with a diameter of 1.3 mm.



**Fig. 2-2** Well-sintered ceramics with electrodes for (a) dielectric measurements, (b) hysteresis  $P$ - $E$  measurements.

## 2.2 Characterization

### 2.2.1 Measurement of particle size distribution

The particle size distribution of pre-products after crushing was measured using the Microtrac UPA with distilled water as medium. Prior to the measurement, the powders were dispersed via ultrasonic treatment for 10 min with distilled water and dispersant.

### 2.2.2 Density determination

After polishing, the density of the sintered ceramic was measured according to the Archimedes method. The average density of three measurements were recorded. The principle of Archimedes method can be described as:<sup>[4,5]</sup>

$$\rho = \frac{m_0}{m_1 - m_2} \rho_w \quad (2-1)$$

where,  $m_0$  is quality of ceramic in air,  $m_1$  is quality of ceramic fully absorbed by water,  $m_2$  is quality of ceramic fully immersed in water,  $\rho_w$  is the density of deionized water.

The theoretical density was calculated from the X-ray diffraction data of  $(200)_{pc}$  and/or  $(002)_{pc}$  diffraction peaks, and the pseudocubic indication was used in this study. The calculation was based on Eqs. (2-2) and (2-3):<sup>[6-8]</sup>

$$2d \sin \theta = \lambda \quad (2-2)$$

$$d = \frac{\lambda}{2 \sin \theta} \quad (2-3)$$

where  $d$  is the inter-planar spacing related to the (hkl) crystal plane,  $\lambda$  is the wavelength of X ray (0.15418 nm). When a single  $(200)_{pc}$  peak was observed, the lattice parameter  $a$  and lattice volume  $V$  can be calculated as shown in Eqs. (2-4) and (2-5):<sup>[6,7]</sup>

$$a = 2 \times d_{200} \quad (2-4)$$

$$V = a^3 = 8 d_{200}^3 \quad (2-5)$$

When double peaks were demonstrated, these parameters should be calculated by:

$$a = 2 \times d_{200} \quad (2-6)$$

$$c = 2 \times d_{002} \quad (2-7)$$

$$V = a^2 c = 8 d_{200}^2 d_{002} \quad (2-8)$$

As a result, the theoretical density  $\rho_T$  should be calculated below:


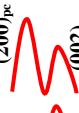

$$\rho_T = \frac{M}{N_A} \frac{1}{V} \quad (2-9)$$

where  $M$  is molecular weight of ceramic,  $N_A$  is the Avogadro constant,  $6.02214129 \times 10^{23} \text{ mol}^{-1}$ . Therefore, the relative density ( $\rho_R$ ) is calculated as follow:

$$\rho_R = \frac{\rho}{\rho_T} \times 100\% \quad (2-10)$$

### 2.2.3 X-ray diffraction (XRD) analysis

**Table 2-2** Characteristic diffraction peak of perovskite structure.<sup>[9-11]</sup>

$(200)_{pc}$ diffraction peak	Shape	Phase
Single		Rhombohedral: under $T_C$ Cubic: above $T_C$
Double weak-right		Orthorhombic
Double weak-left		Tetragonal

The crystal structure of well-sintered ceramics was identified via X-ray diffraction (XRD; Model RINT 2200; Rigaku Smart Lab) with Cu-K $\alpha$  radiation, working voltage of 40 kV and working current of 20 mA. The fine grounded powders were used for XRD measurement and the pseudocubic indication was used in this study.<sup>[6]</sup> This XRD consists of a heating unit that can be used to characterize the process of phase transformation during temperature change. The typical perovskite structures of cubic, rhombohedral, tetragonal and orthorhombic phase was confirmed by the shape of (200)<sub>pc</sub> diffraction peak around 45°.<sup>[9-11]</sup> The judgment method is shown in Table 2-2.

#### 2.2.4 Scanning electron microscope (SEM) analysis

The morphology and microstructure of samples were characterized by scanning electron microscopy (SEM; S-3000N; Hitachi). Prior to SEM imaging, all well-sintered samples were sputter-coated with a thin Au film in order to increase the electrical conductivity on the surface of samples as well as strengthen the quality of the image.

#### 2.2.5 Temperature-dependent dielectric performance measurement

The dielectric properties were measured using the impedance analyzer. The relative dielectric constant ( $\epsilon_r$ ) was calculated according to the principle of parallel plate capacitors, as shown below:<sup>[12-14]</sup>

$$\epsilon_r = \frac{4Ct_c}{\pi\epsilon_0 d^2} \quad (2-11)$$

where  $C$  is capacitance,  $t_c$  is thickness of ceramics,  $\epsilon_0$  represents permittivity in vacuum ( $8.854 \times 10^{-12}$  F/m), and  $d$  represents the diameter of electrode. Temperature-dependent dielectric constant and loss were measured during both heating and cooling processes with temperature range of 25-450 °C at heating and cooling rate of 1.5 °C/min.

#### 2.2.6 Frequency-dependent dielectric performance measurement

Dielectric constant and loss were measured at room temperature with a frequency range of 100 Hz - 1 MHz using the impedance analyzer. The dielectric constant was



calculated by Eq. (2-11).

### 2.2.7 Conductivity measurement

The conductance ( $G$ ) *versus* frequency was measured at room temperature using the impedance analyzer. The conductivity ( $\sigma$ ) was calculated by:<sup>[15-17]</sup>

$$\sigma = \frac{Gt_c}{s} \quad (2-12)$$

where  $t_c$  is the thickness of ceramics, and  $s$  represents the area of ceramics.

### 2.2.8 Ferroelectricity measurement

The hysteresis  $P$ - $E$  loops were measured under AC sine wave with the samples immersed in silicone oil. The measurement was applied with voltage sampling and then converted to the polarization value of the samples.

## References

- [1] B. Y. Zhang, J. G. Wu, X. J. Cheng, X. P. Wang, D. Q. Xiao, J. G. Zhu, X. J. Wang and X. J. Lou. *ACS Appl. Mater. Interfaces*, **5**, 7718, 2013.
- [2] T. Zheng, J. G. Wu, D. Q. Xiao and J. G. Zhu. *ACS Appl. Mater. Interfaces*, **7**, 5927, 2015.
- [3] R. Baba, T. Karaki and T. Fujii. *J. Adv. Dielectr.*, **6**, 1650008, 2016
- [4] A. B. Spierings, M. Schneider and R. Eggenberger. *Rapid Prototyp. J.*, **17**, 380, 2011.
- [5] C. Acott. *South Pacific Underwater Med. Soc.*, **29**, 39, 1999.
- [6] Y. Sakai, T. Futakuchi, T. Karaki and M. Adachi. *Jpn. J. Appl. Phys.*, **53**, 09PB07, 2014.
- [7] M. Ahtee and A. M. Glazer. *Acta Cryst. A*, **32**, 434, 1976
- [8] J. Tellier, B. Malic, B. Dkhil, D. Jenko, J. Cilensek and M. Kosec. *Solid State Sci.*, **11**, 320, 2009.
- [9] A. W. Hewat. *J. Phys. C*, **6**, 2559, 1973.
- [10] A. M. Glazer, S. A. Mabud and R. Clarke. *Acta Crystallogr. Sect. B*, **34**, 1060, 1978.
- [11] R. Wäsche, W. Denner, and H. Schulz. *Mater. Res. Bull.*, **16**, 497, 1981.
- [12] C. Ang, A. S. Bhalla, L. E. Cross. *Phys. Rev. B*, **64**, 184104, 2001.
- [13] X. H. Hao. *J. Adv. Dielectr.* **3**, 1330001, 2013.
- [14] A. Chauhan, S. Patel, R. Vaish and C. R. Bowen. *Materials*, **8**, 8009, 2015.
- [15] A. K. Jonscher. *Nature*, **267**, 7, 1977.
- [16] M. G. Bellino, D. G. Lamas and N. E. Walsöe de Reça. *Adv. Mater.*, **18**, 3005, 2006.
- [17] R. M. Pashley, M. Rzechowicz, L. R. Pashley and M. J. Francis. *J. Phys. Chem. B*, **109**, 1231, 2005.

## Chapter 3

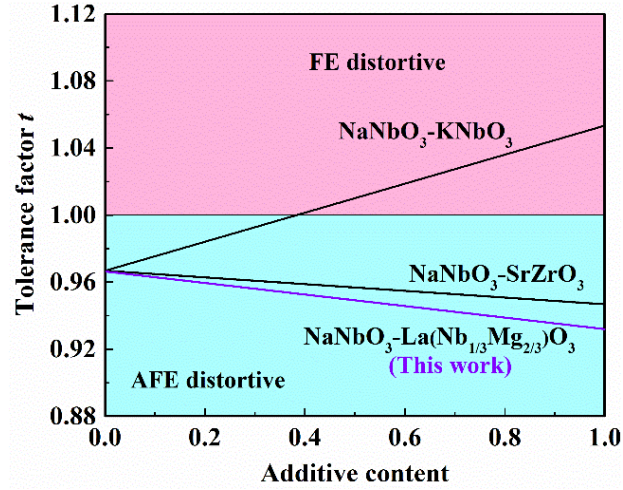
### Preparation and Study of $\text{NaNbO}_3\text{-La}(\text{Nb}_{1/3}\text{Mg}_{2/3})\text{O}_3$ Ceramics

#### 3.1 Introduction

Lead-based  $\text{PbZrO}_3$  (PZ) is a widely applied anti-ferroelectric (AFE) material with superior energy storage properties consisting of double hysteresis  $P$ - $E$  loops. However, the corresponding harm to human health and environment limits its wide applications. Therefore, the lead-free AFE  $\text{NaNbO}_3$  (NN) ceramics have attracted key attentions in recent years. In the case of NN ceramics, the metastable ferroelectric (FE) Q phase with  $P2_1ma$  space group destroys the stability of AFE phase.<sup>[1,2]</sup> Various researches have been conducted on the AFE-FE phase transition in NN-based ceramics.<sup>[3,4]</sup> All these studies highlight a major limitation of the critical phase transition behavior in NN-based ceramics, due to the relative stability of the AFE and FE structures.

The tolerance factor  $t$  is a critical factor to evaluate the packing of ions and crystal stability, therefore, it also plays an important role in stabilizing the AFE phase in NN ceramics.<sup>[5-7]</sup> A reduction in  $t$  can effectively stabilize the AFE phase in NN ceramics, which can narrow the hysteresis  $P$ - $E$  loops. In contrast, larger  $t$  values are beneficial to stabilizing a FE phase with enhanced polar distortions like the  $(\text{K},\text{Na})\text{NbO}_3$  systems.<sup>[5]</sup>

In this work,  $\text{La}(\text{Nb}_{1/3}\text{Mg}_{2/3})\text{O}_3$  (LNM) was employed to enhance anti-ferroelectricity in polycrystalline NN ceramics via decreasing the tolerance factor, as plotted in Fig. 3-1. The effects of additive content on phase transition behavior, dielectric properties and energy storage performance were studied.

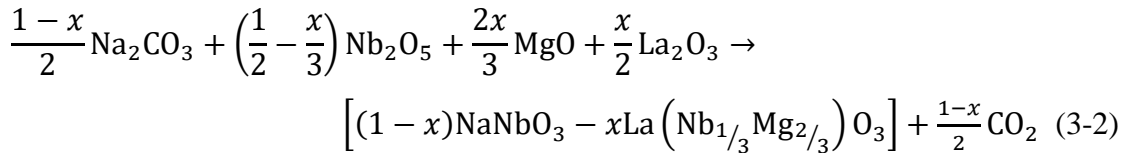
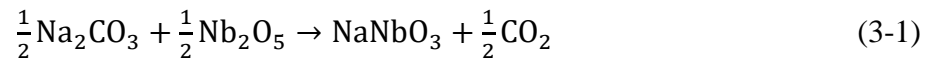


**Fig. 3-1** Plot of tolerance factor  $t$  versus dopant content to NN-based ceramics and the room temperature phase structure originated from theoretical analysis.<sup>[5]</sup>

### 3.2 Performance of $\text{NaNbO}_3\text{-La(Nb}_{1/3}\text{Mg}_{2/3}\text{)O}_3$ Ceramics

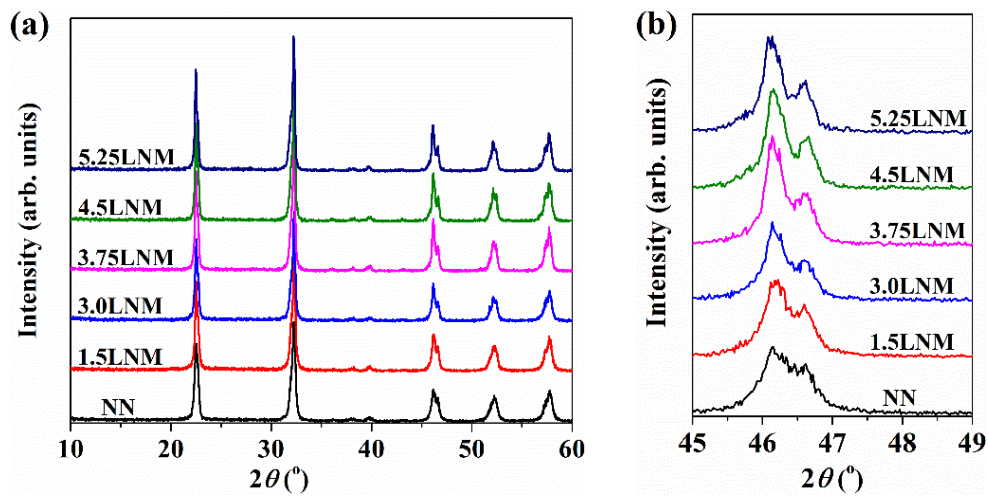
The binary  $(1-x)\text{NN-xLNM}$  ceramics were prepared using the solid-state method as described in section 2.1.2. Hereafter, the samples are abbreviated as NN and  $100x\text{LNM}$ , respectively. The calcination was carried out at  $950\text{-}1000\text{ }^\circ\text{C}$ , while the green bodies were sintered at  $1230\text{-}1350\text{ }^\circ\text{C}$ .

#### 3.2.1 Sintering performance of NN-LNM ceramics



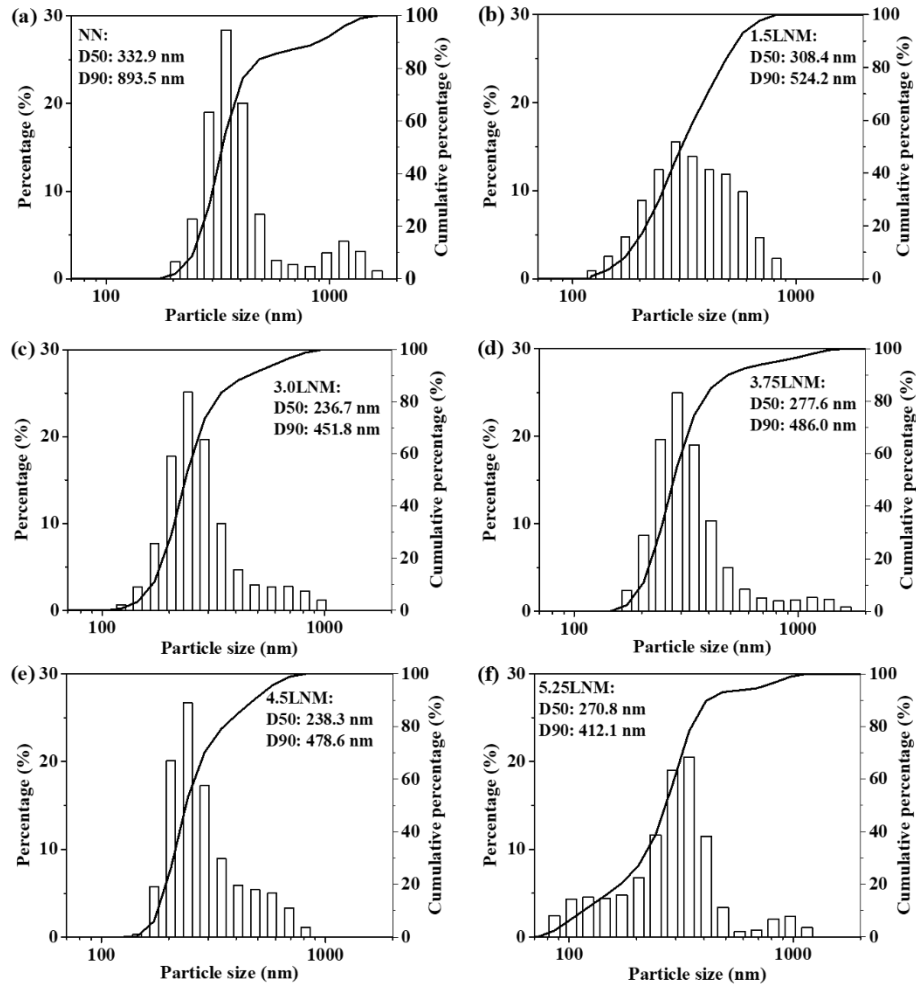
Calcination is an essential process for the preparation of ceramics to achieve the following purposes.<sup>[8]</sup> Firstly, free water is eliminated and carbonate is decomposed in order to effectively control deformation. Secondly, the calcination process can increase the compactness and uniformity of resulting ceramics. Finally, this process can

accelerate atom diffusion and form new chemical bonds prior to sintering. The solid-state reaction can be described using Eqs. (3-1) and (3-2). Figure 3-2 demonstrates the X-ray diffraction (XRD) patterns of pre-products after calcination. Observably, all pre-products possessed perovskite diffraction peaks, while the weak diffraction peaks showed a preliminary reaction (Fig. 3-2(b)). It reveals that the calcination temperature is appropriate.



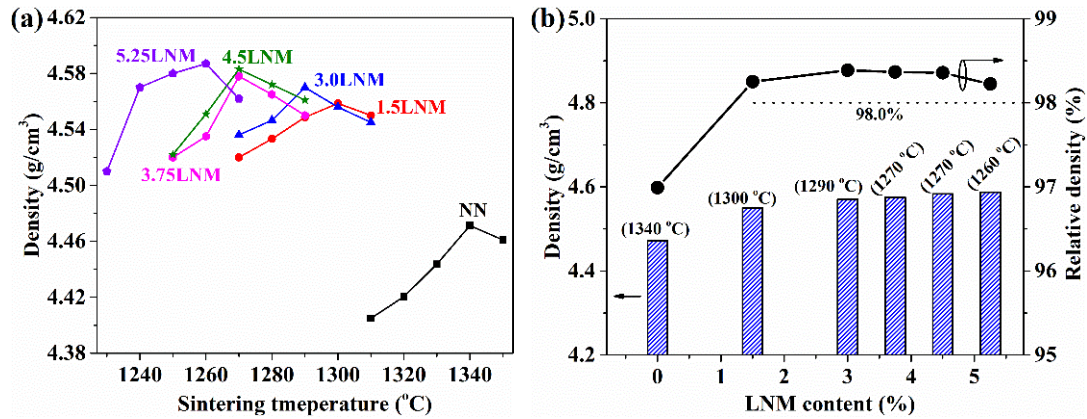
**Fig. 3-2** XRD patterns of NN-LNM pre-products for (a) 10-60°, (b) 45-49°.

Figure 3-3 displays the particle size distribution of pre-products after crushing. It can be found that the particle size of D90 decreased obviously with the addition of LNM. Meanwhile, a gradual reduction in D50 was observed. This may be caused by the octahedral distortion and pinning effect induced by  $\text{La}^{3+}$ .<sup>[9]</sup> And a reduction in particle size can effectively increase reactivity because the sintering driving force is inversely proportional to the particle size. As it is well known, the D90 values less than 900 nm are appropriate for NN-based ceramics, which can provide enough reactivity. Thus, all samples are suitable for sintering.



**Fig. 3-3** The Particle size of pre-products after crushing for (a) NN, (b) 1.5LNM, (c) 3.0LNM, (d) 3.75LNM, (e) 4.5LNM, and (f) 5.25LNM.

As shown in Fig. 3-4, LNM displayed positive effects on improving sintering performance. The optimum sintering temperature decreased from 1340 °C to 1260 °C when the LNM amount increased from 0 to 5.25%. In addition, both density and relative density were improved with the introduction of LNM, and the relative density of LNM-doped ceramics was higher than 98%. This is derived from the auxiliary effect of ion substitutions, which can create defects and cause lattice distortion, increasing the sintering driving force and promoting ion-exchange interactions.<sup>[9,10]</sup> Furthermore, the smaller particles can also enhance reactivity, consequently accelerating the sintering reaction.<sup>[10]</sup> The reduced sintering temperature can inhibit volatilization of sodium, improving electrical properties. In addition, the temperature range was also widened by the addition of LNM, which is beneficial to industrial production and application.

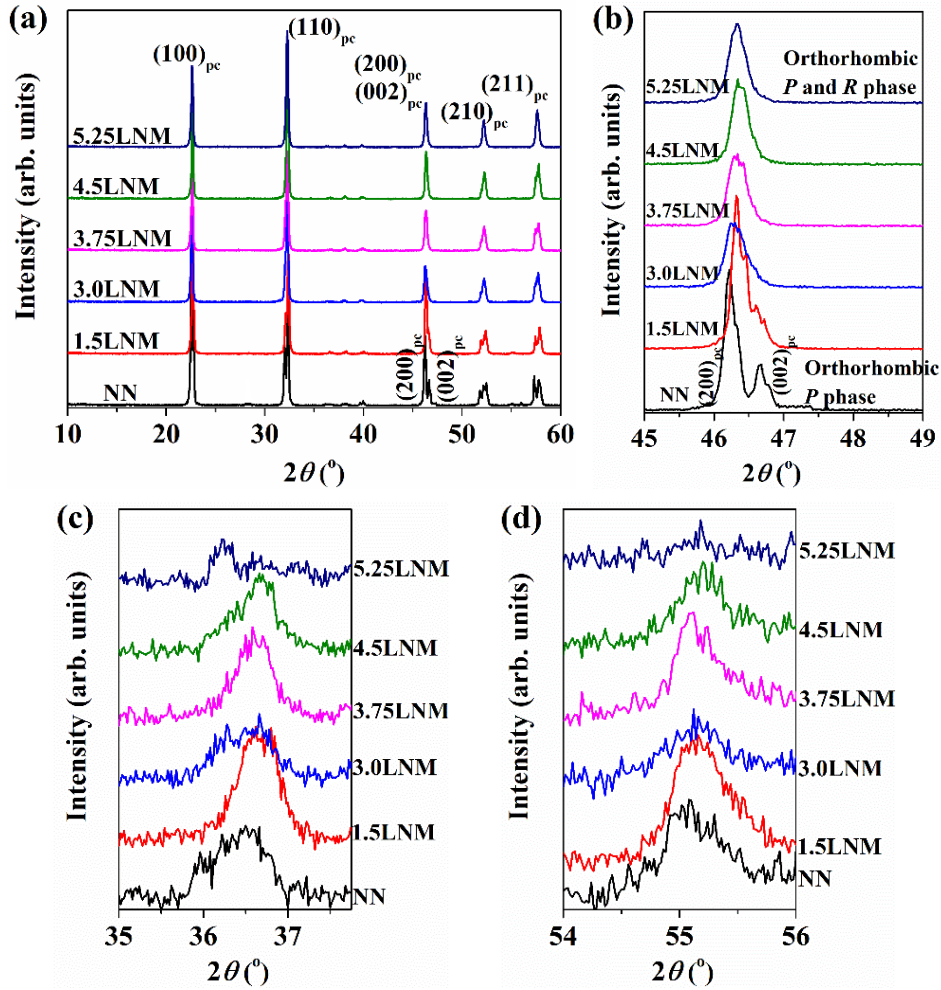


**Fig. 3-4** Sintering performance of NN-LNM ceramics for (a) Density against sintering temperature and (b) density and relative density of ceramics sintered at the optimal temperature.

### 3.2.2 Phase structure and microstructure of NN-LNM ceramics

Figure 3-5 exhibits the XRD patterns of NN-LNM ceramics sintered at the optimum temperatures. It is revealed that all samples possessed pure perovskite structures without any appreciable secondary impurity phases, indicating that  $\text{La}^{3+}$  and  $\text{Mg}^{2+}$  diffused into the NN lattice to form solid solutions. Similar ionic radii, complex crystal and coordination structures are beneficial to improve solid solubility. The magnified sections of the  $(002)_{\text{pc}}$  and  $(200)_{\text{pc}}$  reflection peaks demonstrate that the crystal structure was gradually transformed from orthorhombic  $P$  phase to a coexistence of orthorhombic  $P$  and  $R$  phase (Fig. 3-5(b)). This may be beneficial towards an enhanced energy storage performance via the phase transition. In Figs. 3-5(c) and 3-5(d), a close view of the XRD spectra corresponds to the  $(11\ 3/4)$  and  $(21\ 3/4)$  AFE superlattice diffraction of NN-based ceramics is displayed, locate at  $36.5^\circ$  and  $55.2^\circ$ , respectively.<sup>[6,7]</sup> The intensity of the characteristic AFE superlattice peaks were slightly improved when  $x \leq 4.5\%$ , meaning that the anti-ferroelectricity was enhanced caused by the decrease in tolerance factor  $t$  (Table 3-1).<sup>[7]</sup> Because a reduction in tolerance factor can alter the free energy configuration to benefit the nonpolar-polar switch.<sup>[5]</sup> In addition, the ion substitution may break the long-range ordered phase, beneficial for

short-range dipoles. However, these characteristic peaks were apparently different in 5.25LNM samples, the (11 3/4) superlattice peak was split into two peaks, while the (21 3/4) superlattice peak was obviously weakened. This also indicates the occurrence of orthorhombic AFE *R* phase.<sup>[13]</sup>

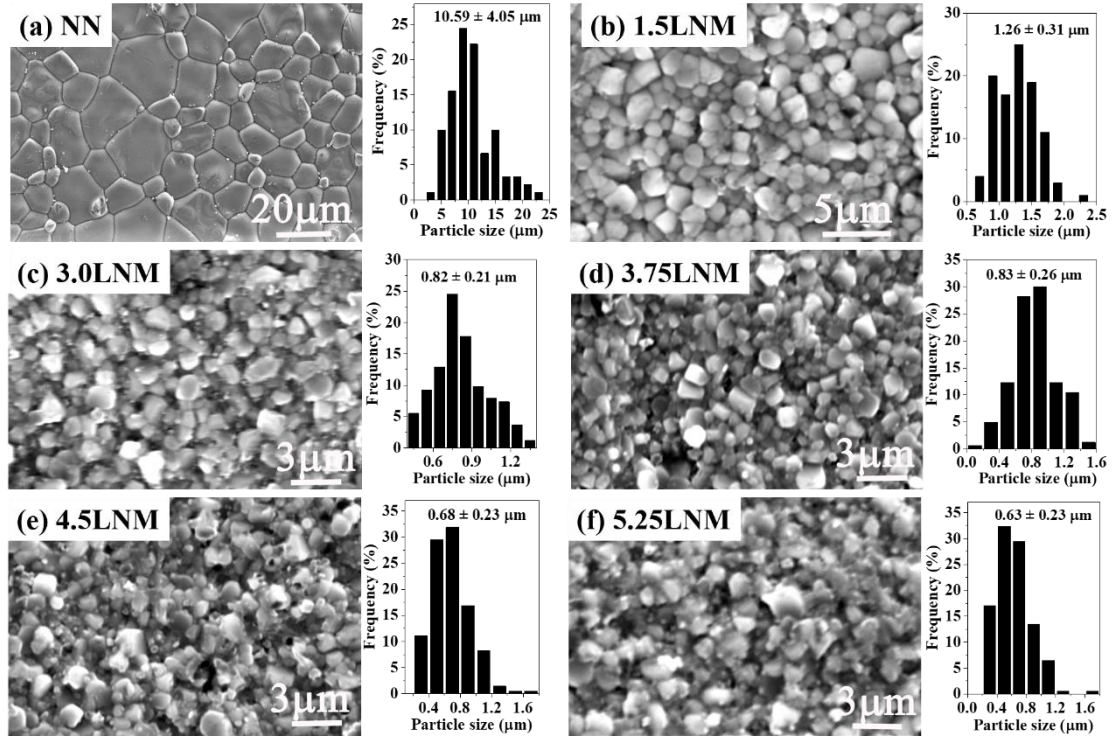


**Fig. 3-5** XRD patterns of NN-LNM ceramics for (a) 10-60°, (b) 45-49°, (c) (11 3/4) AFE superlattice diffraction, and (d) (21 3/4) AFE superlattice diffraction.

As shown in Fig. 3-6, all specimens show a dense structure with only few pores. The grain size ( $G_s$ ) decreased evidently and the microstructure was more uniform with the increase in LNM content. This is beneficial for advanced  $E_b$ , which is described as an exponential relationship:  $E_b \propto G_s^{-0.5}$ .<sup>[11]</sup> This can be interpreted by the effect of  $\text{La}_2\text{O}_3$  acting as a nucleating agent, which can promote the precipitation of targets and uniform distribution of grain size. According to the principle of similar radii,  $\text{La}^{3+}$  ions would



diffuse into A-site forming a donor dopant, producing more oxygen vacancies and consequently reducing the grain size.<sup>[12]</sup> In addition, a small amount of  $\text{La}^{3+}$  may accumulate at the crystal boundaries, acting as pinning effect inhibiting grain growth. The reduced sintering temperature would also decrease the grain size and inhibit volatilization of Na.



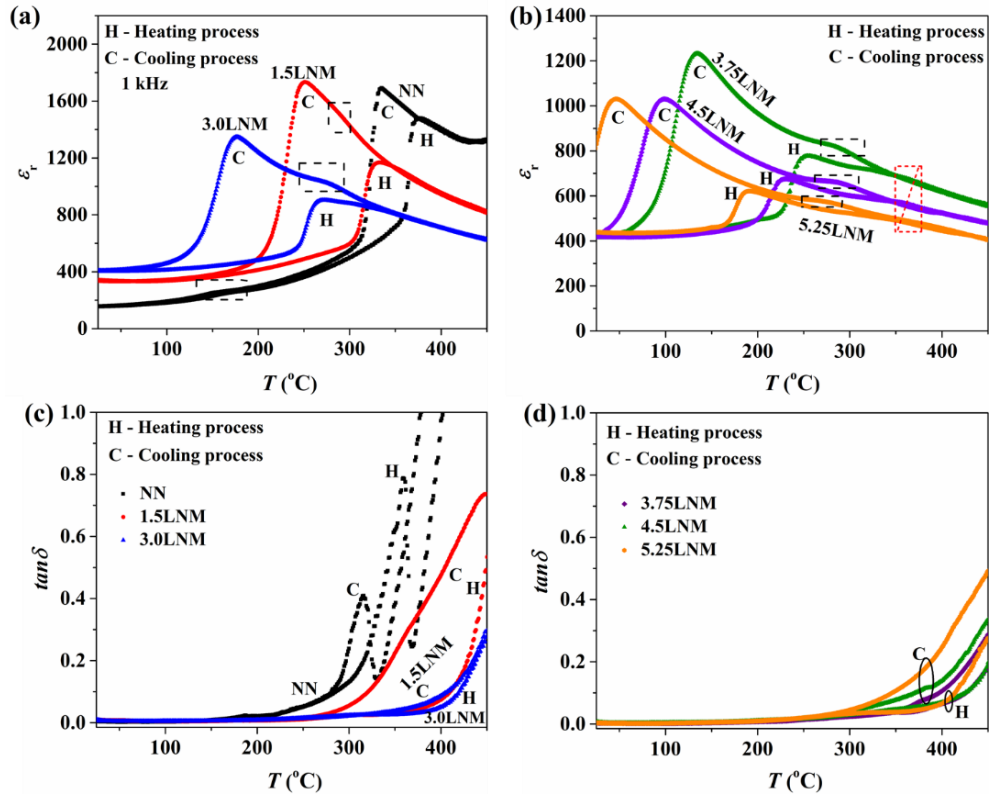
**Fig. 3-6** Microstructure and grain size distribution of NN-LNM ceramics for (a) NN, (b) 1.5LNM, (c) 3.0LNM, (d) 3.75LNM, (e) 4.5LNM, and (f) 5.25LNM.

### 3.2.3 Dielectric and phase transition behavior of NN-LNM ceramics

Figures 3-7(a, b) represent the dielectric constant ( $\epsilon_r$ ) of NN-LNM ceramics as a function of temperature, while Figs. 3-7(c, d) represent the dielectric loss ( $\tan\delta$ ) of NN-LNM ceramics as a function of temperature. The measurements were realized at 1 kHz during heating and cooling sweeps in the range of 25-450 °C. These ceramics possessed unique dielectric characteristics different from the piezoelectric and relaxor-ferroelectric ceramics, which manifested as obvious thermal hysteresis in both  $\epsilon_r$  and  $\tan\delta$ . This is responsible for the first-order AFE phase transition.<sup>[13]</sup> In NN ceramics,

there was a clear dielectric peak located at Curie temperature ( $T_C$ ) attributed to the AFE  $P$  to AFE  $R$  phase transition.<sup>[14,15]</sup> Moreover, the other anomaly was detected around 160 °C in pure NN ceramics, while LNM-doped ceramics showed no visible appearance. This may be caused by oxygen vacancies produced by volatilization of sodium. The ion substitution and reduced sintering temperature can inhibit this volatilization. Alternatively, another subtle dielectric anomaly (Fig. 3-7(b), red box in heating process) occurred above  $T_C$  when  $x \geq 3.75\%$ , which may be caused by a crystal distortion.<sup>[13]</sup> With the increase in additive content, the dielectric vertex temperature during the cooling process (defined as  $T_C'$ ) and  $T_C$  both shifted to lower temperatures. The temperature difference ( $\Delta T_C$ ) between  $T_C$  and  $T_C'$  was enlarged, as shown in Fig. 3-7 and Table 3-1. This is beneficial for the stabilization of AFE phase.

The room temperature (RT) dielectric constant ( $\epsilon_{r(RT)}$ ) increased slightly with the enlargement in LNM amount, while the RT  $\tan \delta$  maintained relatively low values (< 1%). This is induced by the effect of  $\text{La}^{3+}$  on particle size and crystal boundaries, given that there present no extrinsic domain contributions with AFE domain switching.<sup>[12]</sup> However, the maximum dielectric constant decreased gradually during the heating sweep as the additive content increased, while that during the cooling process showed an increase-decrease trend. Generally, the FE domains are difficult to polarize and are accompanied by large stress, while the AFE domains are more prone to polarization. The coexistence of different domains presents a great impact on dielectric properties.



**Fig. 3-7** Temperature dependent dielectric properties of NN-LNM ceramics for (a, b)  $\epsilon_r$ - $T$  curves and (c, d)  $\tan\delta$ - $T$  curves.

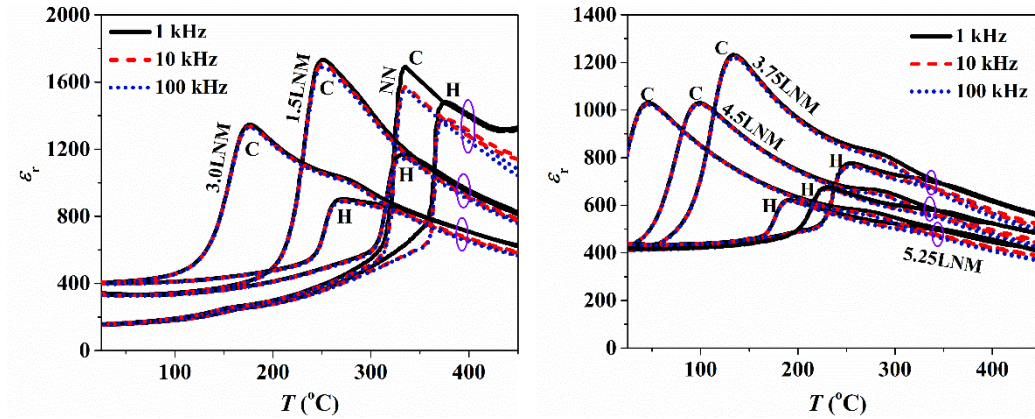
**Table 3-1.** Phase transition temperatures and RT dielectric properties of NN-LNM ceramics.

Sample	$T_C$ (°C)	$T_C'$ (°C)	$\Delta T_C$ (°C)	$\frac{\epsilon_r(\text{RT})}{\tan\delta(\%)}$		$t$
				At 1 kHz, RT		
NN	375	335	40	154	0.33	0.96707
1.5LNM	333	251	82	343	1.00	0.96655
3.0LNM	272	177	95	403	0.53	0.96603
3.75LNM	253	134	119	415	0.43	0.96577
4.5LNM	230	99	131	419	0.50	0.96551
5.25LNM	191	47	144	439	0.32	0.96525

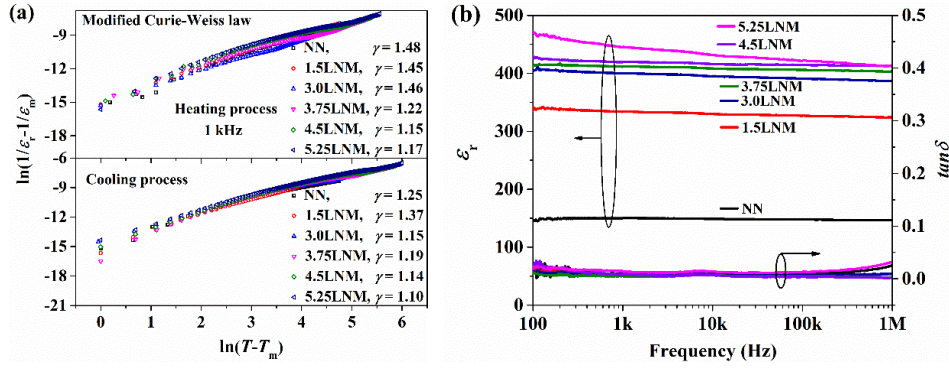
In addition, the influence of frequency on  $\epsilon_r$ - $T$  curves is demonstrated in Fig. 3-8. Both  $T_C$  and  $T_C'$  were independent on frequency, indicating no relaxor-ferroelectric aspects. To support this theory, the modified Curie-Weiss law is introduced:<sup>[16-18]</sup>

$$\frac{1}{\varepsilon_r} - \frac{1}{\varepsilon_m} = \frac{(T-T_m)^\gamma}{C} \quad (3-3)$$

where  $\varepsilon_m$  is the dielectric constant at  $T_C$  or  $T_C'$ ,  $T_m$  represents  $T_C$  or  $T_C'$ ,  $\gamma$  is the diffuseness parameter located between 1 and 2, and  $C$  is the Curie-Weiss constant. When  $\gamma$  is close to 1, it deviates from relaxor characteristics.<sup>[19]</sup> The extracted  $\gamma$  values at 1 kHz are fitted with Eq. (3-3) and the results are demonstrated in Fig. 3-9(a). The  $\gamma$  values during the cooling process were much smaller as compared to the heating process. During heating actions,  $\gamma$  presented an obvious reduction when LNM content increased, gradually approaching 1, signifying an enhanced AFE phase rather than the RFE phase. Furthermore, Fig. 3-9(b) plots  $\varepsilon_r$  and  $\tan\delta$  as functions of frequency at RT. Although the introduction of LNM displayed a negative influence on stability, all samples illustrated attractive frequency stability. The  $\varepsilon_r$  slightly reduced (< 6.0%), while  $\tan\delta$  featured relatively low values (< 3%) at a frequency range of 100 Hz-1 MHz.

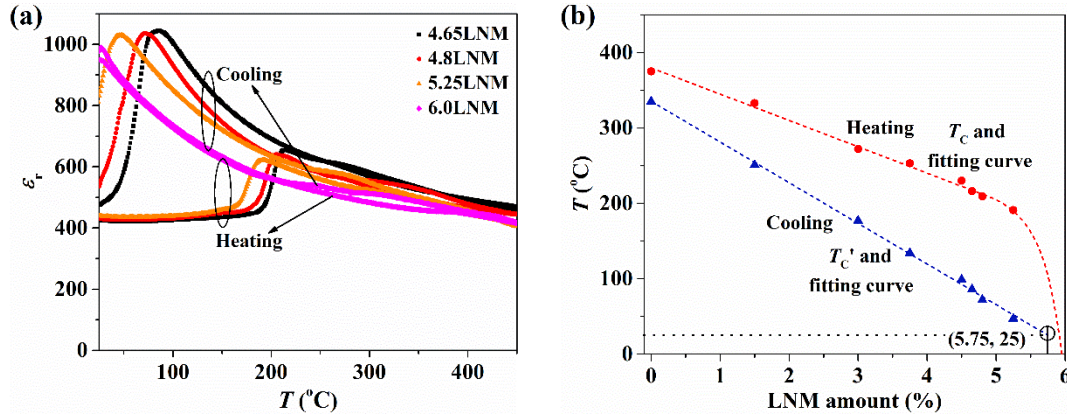


**Fig. 3-8**  $\varepsilon_r$ - $T$  curves of NN-LNM ceramics measured at different frequency.



**Fig. 3-9** NN-LNM ceramics for (a) Modified Curie-Weiss law at 1 kHz, (b) room temperature dielectric properties depend on frequency.

Noticeably,  $\epsilon_{r(RT)}$  was dependent on the thermal effect for 5.25LNM ceramics, as plotted in Fig. 3-8. After test process, the room temperature dielectric constant ( $\epsilon_{r(RT)'}^{\prime}$ ) was enlarged apparently, while others were reverted to their original state. For further investigation, three other samples containing different amount (4.65%, 4.8% and 6.0%) of LNM were introduced and their results are shown in Fig. 3-10(a) and Table 3-2. The difference in dielectric constant ( $\Delta\epsilon_{r(RT)} = \epsilon_{r(RT)} - \epsilon_{r(RT)'}^{\prime}$ ) obviously increased as LNM content increased when  $x > 4.5\%$  until  $T_C$  reached below 25 °C. Importantly,  $T_C$  suddenly reduced below 25 °C for 6.0LNM. Combined with above XRD analysis, the orthorhombic *P* phase was broken. We infer that this phase transition will become an irreversible reaction under surrounding conditions. After sintering, the sample was transformed into orthorhombic *R* phase during furnace temperature dropped to RT, and this structure remained at RT. Due to the varied ionic radius and charge, the ionic substitution must induce structural distortion and charge fluctuation. When these exceed a certain limit, a sudden transition of crystal structure will be induced. Therefore, there must be a “change point” between different structural phase induced by LNM, which is characterized by  $T_C' = 25$  °C. Figure 3-10(b) represents the fitting curves of  $T_C$  and  $T_C'$  depicted from  $\epsilon_r - T$  curves to describe the adding limitation. As seen,  $T_C'$  would be reduced to 25 °C when 5.75% LNM was applied. Considering the stability of phase structure, LNM used to stabilize AFE *P* phase should be controlled to be 5.0%.



**Fig. 3-10** (a)  $\epsilon_r$ - $T$  curves of 4.65LNM, 4.8LNM, 5.25LNM, 6.0LNM ceramics, (b) compositional dependent phase transition temperature depicted from  $\epsilon_r$ - $T$  curves (points in figure) and the fitting results (dotted line).

**Table 3-2.** RT dielectric constant and the difference measured at 1 kHz before and after dielectric measurements.

Sample	$\epsilon_{r(RT)}$	$\epsilon_{r(RT)}'$	$\Delta\epsilon_{r(RT)}$
4.5LNM	419	422	3
4.65LNM	425	475	50
4.8LNM	429	535	106
5.25LNM	439	831	392
6.0LNM	950	978	28

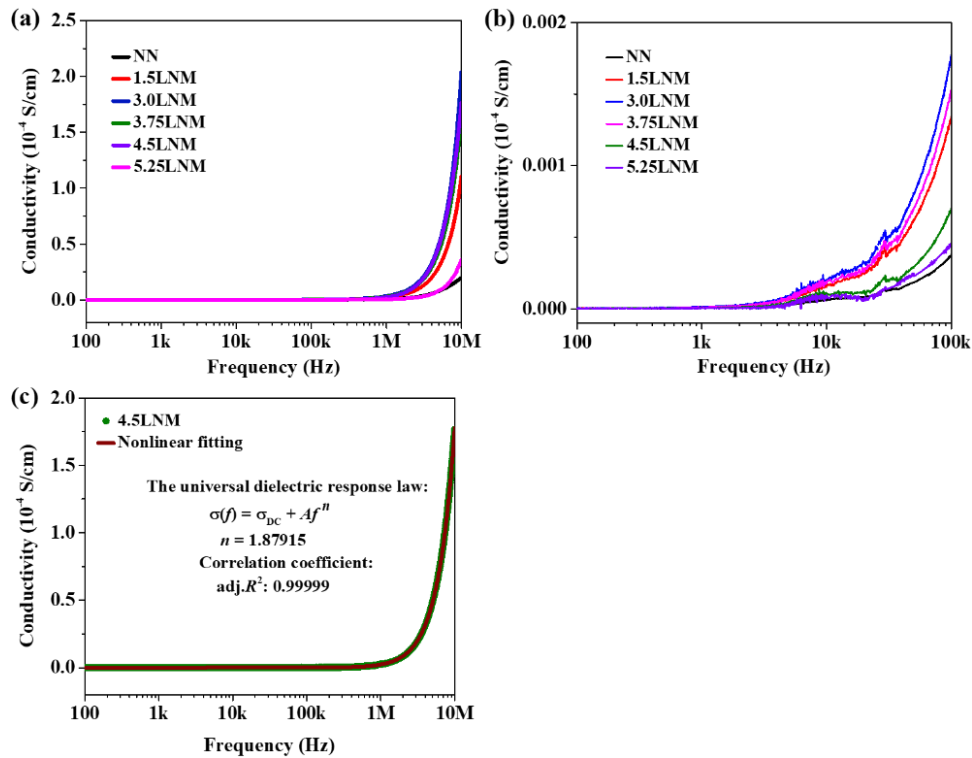
### 3.2.4 Energy storage performance of NN-LNM ceramics

To better understand the carrier migration behavior, the RT conductivity ( $\sigma$ ) was plotted against frequency, and the results are demonstrated in Fig. 3-11 and Table 3-3. At low frequency, the addition of LNM could reduce the conductivity as a whole (Fig. 3-5(b)), which is induced by the increase in conductance activation energy effected by oxygen vacancy concentration. Frequency-dependent  $\sigma$  can be applied to explore the conduction mechanism between nano-ceramics and conventional microcrystalline materials as described using the universal dielectric response law:<sup>[20,21]</sup>

$$\sigma(f) = \sigma_{DC} + Af^n \quad (3-4)$$



where  $f$  represents frequency,  $\sigma_{DC}$  is the DC conductivity,  $A$  and  $n$  are temperature dependent parameters. This is a universal property of materials, which is related to the hopping conduction dynamic.<sup>[20]</sup> When  $n < 1$ , the conduction mechanism involves a delocalized carrier motion with a big hop. When  $n > 1$ , the conduction mechanism presents a localized hopping within the specific area. The nonlinear fitting of 4.5LNM is displayed in Fig. 3-11(c), and the correlation coefficient  $adj.R^2$  is applied to evaluate the fitting results. The ideal fitting results are shown in Table 3-3. Observably, all samples possessed  $n > 1$ , indicating that the conduction existed as a localized hopping in the vicinity of their initial site. All samples exhibited nano-ceramic characteristics, this indicates the appearance of nano-domains, which is also beneficial for a larger breakdown electric field.



**Fig. 3-11** Room temperature conductivity depends on frequency of NN-LNM ceramics for (a) 100 Hz-10 MHz, (b) 100 Hz-100 kHz, and (c) the nonlinear fitting of 4.5LNM ceramics.

**Table 3-3** The conductivity ( $\sigma$ ) at 100 Hz, 100 kHz, and fitting results of the universal dielectric response law of NN-LNM ceramics.

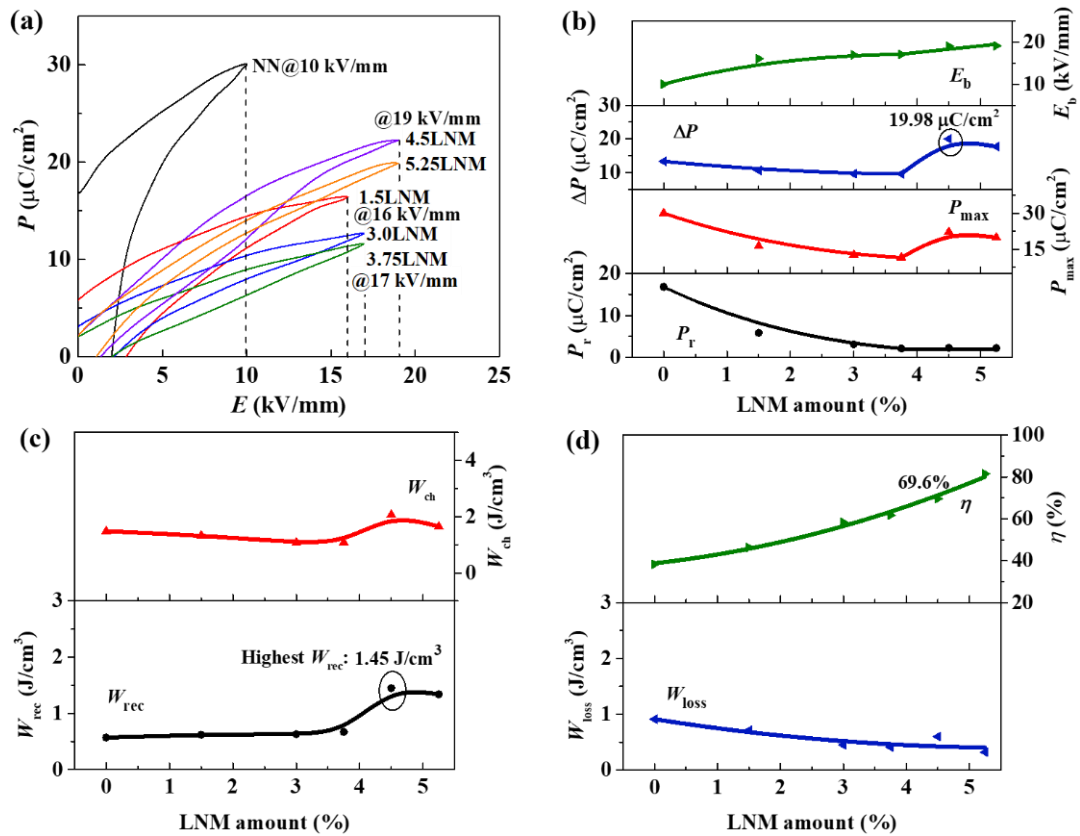
Sample	$\sigma$ (100 Hz) ( $10^{-10}$ S/cm)	$\sigma$ (100 kHz) ( $10^{-7}$ S/cm)	$n$	adj. $R^2$
NN	1.83	0.50	1.40	0.99921
1.5LNM	1.51	1.48	1.89	0.99964
3.0LNM	1.58	1.94	2.02	0.99966
3.75LNM	2.31	1.69	1.93	0.99980
4.5LNM	0.40	0.99	1.88	0.99999
5.25LNM	0.27	0.55	2.17	0.99941

Figure 3-12 reveals the energy storage performance of NN-LNM ceramics measured at 10 Hz, RT. The  $P$ - $E$  loops displayed different features induced by LNM, as shown in Fig. 3-12(a). NN and 1.5LNM ceramics showed typical well-saturated ferroelectric behavior with high residual polarization ( $P_r$ ) and large width of hysteresis loops (WHL), which is caused by the electric field-induced irreversible AFE-FE phase transition. Other ceramics showed reduced WHL and lower  $P_r$ , exhibiting a coexistence of FE and AFE phase. The crystal distortion and charge variation would enhance the disorder of microstructure, attenuating the electric field-induced FE phase. In addition, the introduction of LNM can alter the free energy configuration to suppress ferroelectricity. Therefore, the AFE-liked  $P$ - $E$  loops were induced by the interaction of polar and non-polar domains.

Influenced by the grain size, densification, and dielectric properties, the breakdown electric field strength ( $E_b$ ) increased gradually with the increase in LNM amount (Fig. 3-12(b)). Usually, higher electric field will improve the polarization values. However, the addition of LNM suppressed both  $P_r$  and the maximum polarization ( $P_{max}$ ) resulted from the reduced ferroelectricity and existence of ordered AFE phase. Therefore,  $P_r$ ,  $P_{max}$  and  $\Delta P$  ( $P_{max} - P_r$ ) gradually reached the rock bottom when 3.75% LNM was used. Conversely, the maximum  $\Delta P$  of 19.98  $\mu\text{C}/\text{cm}^2$  was achieved for 4.5LNM. However, there existed non-zero  $P_r$ , it was caused by a small number of polar nano regions (PNRs). These micro domains can exist in macro non-polar matrix.



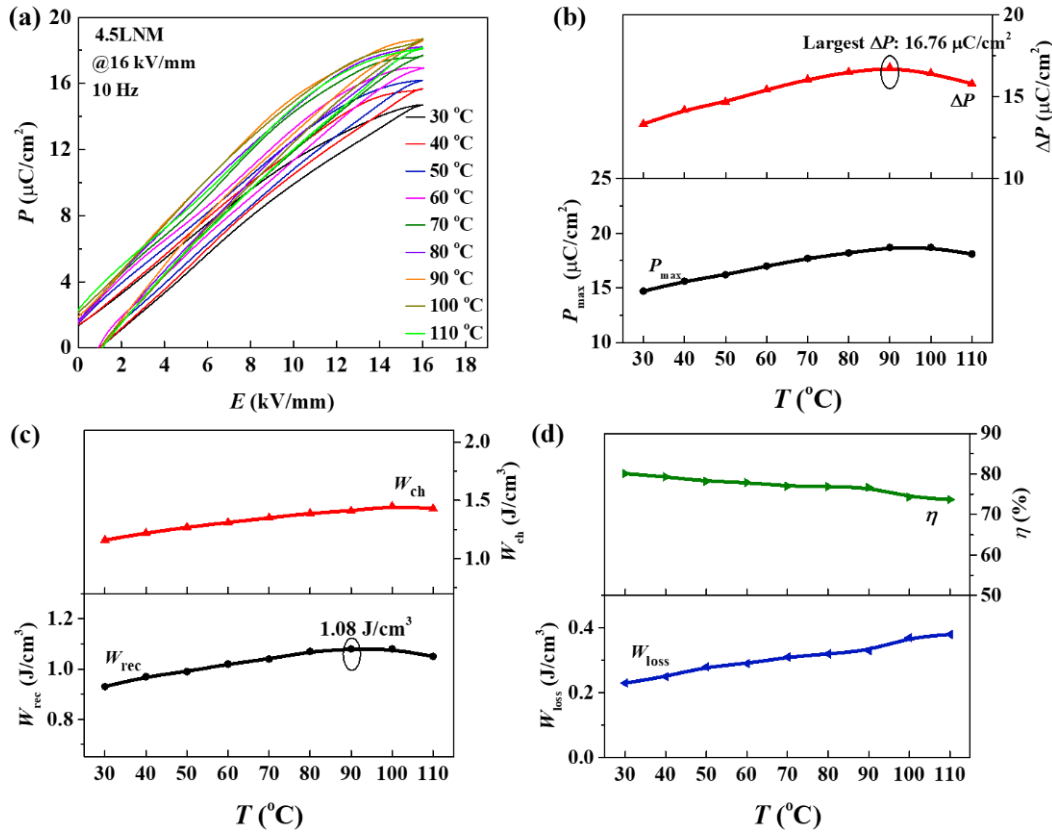
As a result, mainly influenced by  $\Delta P$  and the applied electric field, the recoverable energy storage density ( $W_{\text{rec}}$ ) slightly improved from  $0.57 \text{ J/cm}^3$  to  $0.67 \text{ J/cm}^3$  as LNM content increased from 0 to 3.75% (Fig. 3-12(c)). This is related to the competition between polar regions and non-polar regions. Then, it increased rapidly to the maximum value of  $1.45 \text{ J/cm}^3$  with efficiency ( $\eta$ ) of 69.6% for 4.5LNM at  $19.0 \text{ kV/mm}$ , as shown in Figs. 3-12(c, d). That is mainly induced by the enhanced anti-ferroelectricity and improved  $E_b$ . In addition, the charge energy density ( $W_{\text{ch}}$ ) showed a similar change with the  $\Delta P$ , while the energy loss ( $W_{\text{loss}}$ ) presented a downward trend.



**Fig. 3-12** Energy storage performance of NN-LNM ceramics for (a)  $P$ - $E$  hysteresis loops, (b) the  $P_r$ ,  $P_{\text{max}}$ ,  $\Delta P$ , and  $E_b$  values, (c) the  $W_{\text{rec}}$  and  $W_{\text{ch}}$ , and (d) the  $W_{\text{loss}}$  and  $\eta$ .

The temperature-dependent energy storage performance of 4.5LNM was studied at 30-110 °C, as presented in Fig. 3-13. The measures were carried out at 16.0 kV/mm and 10 Hz. As temperature increased, the  $P$ - $E$  loops were broadened slightly, but there exist no FE features (Fig. 3-13(a)). This signifies that the stable phase was constructed below 110 °C with slim  $P$ - $E$  loops and lower  $P_r$ . As shown in Fig. 3-13(b), both  $P_{\max}$  and  $\Delta P$  increased firstly and then reduced as temperature increased, simultaneously achieving the maximum values at 90 °C. This is due to the thermal motion of domains. Usually, the increase in temperature leads to intensified thermal motion, which is conducive to domain inversion. However, in a higher temperature region, the motion of domain becomes so active that partially ordered regions change into disordered, leading to a reduction in  $P_{\max}$ .

As a result, the best  $W_{\text{rec}}$  of 1.08 J/cm<sup>3</sup> with  $\eta$  of 77.5% was obtained at 90 °C, as shown in Figs. 3-13(c, d). However, the  $\eta$  presented a declining trend as the WHL was broadened with the increase in temperature. That means the PNRs are more active at high temperatures. In addition, both  $W_{\text{ch}}$  and  $W_{\text{loss}}$  showed a gradual growth as temperature increased. In addition, there existed 8.0% reduction in  $\eta$ , while  $W_{\text{rec}}$  displayed a fluctuation of 13.9%, which still need further improvement.



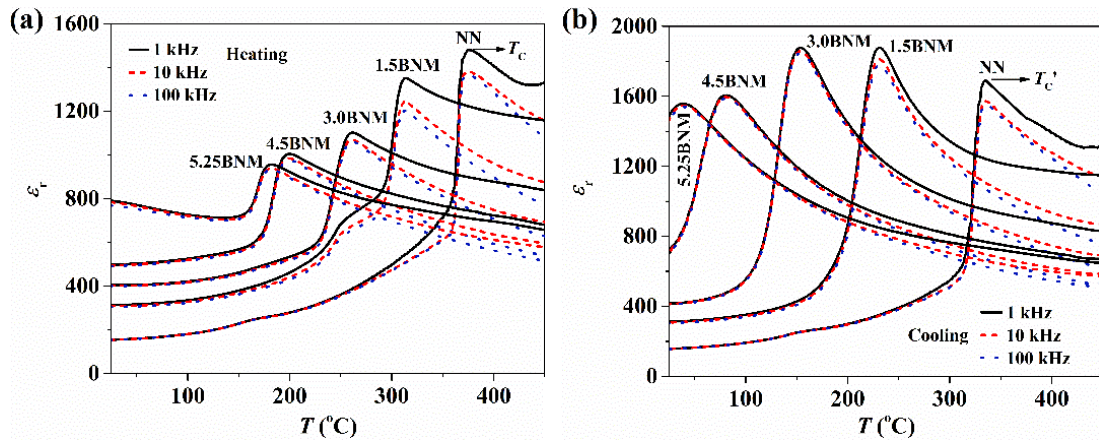
**Fig. 3-13** Temperature dependence of energy storage performances of 4.5LNM ceramics for (a)  $P$ - $E$  loops, (b) the  $P_{\max}$  and  $\Delta P$  values, (c) the  $W_{\text{rec}}$  and  $W_{\text{ch}}$  values, and (d) the  $W_{\text{loss}}$  and  $\eta$  values.

Although the double  $P$ - $E$  loops were not observed, which is mainly because the  $E_b$  cannot reach the phase transition electric field strength. Attractively, well narrowed  $P$ - $E$  loops with relatively low  $P_r$  were observed. Combined with other AFE characteristics, it can be inferred that the AFE phase has been stabilized at RT. Therefore, it is referred to as AFE phase in this work. And there exists no phenomenon contrary to the inference. In addition, the AFE-liked  $P$ - $E$  loops are beneficial for energy storage.

### 3.3 Influences of Tolerance Factor on Phase Transition in Another System

To further understand the influences of tolerance factor  $t$  on phase transition behavior,  $(1-w)\text{NaNbO}_3$ - $w\text{Bi}(\text{Nb}_{1/3}\text{Mg}_{2/3})\text{O}_3$  was also studied, which is abbreviated as  $100_w\text{BNM}$ . The  $\varepsilon_r$  as a function of temperature is presented in Fig. 3-14. The phase

transition temperatures, dielectric constant as well as tolerance factor  $t$  are displayed in Table 3-4. Similar behavior was observed in the first-order AFE phase transition with obvious thermal hysteresis. And both  $T_C$  and  $T_C'$  decreased sharply with the increase in  $\text{Bi}(\text{Nb}_{1/3}\text{Mg}_{2/3})\text{O}_3$  amount, leading to an improvement in  $\Delta T_C$ . As tolerance factor decreased to 0.96684,  $T_C$  and  $T_C'$  were reduced to 182 °C and 39 °C, respectively, with an improved  $\Delta T_C$  of 143 °C.



**Fig. 3-14** Temperature dependent  $\varepsilon_r$  curves of 100wBNM ceramics for (a) heating process and (b) cooling process.

**Table 3-4** Phase transition temperatures, tolerance factor  $t$ , and RT  $\varepsilon_r$  measured at 1 kHz before and after the dielectric measurement.

Sample	$T_C$ (°C)	$T_C'$ (°C)	$\Delta T_C$ (°C)	$\varepsilon_{r(\text{RT})}$	$\varepsilon_{r(\text{RT})}'$	$\Delta \varepsilon_{r(\text{RT})}$	$t$
NN	375	335	40	154	157	3	0.96707
1.5BNM	313	231	82	313	314	1	0.96701
3.0BNM	262	154	108	405	416	11	0.96694
4.5BNM	200	81	119	497	702	205	0.96688
5.25BNM	182	39	143	793	1488	695	0.96684

### 3.4 Summary

The perovskite  $(1-x)\text{NN}-100x\text{LNM}$  solid solutions with dense and uniform microstructure were successfully prepared by the conventional method. Although the

double  $P$ - $E$  loops are not observed under the lower electric field ( $\leq 19.0$  kV/mm), it is temporarily judged as AFE phase according to the unique behaviors. LNM could effectively promote sintering performance and stabilize the AFE phase in NN ceramics, which is resulted from the decrease in tolerance factor. The addition of LNM significantly influences the phase transition behavior and thermal hysteresis phenomenon. The  $T_C$  decreases from 375 °C to 192 °C and the  $T_C'$  decreases from 335 °C to 47 °C. And there also exists an adding limitation (5.75%) for the stabilization of AFE  $P$  phase. Furthermore, the dielectric properties are promoted upon the introduction of LNM as a result of the smaller particles, dense crystal boundaries. The lead-free bulk 4.5LNM ceramics exhibit the optimum  $W_{\text{rec}}$  of 1.45 J/cm<sup>3</sup> with  $\eta$  of 69.6% under a low electric field of 19.0 kV/mm. It is a feasible approach to strengthen the AFE phase by reducing tolerance factor in both NN-LNM and NN-BNM binary systems. Indeed, the prepared 0.955NN-0.045LNM ceramics are highly promising in electrostatic energy storage capacitors. However, there is a need for further improvement in RT  $W_{\text{rec}}$ ,  $\eta$  and thermal stability.

## References

- [1] T. Arioka, H. Taniguchi, M. Itoh, K. Oka, R. P. Wang and D. S. Fu. *Ferroelectrics*, **401**, 51, 2010.
- [2] R. H. Dungan and R. D. Golding. *J. Am. Ceram. Soc.*, **47**, 4, 1964.
- [3] D. S. Fu, T. Arioka, H. Taniguchi, T. Taniyama and M. Itoh. *Appl. Phys. Lett.*, **99**, 012904, 2011.
- [4] Y. H. Xu, W. Hong, Y. J. Feng and X. L. Tan. *Appl. Phys. Lett.*, **104**, 052903, 2014.
- [5] H. Shimizu, H. Guo, S. E. Reyes-Lillo, Y. Mizuno, K. M. Rabe and C. A. Randall. *Dalton Trans.*, **44**, 10763, 2015.
- [6] H. Guo, H. Shimizu, Y. Mizuno and C. A. Randall. *J. Appl. Phys.*, **117**, 214103, 2015.
- [7] L. Gao, H. Guo, S. Zhang and C. A. Randall. *J. Appl. Phys.*, **120**, 204102, 2016.
- [8] X. G. Tang, K. H. Chew, and H. L. W. Chan. *Acta Mater.*, **52**, 5177, 2004.
- [9] Y. R. Cui, C. L. Yuan, X. Y. Liu, X. Y. Zhao and X. Shan. *J. Mater. Sci.: Mater. El.*, **24**, 654, 2013.
- [10] Y. Liu, Z. S. Zheng, Y. L. Li, K. B. Xi, Y. S. Mi, W. S. Kang and R. J. Zhao. *J. Mater. Sci.: Mater. El.*, **30**, 21316, 2019.
- [11] T. Tunkasiri and G. Rujijanagul. *J. Mater. Sci. Lett.*, **15**, 1767, 1996.
- [12] W. S. Kang, Z. S. Zheng, Y. L. Li, R. J. Zhao, W. X. Dun and Y. F. Wang. *J. Mater. Sci.: Mater. El.*, **30**, 2743, 2019.
- [13] S. K. Mishra, R. Mittal, V. Y. Pomjakushin and S. L. Chaplot. *Phys. Rev. B*, **83**, 134105, 2011.
- [14] G. Shirane, R. Newnham and R. Pepinsky. *Phys. Rev.*, **96**, 581, 1954.
- [15] H. D. Megaw. *Ferroelectrics*, **7**, 87, 1974.
- [16] R. E. Newnham and L. E. Cross. *MRS Bulletin*, **30**, 845, 2005.
- [17] A. Dixit, S. B. Majumder, R. S. Katiyar and A. S. Bhalla. *Appl. Phys. Lett.* **82**, 2679, 2003.
- [18] K. Uchino and S. Nomura. *Ferroelectrics*, **44**, 55, 1982.

- [19] J. L. Li, F. Li, Z. Xu and S. J. Zhang. *Adv. Mater.*, **30**, 1802155, 2018.
- [20] A. K. Jonscher. *Nature*, **267**, 7, 1977.
- [21] M. G. Bellino, D. G. Lamas and N. E. Walsøe de Reça. *Adv. Mater.*, **18**, 3005, 2006.

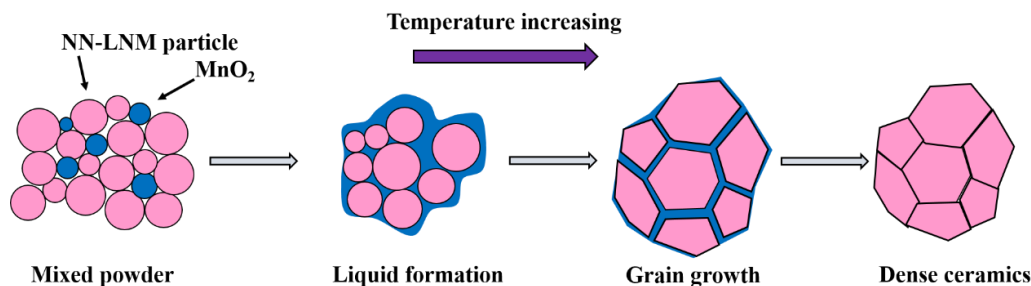
## Chapter 4

### Effect of MnO<sub>2</sub> Dopant on Properties of NN-LNM Ceramics

#### 4.1 Introduction

For lead-free ceramic-based dielectric capacitors, large residual polarization ( $P_r$ ), small maximum polarization ( $P_{\max}$ ) and low breakdown electric field strength ( $E_b$ ) hinder the improvement of energy storage properties.<sup>[1,2]</sup> In addition, NaNbO<sub>3</sub> (NN)-based ceramics are usually difficult to densify through conventional sintering under a pressure less condition because of their poor sinterability, which obviously obstructs the improvement in  $E_b$ . At high temperatures, the serious evaporation of alkaline element leads to an imbalance in chemical stoichiometry, resulting in a degradation in resistivity and other electrical properties. To solve these problems, there exist mainly two approaches. One involves improvements in sintering methods, including a spark plasma sintering method<sup>[3-5]</sup> or a hot press sintering process<sup>[6,7]</sup>. However, the special sintering methods are not only complicated but also expensive, which is unsuitable for large-scale promotion. As a comparison, the other approach, which is quietly easy to implement, involves the addition of sintering aids. There exist researches related to the improvements in sinterability and electrical properties through adding MnO<sub>2</sub><sup>[8,9]</sup>, CuO<sup>[10]</sup> and NiO<sup>[11]</sup>. The sintering aids will provoke a liquid phase to densify samples, and the sintering mechanism is illustrated in Fig. 4-1.<sup>[12]</sup> For example, Mn-doped (K<sub>0.5</sub>Na<sub>0.5</sub>)NbO<sub>3</sub>-based ceramics was fabricated at a lower temperature with enhanced properties, revealing that MnO<sub>2</sub> possesses excellent softening property.<sup>[8]</sup>





**Fig. 4-1** Schematic diagram of liquid phase sintering.<sup>[12]</sup>

As well known,  $\text{MnO}_2$  is not only an effective sintering aid for densification, but also an acceptor dopant for improving electrical properties.<sup>[13]</sup> During sintering process, Mn shows sliding valences from  $\text{Mn}^{2+}$ ,  $\text{Mn}^{3+}$  to  $\text{Mn}^{4+}$  when it is employed to replace B-site ions, so the crystallinity and microstructure are also affected.<sup>[14,15]</sup> Generally, the mechanical and electrical properties are closely related to the microstructure, however, there still exists the contradiction in the doping mechanism, especially for the regions above solubility limit.<sup>[16]</sup> In addition, the incorporation of Mn can effectively promote the formation of defective dipoles, which can reduce carrier migration and improve the reliability. Therefore,  $\text{MnO}_2$  was applied in  $0.955\text{NaNbO}_3\text{-}0.045\text{La}(\text{Nb}_{1/3}\text{Mg}_{2/3})\text{O}_3$  (0.955NN-0.045LNM) ceramics as a sintering aid to enhance the sintering and energy storage performance. And the effects of  $\text{MnO}_2$  amount on crystal structure, dielectric properties as well as energy storage performance were also investigated in this chapter.

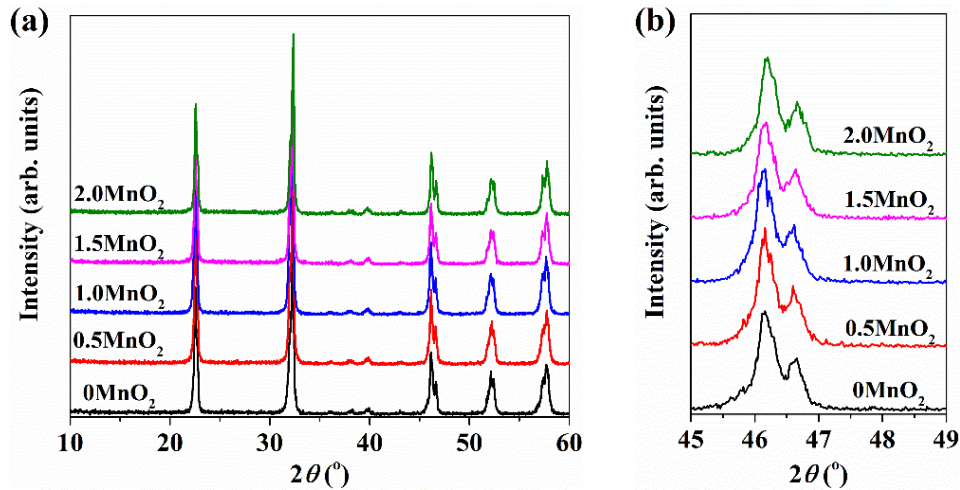
## 4.2 Performance of $\text{MnO}_2$ -Doped NN-LNM Ceramics

$\text{MnO}_2$  was applied as a sintering aid in  $0.955\text{NaNbO}_3\text{-}0.045\text{La}(\text{Nb}_{1/3}\text{Mg}_{2/3})\text{O}_3\text{-}y(\text{mole})\text{MnO}_2$  ceramics using the solid-state method as described in Section 2.1.2. The ceramics are abbreviated as  $100y\text{MnO}_2$  hereafter. The calcination was carried out at  $900\text{-}950\text{ }^\circ\text{C}$ , while the green bodies were sintered at  $1180\text{-}1290\text{ }^\circ\text{C}$ .

### 4.2.1 Effect of $\text{MnO}_2$ dopant on sintering performance

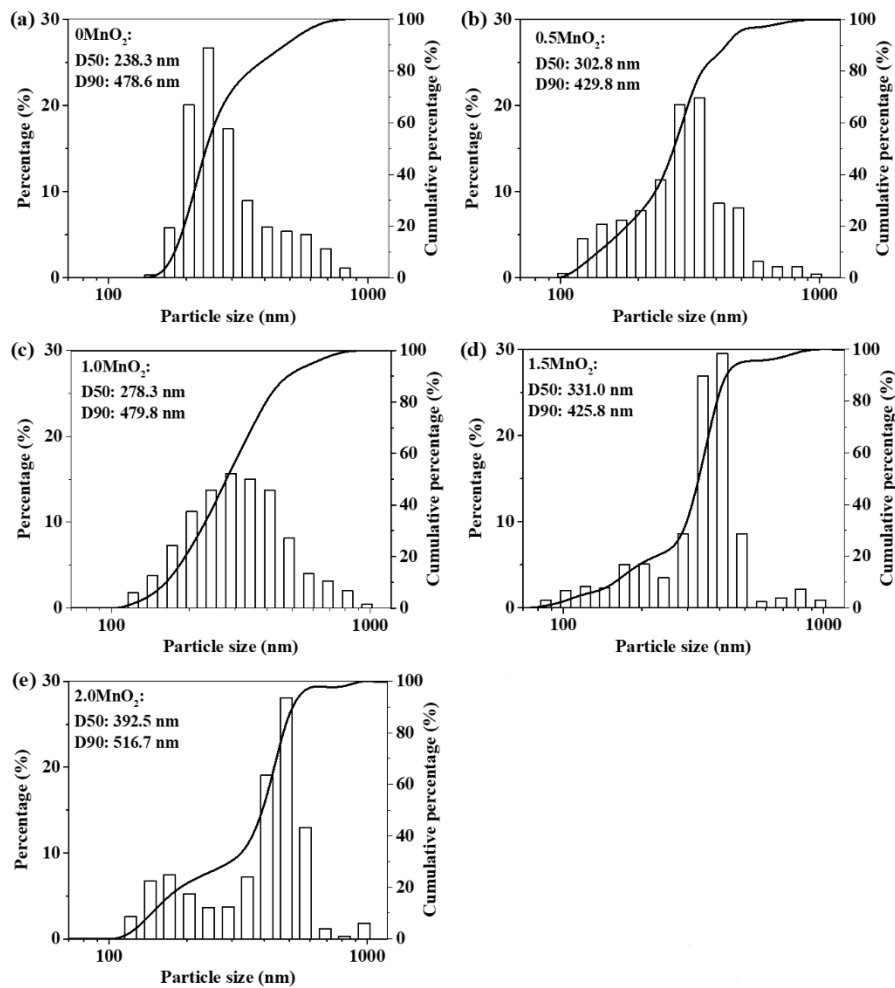
After calcination, all the pre-products demonstrated characteristic perovskite diffraction peaks without any diffraction peaks of reactants, as shown in Fig. 4-2. It is

able to avoid environmental impact in the next operations because  $\text{Na}_2\text{CO}_3$  is very deliquescent. Figure 4-2(b) displays the magnified section, all samples showed passivated double diffraction peaks, presenting an incomplete reaction. All these details certify that the calcination temperature is suitable, which can provide appropriate reaction driving force. This can reduce sintering temperature and inhibit deformation.



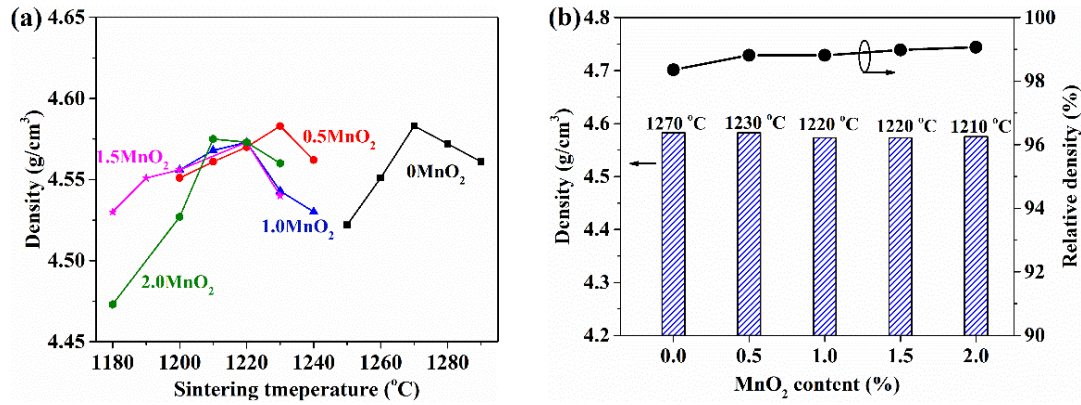
**Fig. 4-2** XRD (X-ray diffraction) patterns of  $100y\text{MnO}_2$  pre-products for (a)  $10\text{-}60^\circ$ , (b)  $45\text{-}49^\circ$ .

As well known, the particle size shows an important influence on the preparation of ceramics, which in turn affects the final properties. Smaller particles can provide more reactivity for sintering and decrease the sintering temperature. Therefore, a D90 within 900 nm is acceptable for next sintering for NN-based systems. The particle size distribution of pre-products after crushing is displayed in Fig. 4-3. The particle size of all samples was well distributed with smaller D90 around 500 nm.



**Fig. 4-3** The Particle size of  $100y\text{MnO}_2$  pre-products after crushing for (a)  $0\text{MnO}_2$ , (b)  $0.5\text{MnO}_2$ , (c)  $1.0\text{MnO}_2$ , (d)  $1.5\text{MnO}_2$ , and (e)  $2.0\text{MnO}_2$ .

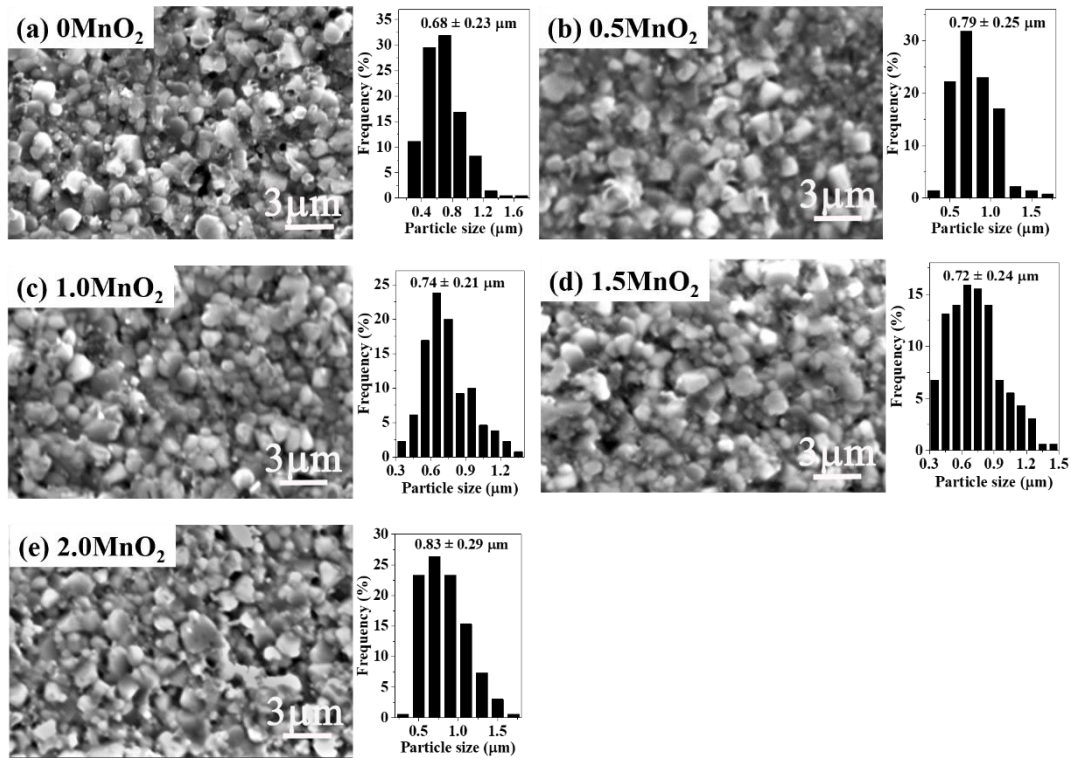
$\text{MnO}_2$  presents a lower melting point ( $535\text{ }^\circ\text{C}$ ) as compared with other reactants, it must melt forming a eutectic liquid at the sintering temperatures ( $> 1100\text{ }^\circ\text{C}$ ).<sup>[8,13]</sup> The sintering process changed from solid-state sintering to the coexistence of solid-state sintering and liquid-phase sintering. The sintering temperature can be greatly reduced due to the higher mass transfer rate of liquid phase, as shown in Fig. 4-4. In addition, the crystal distortion and charge compensation can also affect the sintering process. Therefore, the optimum sintering temperature was decreased from  $1280\text{ }^\circ\text{C}$  to  $1210\text{ }^\circ\text{C}$ , and the temperature range of full densification was also slightly widened. The measured density slightly decreased when  $\text{MnO}_2$  was added, while the relative density showed a gradual growth. This may be caused by the imbalance of ion ratio and charge in crystal lattice. And, all samples were well densified with the relative density exceeds 98%.



**Fig. 4-4** Sintering performance of 100yMnO<sub>2</sub> ceramics for (a) density *versus* sintering temperature, (b) density and relative density of ceramics sintered at the optimal temperature.

#### 4.2.2 Effect of MnO<sub>2</sub> dopant on phase structure and microstructure

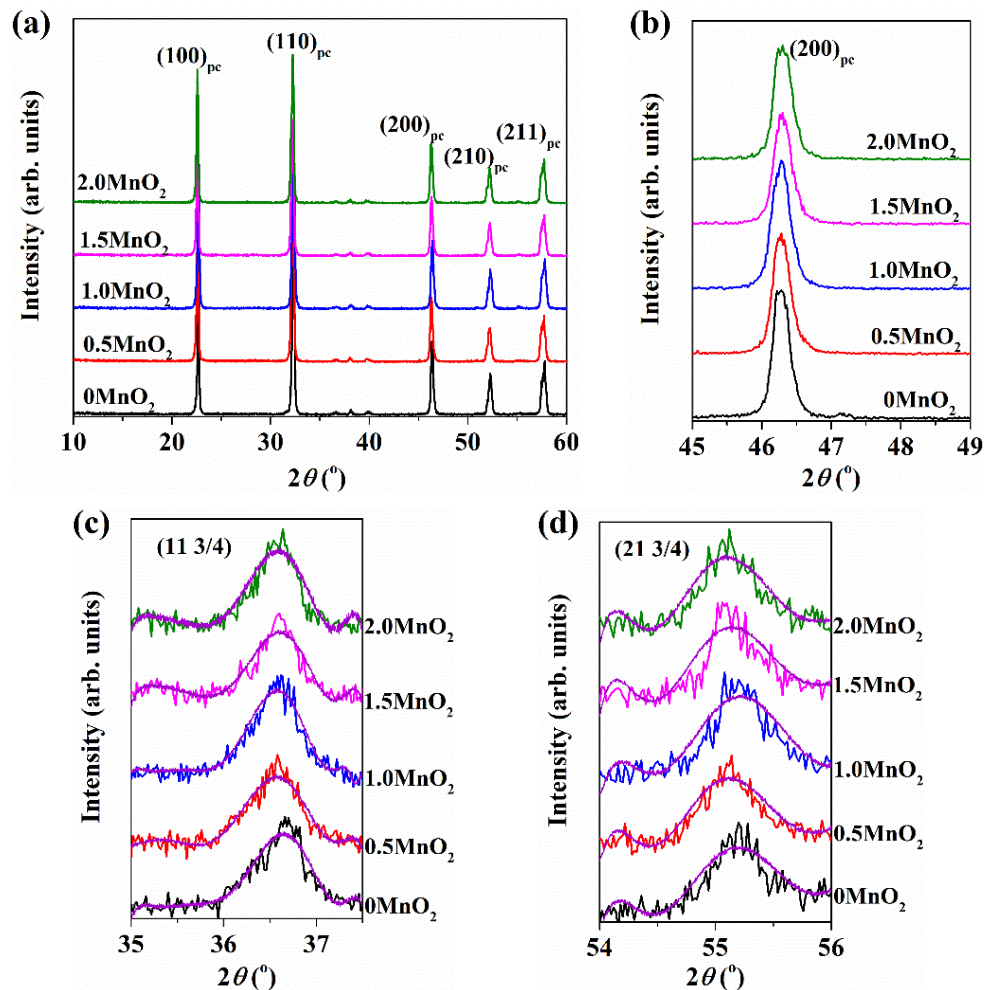
In Fig. 4-5, the microstructure and particle size distribution are displayed. The reduced sintering temperature can inhibit grain growth, conversely, the liquid phase is favorable to that. Therefore, a slight increase in grain size took place with the addition of MnO<sub>2</sub>, which is synthetically influenced by above two factors. Nevertheless, all samples possessed relatively small particles (< 1.0 μm). And all specimens were well densified with only few pores, and homogeneous microstructure was observed, benefiting to the enhancement in electrical properties and  $E_b$ .



**Fig. 4-5** Microstructure and particle size distribution of MnO<sub>2</sub>-doped ceramics for (a) 0MnO<sub>2</sub>, (b) 0.5MnO<sub>2</sub>, (c) 1.0MnO<sub>2</sub>, (d) 1.5MnO<sub>2</sub>, (e) 2.0MnO<sub>2</sub>, and (f) average grain size *versus* MnO<sub>2</sub> content.

The XRD patterns of MnO<sub>2</sub>-doped ceramics are exhibited in Fig. 4-6, and the pure perovskite structures without any appreciable secondary phase were observed in all samples. There must be a limit for additional aids. Beyond this limit, the impurity phase will accumulate at the grain boundaries, weakening the electrical properties. In this work, the small addition amount of MnO<sub>2</sub> showed no effect on the crystal structure. Furthermore, the magnified sections of (200)<sub>pc</sub> reflection peaks demonstrate passivated singlet, indicating an orthorhombic *P* phase, as shown in Fig. 4-6(b). A close view of XRD spectra around 36.5° and 55.2° is displayed in Figs. 4-6(c, d), which corresponds to the (11 3/4) and (21 3/4) AFE superlattice diffraction peaks, respectively. All samples showed intensive characteristic AFE superlattice peaks, meaning that the stabilized AFE *P* phase was maintained at room temperature (RT). In addition, Mn with different valence and radius can destroy the ordered polar nano-regions (PNRs) and favor the short-range non-polar domains.



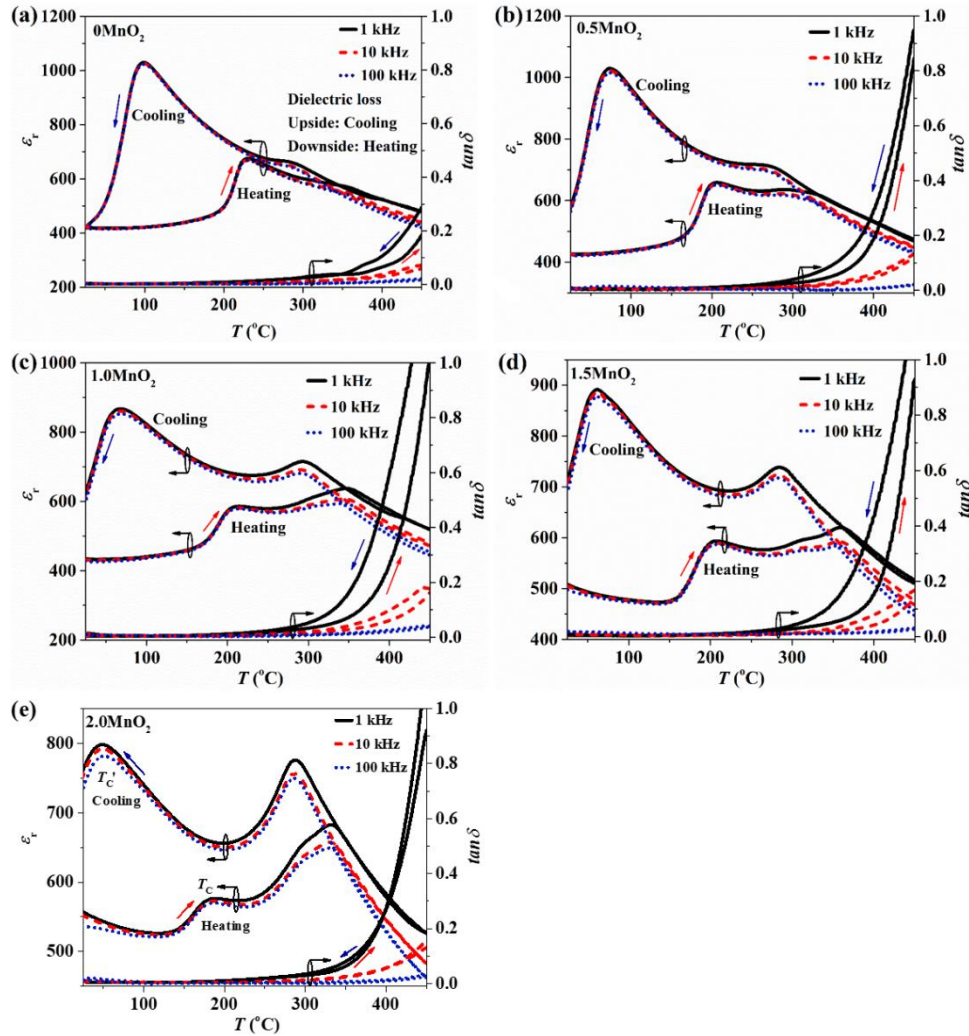


**Fig. 4-6** XRD patterns of  $\text{MnO}_2$ -doped ceramics for (a)  $10\text{-}60^\circ$ , (b)  $45\text{-}49^\circ$ , (c)  $(11\ 3/4)$  AFE superlattice diffraction, and (d)  $(21\ 3/4)$  AFE superlattice diffraction.

#### 4.2.3 Effect of $\text{MnO}_2$ dopant on dielectric and phase transition behavior

The dielectric constant ( $\varepsilon_r$ ) and loss ( $\tan\delta$ ) of  $\text{MnO}_2$ -doped ceramics as functions of temperature are demonstrated in Fig. 4-7. Obvious thermal hysteresis was observed in  $\varepsilon_r$  and  $\tan\delta$ , which is responsible for the first-order AFE phase transition in NN-based materials. The phase transition behaviors of heating and cooling processes were both closely related to  $\text{MnO}_2$  content, as shown in Fig. 4-7 and Table 4-1. Because  $\text{MnO}_2$  as an acceptor can greatly affect the dielectric properties when it diffused into crystal lattice. Firstly, the Curie temperature ( $T_C$ ) showed a slight reduction, while this phase transition temperature (defined as  $T_C'$ ) during cooling process decreased sharply with the addition of  $\text{MnO}_2$ . And the temperature difference ( $\Delta T_C$ ) between  $T_C$  and  $T_C'$  showed

an increase-decrease trend. Secondly, as  $\text{MnO}_2$  amount increased, the other peak above  $T_C$  became more apparent, which may be caused by the transition of different unit cell dimensions, involving the orthorhombic  $R$  and  $S$  phases. However, this anomaly has never been observed before, and it is also inconsistent with the XRD results. The mechanism needs a further study in the future. Consequently, a “hump-shape” curve emerged in the temperature range of 200-350 °C. Additionally, the RT dielectric constant ( $\epsilon_{\text{r(RT)}}$ ) increased gradually with the addition of  $\text{MnO}_2$ , while  $\tan\delta$  at RT was relatively low ( $< 0.7\%$ ), demonstrating improved dielectric properties. The lower sintering temperature can reduce oxygen vacancies at A-site by inhibiting volatilization, thereby affecting the dielectric properties.

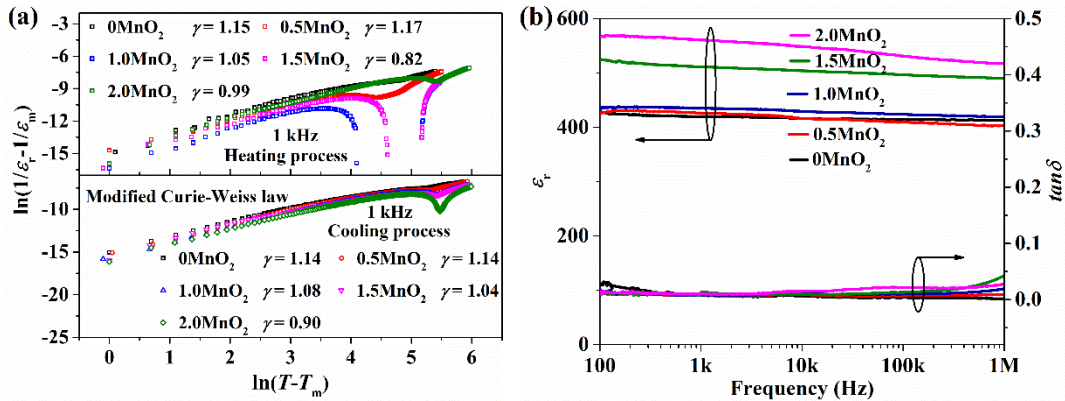


**Fig. 4-7** The  $\epsilon_{\text{r}}-T$  and  $\tan\delta-T$  curves of  $100y\text{MnO}_2$  ceramics for (a)  $0\text{MnO}_2$ , (b)  $0.5\text{MnO}_2$ , (c)  $1.0\text{MnO}_2$ , (d)  $1.5\text{MnO}_2$ , and (e)  $2.0\text{MnO}_2$ .

**Table 4-1.** Phase transition temperatures and RT dielectric properties at 1 kHz of 100yMnO<sub>2</sub> ceramics.

Sample	$T_C$	$T_C'$	$\Delta T_C$	$\varepsilon_{r(\text{RT})}$	$\tan\delta$ (%)
	(°C)	(°C)	(°C)	At 1 kHz, RT	
0MnO <sub>2</sub>	230	99	131	419	0.51
0.5MnO <sub>2</sub>	207	74	133	425	0.50
1.0MnO <sub>2</sub>	210	69	141	434	0.41
1.5MnO <sub>2</sub>	205	62	143	508	0.50
2.0MnO <sub>2</sub>	182	49	133	557	0.63

Importantly, all samples showed no relaxor-ferroelectric characteristics, both  $T_C$  and  $T_C'$  were independent on measured frequency. The modified Curie-Weiss law is applied to evidence that using  $\varepsilon_r$ - $T$  data at 1 kHz (Fig. 4-8(a)). The fitting diffuseness parameter ( $\gamma$ ) was around 1. It also reveals that all samples were deviated from relaxor behaviors ( $\gamma$  approaches 2). Moreover, Fig. 4-8(b) displays  $\varepsilon_r$  and  $\tan\delta$  as functions of frequency at RT, in the frequency range between 100 Hz and 1 MHz,  $\varepsilon_r$  slightly reduced, while  $\tan\delta$  exhibited relatively low values (< 3%).

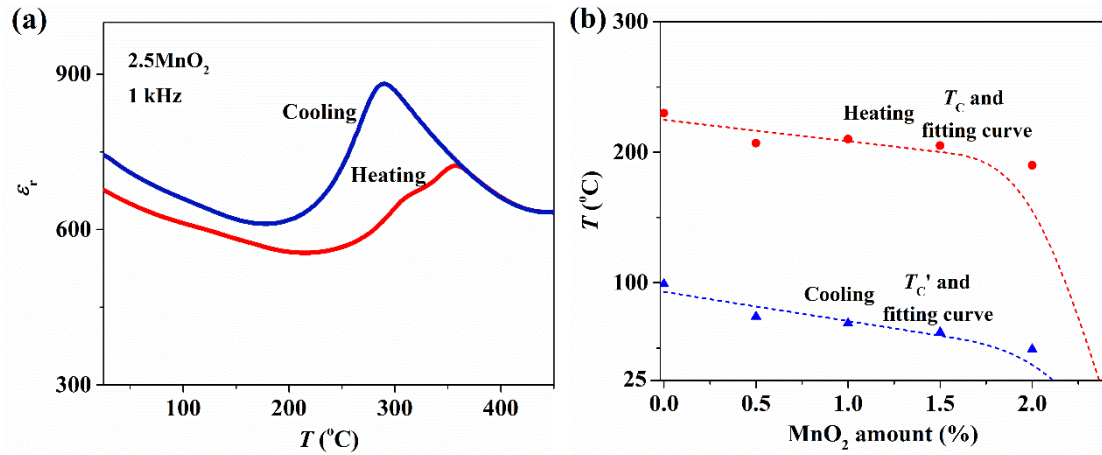


**Fig. 4-8** 100yMnO<sub>2</sub> ceramics for (a) Modified Curie-Weiss law at 1 kHz, (b)  $\varepsilon_r$  and  $\tan\delta$  depend on frequency at RT.

When MnO<sub>2</sub> was introduced, it can be found that the  $\varepsilon_{r(\text{RT})}$  increased obviously after the test process and it is defined as  $\varepsilon_{r(\text{RT})}'$  after the dielectric measurement. The difference ( $\Delta\varepsilon_{r(\text{RT})}$ ) between  $\varepsilon_{r(\text{RT})}$  and  $\varepsilon_{r(\text{RT})}'$  increased gradually with the increment in MnO<sub>2</sub> amount (Table 4-2). When 2.5% MnO<sub>2</sub> was applied,  $T_C$  suddenly decreased



below 25 °C, as plotted in Fig. 4-9(a). This reveals that an irreversible phase transition occurred at surrounding conditions, so it is essential to consider the MnO<sub>2</sub> adding limitation. The fitting results of  $T_C$  and  $T_C'$  depicted from  $\varepsilon_r$ - $T$  curves are demonstrated in Fig. 4-9(b), and considering the crystal stability, MnO<sub>2</sub> amount should be controlled to be 2.0%.



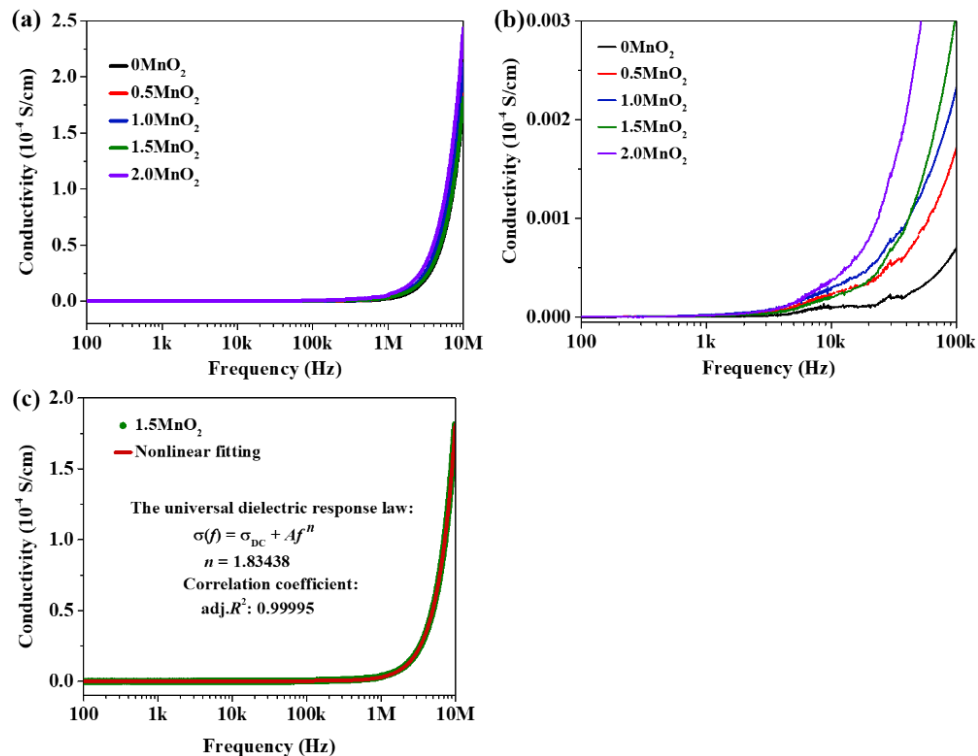
**Fig. 4-9** (a)  $\varepsilon_r$ - $T$  curves of 2.5MnO<sub>2</sub> ceramics measured at 1 kHz, (b) compositional dependent phase transition temperature depicted from  $\varepsilon_r$ - $T$  curves (points in figure) and the fitting results (dotted line).

**Table 4-2** RT dielectric constant and the difference measured at 1 kHz before and after dielectric measurements.

Sample	$\varepsilon_{r(RT)}$	$\varepsilon_{r(RT)}'$	$\Delta\varepsilon_{r(RT)}$
0MnO <sub>2</sub>	419	422	3
0.5MnO <sub>2</sub>	425	576	151
1.0MnO <sub>2</sub>	434	624	190
1.5MnO <sub>2</sub>	508	708	200
2.0MnO <sub>2</sub>	557	762	205
2.5MnO <sub>2</sub>	676	745	69

#### 4.2.4 Effect of MnO<sub>2</sub> dopant on energy storage properties

According to the universal dielectric response law described in Chapter 3, the influences of MnO<sub>2</sub> on conduction mechanism and conductivity ( $\sigma$ ) were investigated. The  $\sigma$  of 100yMnO<sub>2</sub> ceramics against frequency is displayed in Fig. 4-10. The  $\sigma$  of all samples grew slightly as increasing frequency within 10<sup>5</sup> Hz, and it was kept below 7×10<sup>-7</sup> S/cm (Table 4-3). As a whole, the  $\sigma$  values increased when MnO<sub>2</sub> was introduced (Fig. 4-10(b)). The vacancies can form composite defects induced by ion substitution, which in turn reduces the conduction activation energy. The nonlinear fitting of the universal dielectric response law of 1.5MnO<sub>2</sub> is displayed in the inset in Fig. 4-10(c). All samples demonstrated ideal results, as shown in Table 4-3, and the power exponents  $n$  are much larger than 1.0. It exhibits that the conduction mechanism presents as a localized hopping, demonstrating nano-ceramic characteristics.



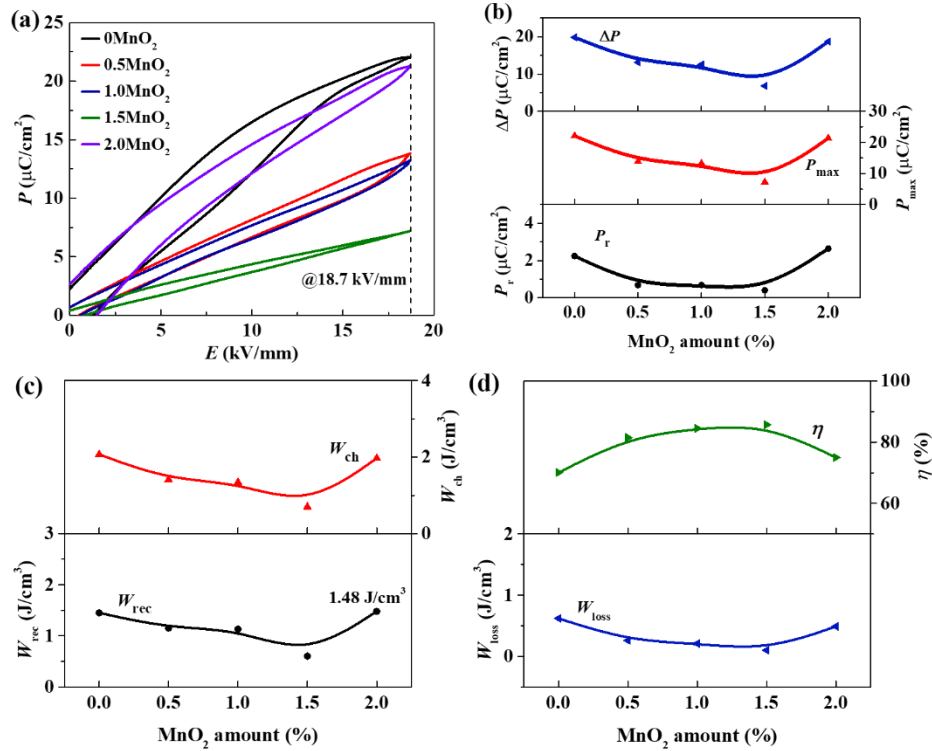
**Fig. 4-10** Room temperature conductivity of 100yMnO<sub>2</sub> ceramics depends on frequency for (a) 100 Hz-10 MHz, (b) 100 Hz-100 kHz.

**Table 4-3** The conductivity ( $\sigma$ ) at 100 Hz, 100 kHz, and fitting results of the universal dielectric response law at RT of 100yMnO<sub>2</sub> ceramics.

Sample	$\sigma$ (100 Hz) (10 <sup>-10</sup> S/cm)	$\sigma$ (100 kHz) (10 <sup>-7</sup> S/cm)	$n$	adj. $R^2$
0MnO <sub>2</sub>	0.40	0.99	1.88	0.99999
0.5MnO <sub>2</sub>	6.28	1.71	1.81	0.99997
1.0MnO <sub>2</sub>	3.41	2.66	1.80	0.99999
1.5MnO <sub>2</sub>	6.81	3.40	1.83	0.99995
2.0MnO <sub>2</sub>	3.03	6.98	1.71	0.99992

The RT energy storage performance detected at 18.7 kV/mm, 10 Hz is displayed in Fig. 4-11. It can be found that the introduction of MnO<sub>2</sub> was beneficial to reduce the width of hysteresis loops (WHL) resulted from the stabilized AFE phase. The addition of Mn leads to crystal distortion and charge variation, strengthening the disorder of microscopic domains. Both  $P_{\max}$ ,  $P_r$  and  $\Delta P$  ( $P_{\max} - P_r$ ) reduced greatly as increasing MnO<sub>2</sub> content when  $y \leq 1.5\%$  (Fig. 4-11 (b)). These can be inferred that the introduction of Mn with different valence and radius can destroy long-range ordered FE regions and favor the short-range non-polar regions.<sup>[17]</sup> Thus, the anti-ferroelectricity is enhanced with weak coupling from region to region, which is beneficial for energy storage.<sup>[18,19]</sup> Interestingly, these values for 2.0MnO<sub>2</sub> ceramics were strengthened suddenly, which has not been reported before. It may be caused by the larger  $\epsilon_r$  and unstable RT phase structure. In addition, oxygen vacancies can inhibit the reversal and movement of domains, while Mn would alter those to effect domain inversion under electric fields, improving polarization values.

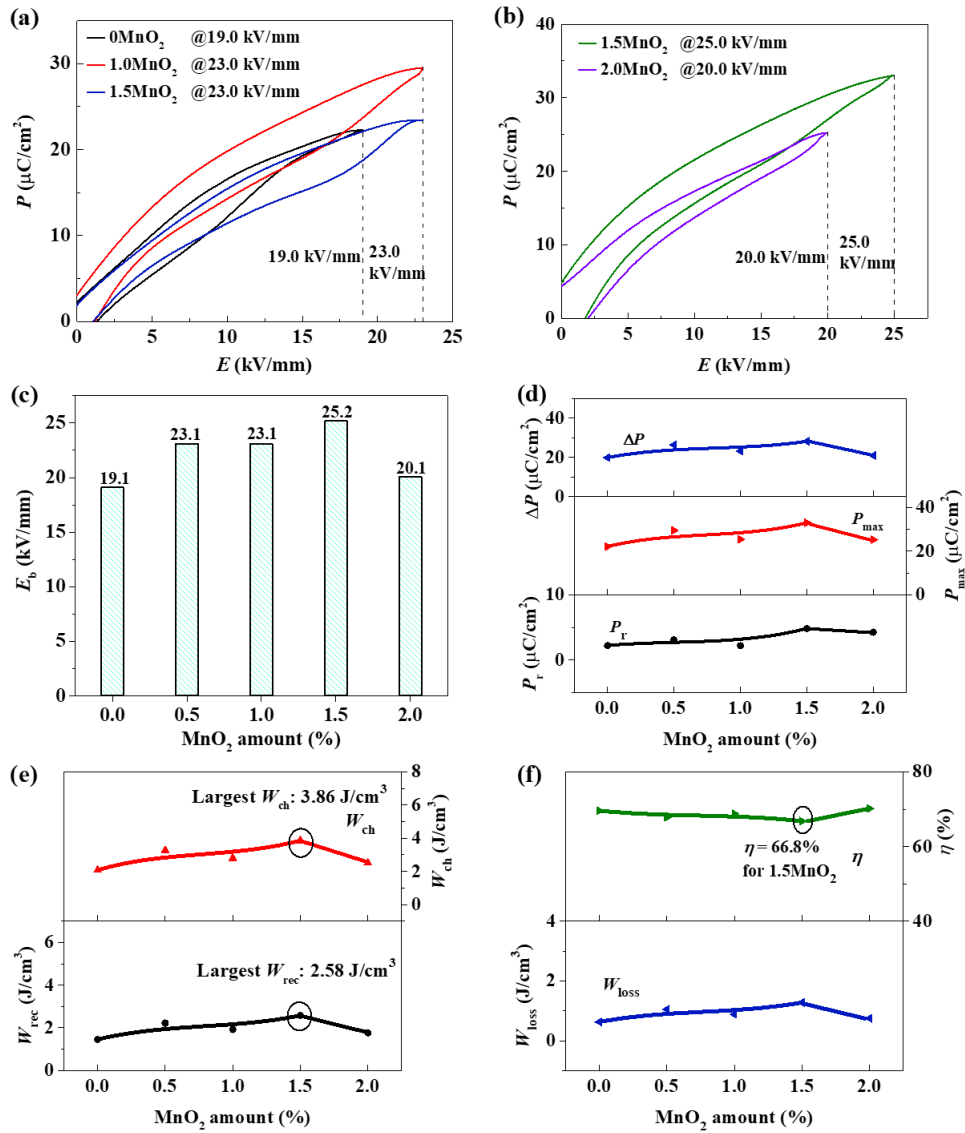
Consequently, the recoverable energy storage density ( $W_{\text{rec}}$ ) was reduced firstly, and then suddenly increased to the maximum value (1.48 J/cm<sup>3</sup>) for 2.0MnO<sub>2</sub> ceramics, as displayed in Fig. 4-11(c). Conversely, the energy storage efficiency ( $\eta$ ) advertised a contrary trend, the smallest and largest  $\eta$  were respectively observed for 0MnO<sub>2</sub> and 1.5MnO<sub>2</sub> ceramics (Fig. 4-11(d)). Alternatively, the change of charge energy density ( $W_{\text{ch}}$ ) and energy loss ( $W_{\text{loss}}$ ) was similar to  $W_{\text{rec}}$  when MnO<sub>2</sub> was adopted.



**Fig. 4-11** Energy storage performance of 100yMnO<sub>2</sub> ceramics under 18.7 kV/mm for (a)  $P$ - $E$  loops, (b) the  $P_{\max}$ ,  $P_r$  and  $\Delta P$  values, (c) the  $W_{\text{rec}}$  and  $W_{\text{ch}}$  values, and (d)  $W_{\text{loss}}$  and  $\eta$  values.

In order to obtain the maximum  $W_{\text{rec}}$ , all samples were measured at their optimum electric field, as displayed in Fig. 4-12. All  $P$ - $E$  loops displayed similar features with reduced WHL, which is mainly induced by the enhanced anti-ferroelectricity and weakened ferroelectricity (Figs. 4-12(a, c)). The  $E_b$  achieved the maximum value of 25.2 kV/mm when 1.5% MnO<sub>2</sub> was applied, while it decreased suddenly for 2.0MnO<sub>2</sub> ceramics, as shown in Fig. 4-12(c). Firstly, the suppressed volatilization of Na is beneficial for larger  $E_b$  induced by lower sintering temperatures. Secondly, the addition of Mn easily introduces defects, and large leakage conductance will lead to a lower  $E_b$ . Additionally, the grain size, uniformity, and densification also affect the voltage withstand performance. Mainly influenced by the anti-ferroelectricity and applied electric field, the  $P_r$ ,  $P_{\max}$  and  $\Delta P$  simultaneously achieved the biggest values for 1.5MnO<sub>2</sub>, as revealed in Fig. 4-12(d). However, the non-zero  $P_r$  was produced by a small amount of polar nano regions, which would be oriented under electric field. As a

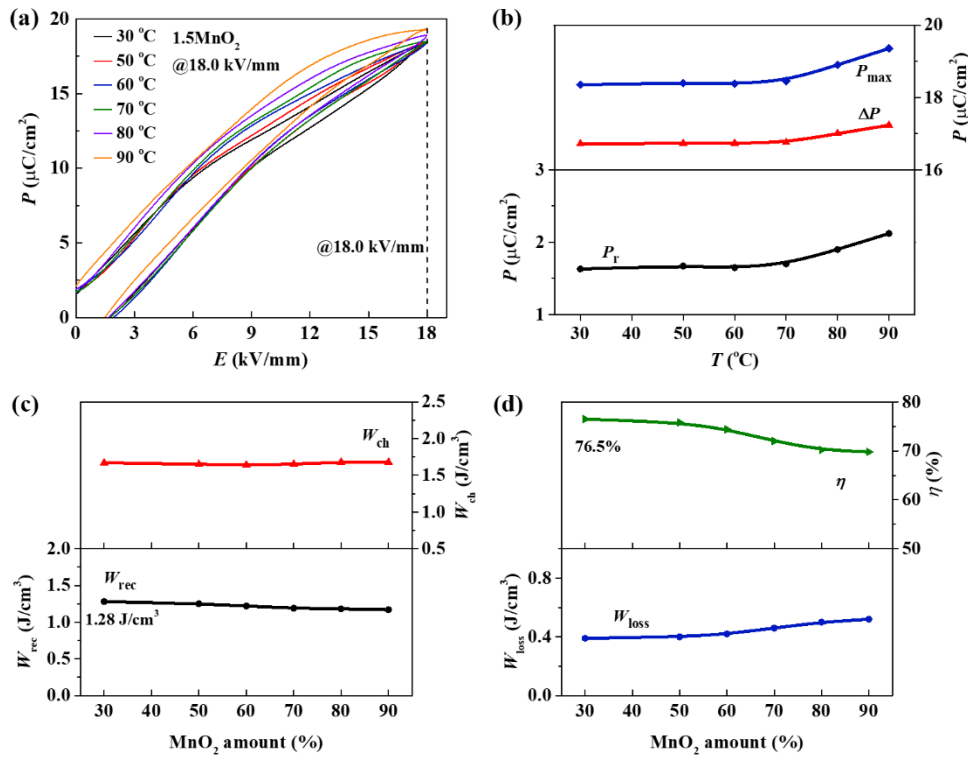
result, comprehensively affected by  $\Delta P$  and the applied electric field, the highest  $W_{\text{rec}}$  of  $2.58 \text{ J/cm}^3$  was obtained at a moderate electric field of  $25.0 \text{ kV/mm}$  for  $1.5\text{MnO}_2$  with  $\eta$  of  $66.8\%$  (Figs. 4-12(e, f)). The  $W_{\text{ch}}$  and  $W_{\text{loss}}$  were demonstrated similar change as  $W_{\text{rec}}$ .



**Fig. 4-12** The energy storage performance of  $100y\text{MnO}_2$  ceramics under the optimum electric field for (a, b)  $P$ - $E$  loops, (c) the  $E_b$  values, (d) the  $P_r$ ,  $P_{\text{max}}$  and  $\Delta P$  values, (e) the  $W_{\text{rec}}$  and  $W_{\text{ch}}$  values, and (f) the  $W_{\text{loss}}$  and  $\eta$  values.

The thermal influence on energy storage performance for  $1.5\text{MnO}_2$  was also investigated, as demonstrated in Fig. 4-13. Figure 4-13(a) represents the temperature-

dependent  $P$ - $E$  loops measured at 18.0 kV/mm and 10 Hz. The WHL was improved slightly as temperature increased, but no FE feature appeared in the temperature range of 30-90 °C. Both  $P_r$ ,  $P_{\max}$  and  $\Delta P$  maintained excellent thermal stability during 30-60 °C, and then showed a slight increase from 70 °C (Fig. 4-13(b)). As temperature increased, the domain inversion and movement became more active. Correspondingly, as shown in Figs. 4-13(c, d),  $W_{\text{rec}}$  reduced by 4.86% and  $\eta$  reduced by 2.75% from 30 °C to 60 °C. The addition of Mn effectively enhanced the thermal stability of energy storage. The optimum  $W_{\text{rec}}$  of 1.28 J/cm<sup>3</sup> with  $\eta$  of 76.5% was obtained at 30 °C, while  $\eta$  decreased gradually as temperature raised. In addition, the  $W_{\text{ch}}$  and  $W_{\text{loss}}$  also demonstrated good thermal stability.



**Fig. 4-13** Thermal effects on energy storage performance of 1.5MnO<sub>2</sub> for (a)  $P$ - $E$  loops, (b) the related polarization values, (c) the calculated  $W_{\text{rec}}$  and  $W_{\text{ch}}$  values, and (d) the calculated  $W_{\text{loss}}$  and  $\eta$ .

### 4.3 Summary

The pure perovskite 0.955NN-0.045LNM ceramics with MnO<sub>2</sub> as an additive were successfully prepared via the conventional solid-state method. The optimum sintering temperature is reduced from 1270 °C to 1210 °C with dense microstructure as a result of liquid phase sintering. The adoption of MnO<sub>2</sub> can also improve the anti-ferroelectricity, and obviously influence the phase transition behavior and thermal stability. However, the adding limitation (2%) should be noticed. Furthermore, the dielectric properties are also improved, coupled with a reduction in phase transition temperature. A  $W_{\text{rec}}$  of 2.58 J/cm<sup>3</sup> with  $\eta = 66.8\%$  is obtained for 1.5MnO<sub>2</sub> ceramics at 25.0 kV/mm, which is much stronger than most lead-free ceramics. These lead-free bulk ceramics also exhibit admirable thermal stability in energy storage performance. All presented results illustrate that this lead-free system is highly promising in electrostatic energy storage devices, but  $\eta$  should be improved further.

## References

- [1] T. Q. Shao, H. L. Du, H. Ma, S. B. Qu, J. Wang, J. F. Wang, X. Y. Wei and Z. Xu. *J. Mater. Chem. A*, **5**, 554, 2017.
- [2] F. Li, J. W. Zhai, B. Shen, X. Liu and H. R. Zeng. *Mater. Res. Lett.*, **6**, 345, 2018.
- [3] T. Wada, K. Tsuji, T. Saito and Y. Matsuo. *Jpn. J. Appl. Phys.*, **42**, 6110, 2003.
- [4] J. J. Bian, M. Otonicar, M. Spreitzer, D. Vengust and D. Suvorov. *J. Eur. Ceram. Soc.*, **39**, 2339, 2019.
- [5] J. F. Li, K. Wang, B. P. Zhang and L. M. Zhang. *J. Am. Ceram. Soc.*, **89**, 706, 2006.
- [6] Y. L. Su, X. M. Chen, Z. D. Yu, H. L. Lian, D. D. Zheng and J. H. Peng. *J. Mater. Sci.*, **52**, 2934, 2017.
- [7] P. Rutkowski, J. Huebner, A. Grabos, D. Kata, B. Sapinski and M. Faryna. *Materials*, **13**, 5741, 2020.
- [8] Y. F. Deng, J. J. Wang, C. X. Zhang, H. Ma, C. G. Bai, D. Q. Liu, F. M. Wu and B. Yang. *Crystals*, **10**, 705, 2020.
- [9] N. Wei, T. Karaki and T. Fujii. *Jpn. J. Appl. Phys.*, **59**, SPPD02, 2020.
- [10] J. Yoo, Y. W. Lee and J. Lee. *Ferroelectrics*, **572**, 51, 2021.
- [11] S. Yotthuan, S. Rueanngam, S. Pinitsoontorn, S. Chootin and T. Bongkarn. *Integr. Ferroelectr.*, **214**, 56, 2021.
- [12] B. Y. Qu, H. L. Du, Z. T. Yang, Q. H. Liu and T. H. Liu. *RSC Adv.*, **6**, 34381, 2016.
- [13] T. Teranishi, S. Azuma and A. Kishimoto. *Jpn. J. Appl. Phys.*, **58**, SLLC03, 2019.
- [14] L. L. Chen, H. X. Wang, P. Y. Zhao, Z. B. Shen, C. Q. Zhu, Z. Y. Cen, L. T. Li and X. H. Wang. *J. Am. Ceram. Soc.*, **102**, 2781, 2019.
- [15] Z. M. Cai, H. X. Wang, P. Y. Zhao, L. L. Chen, C. Q. Zhu, K. Z. Hui, L. T. Li and X. H. Wang. *Appl. Phys. Lett.*, **115**, 023901, 2019.
- [16] S. J. Yoon, A. Joshi and K. Uchino. *J. Am. Ceram. Soc.*, **80**, 1035, 1997.
- [17] M. X. Zhou, R. H. Liang, Z. Y. Zhou and X. L. Dong. *J. Mater. Chem. C*, **6**, 8528, 2018.
- [18] L. Zhao, Q. Liu, S. J. Zhang and J. F. Li. *J. Mater. Chem. C*, **4**, 8380, 2016.



[19] H. Ogihara, C. A. Randall and S. Trolrier-McKinstry. *J. Am. Ceram. Soc.*, **92**, 110, 2009.

## Chapter 5

### Preparation of $\text{NaNbO}_3\text{-La}(\text{Nb}_{1/3}\text{Mg}_{2/3})\text{O}_3\text{-CaZrO}_3$ Ceramics

#### 5.1 Introduction

Except for recoverable energy storage density ( $W_{\text{rec}}$ ), the efficiency ( $\eta$ ) should also be emphasized for energy storage applications. A lower  $\eta$  not only implies a waste of electricity, but also means more electricity is converted to heat during the application process.<sup>[1]</sup> Thus, it will result in a reduction in energy storage performance and even break down the capacitors.<sup>[1]</sup> Nevertheless, anti-ferroelectric (AFE)-liked  $\text{NaNbO}_3$  (NN)-based ceramics usually occupy a lower  $\eta$  due to the competitive relationship between AFE and metastable ferroelectric (FE) phase. For example, rare-earth elements doped  $0.96\text{NaNbO}_3\text{-}0.04\text{CaSnO}_3$  ceramics only possessed a reduced  $\eta$  of 62.0%.<sup>[2]</sup> Therefore, some endeavors have been focused on para-electric (PE) NN-based ceramics, which usually possess a lower residual polarization ( $P_r$ ) and a higher  $\eta$  ( $> 80\%$ ).<sup>[3,4]</sup> However, there exists a new issue that a suppressed maximum polarization ( $P_{\text{max}}$ ) is commonly observed in NN-based PE ceramics. Thereby, energy storage performance can only be improved by increasing applied electric field, leading to high security risks and large cost of insulation technology.<sup>[3-5]</sup> Nevertheless, only few study has been focused on simultaneously improving  $W_{\text{rec}}$  and  $\eta$  in AFE-liked NN-based ceramics under a low electric field.

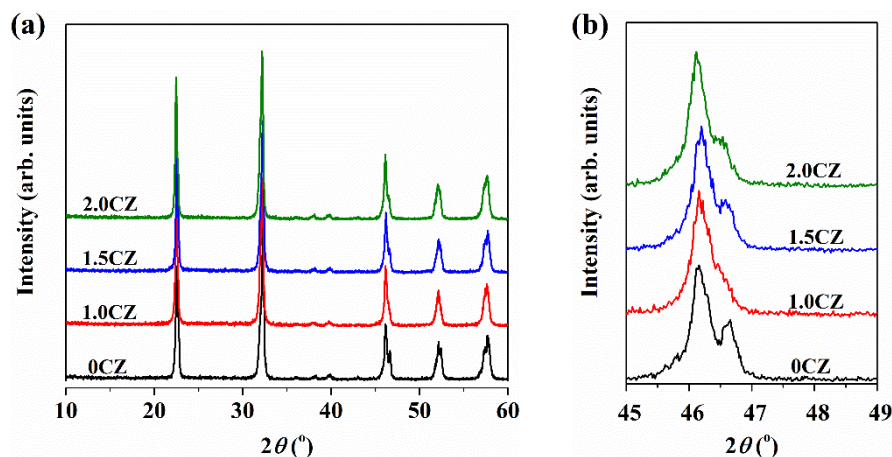
Therefore,  $\text{CaZrO}_3$  (CZ) ceramics were selected to reduce the width of hysteresis loops (WHL) and enhance room temperature (RT)  $W_{\text{rec}}$  and  $\eta$  under lower external electric fields in NN-based AFE systems. Ternary  $\text{NaNbO}_3\text{-La}(\text{Nb}_{1/3}\text{Mg}_{2/3})\text{O}_3\text{-CaZrO}_3$  (NN-LNM-CZ) ceramics were fabricated in this chapter. The effects of CZ on phase transition behavior, electrical properties, and energy storage performance were subsequently studied.

## 5.2 Performance of Ternary NN-LNM-CZ Ceramics

CZ was applied in  $(0.955-z)\text{NN}-0.045\text{LNM}-z\text{CZ}$  ceramics, using the solid-state method as described in section 2.1.2, which are abbreviated as  $100z\text{CZ}$  hereafter. The calcination was carried out at 950-1000 °C, while the green bodies were sintered at 1220-1290 °C.

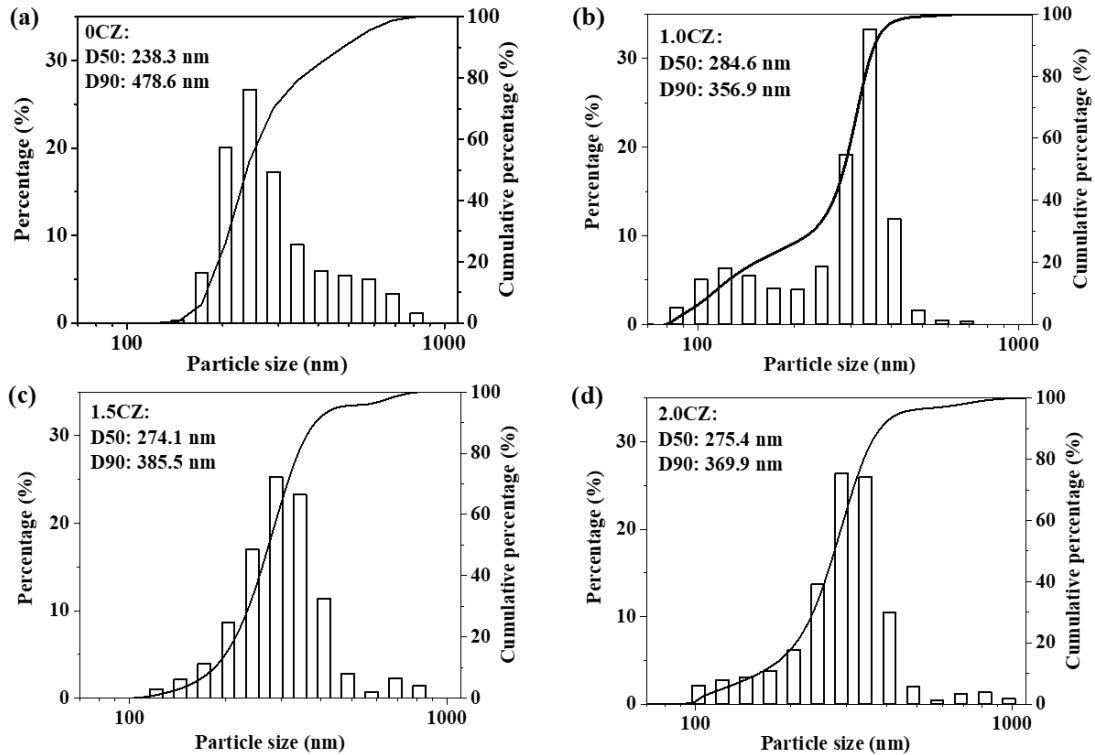
### 5.2.1 Sintering performance of NN-LNM-CZ ceramics

After calcination, the fine powders were detected by X-ray diffraction (XRD), as displayed in Fig. 5-1. Characteristic perovskite peaks were observed with weak diffraction intensity, revealing a preliminary reaction that can provide enough driving force for next sintering process. It demonstrates that the additives successfully diffused into crystal lattice under much lower calcination temperatures. All these evidences certify that the calcination process is appropriate for  $100z\text{CZ}$  ceramics and beneficial for sintering process.



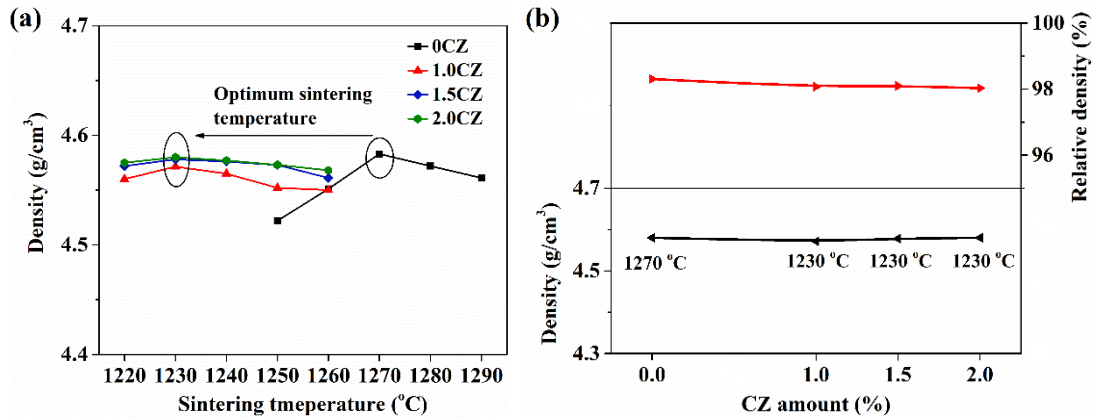
**Fig. 5-1** XRD patterns of  $100z\text{CZ}$  pre-products for (a) 10-60°, (b) 45-49°.

Figure 5-2 displays the D50 and D90 values of  $100z\text{CZ}$  pre-products after crushing. Although D50 enlarged slightly with CZ content increased, D90 sharply reduced to below 400 nm. Generally, smaller particles (D90) possess more reactive activity beneficial to reducing sintering temperature. It shows a potential to save energy for industrial applications.



**Fig. 5-2** The particle size distribution of 100zCZ pre-products after crushing for (a) 0CZ, (b) 1.0CZ, (c) 1.5CZ, (d) 2.0CZ.

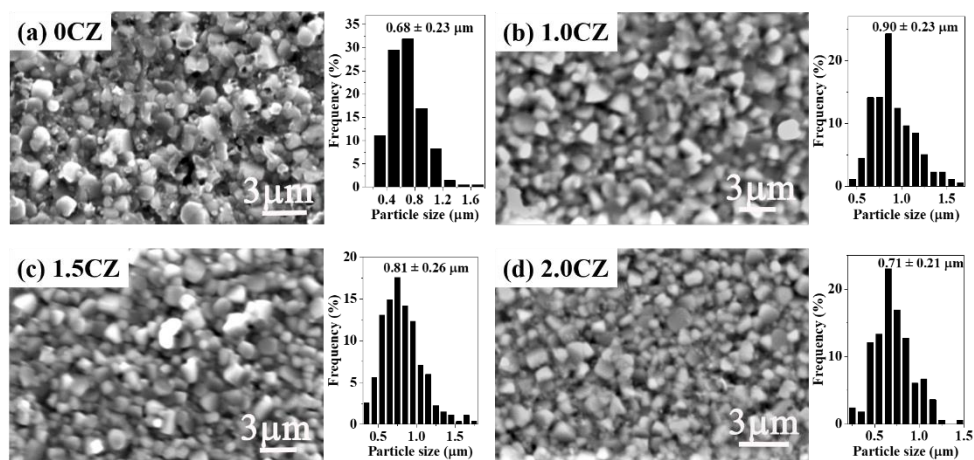
Figure 5-3 displays the density and relative density values of 100zCZ ceramics, it can be found that the range of temperature window of full densification was obviously widened by adding CZ. The optimum sintering temperature reduced from 1270 °C to 1230 °C with the introduction of CZ. This may be resulted from the smaller particles of the pre-products. In addition, the substitution of ions with different radius and charge will create more defect to improve reaction driving force. Although slight reductions in density and relative density were observed in Fig. 5-3(b), a large relative density (> 98.0%) was maintained.



**Fig. 5-3** 100zCZ-doped ceramics for (a) density *versus* sintering temperature, (b) density and relative density of ceramics sintered at the optimum temperature.

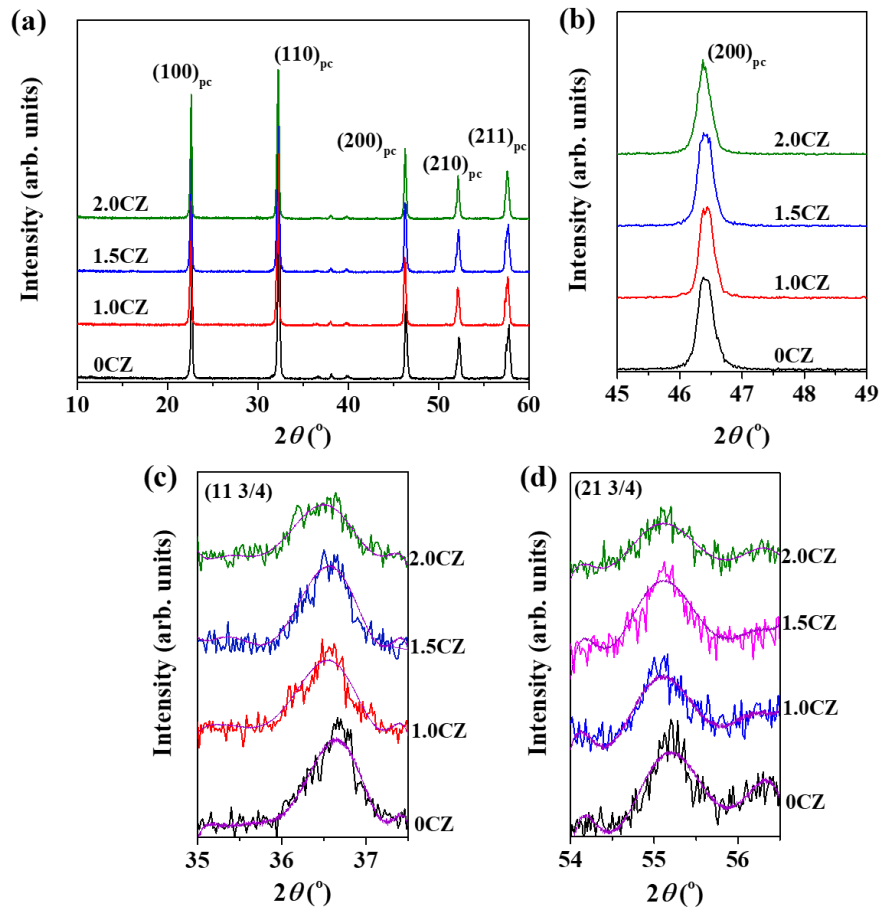
### 5.2.2 Phase structure and microstructure of NN-LNM-CZ ceramics

In Fig. 5-4, the microstructure and average grain size distribution of 100zCZ ceramics are displayed. All the ceramics possessed a dense and uniform microstructure with only few poles positioned on the grain boundaries. The reduced sintering temperature trends to inhibit grain growth, while CZ shows opposite effects with higher driving force. Therefore, the average grain size showed an increase-decrease change, but all samples possessed relatively small grains (< 1.0 μm). Generally speaking, these are small enough to enhance  $E_b$  for NN-based bulk ceramics.



**Fig. 5-4** Microstructure and particle size distribution of 100zCZ ceramics for (a) 0CZ, (b) 1.0CZ, (c) 1.5CZ, (d) 2.0CZ.

Figure 5-5 plots XRD patterns of the well-sintered  $100z\text{CZ}$  ceramics. It can be observed that all samples possessed single perovskite structure without any appreciable secondary impurity phases, implying that CZ successfully diffused into the crystal lattice to form solid solutions (Fig. 5-5(a)). With the increase of element types, the ion coordination becomes more complex, which is conducive to solid solution. The magnified sections of  $(200)_{\text{pc}}$  reflection peaks showed unimodal shape, and the peak of 2.0CZ was more incisive than that of others (Fig. 5-5(b)). This should be explained that the phase structure was gradually transformed from orthorhombic  $P$  phase to orthorhombic  $R$  phase with CZ content increased. In Figs. 5-5(c, d), a close analysis of XRD spectra around  $2\theta$  angles  $36.5^\circ$  and  $55.2^\circ$  is demonstrated, which corresponds to the  $(11\ 3/4)$  and  $(21\ 3/4)$  AFE superlattice diffraction, respectively. The samples demonstrated strengthened characteristic AFE superlattice peaks when  $z \leq 1.5\%$ , meaning that the stabilized AFE phase was maintained mainly caused by the decrease in tolerance factor  $t$  (Table 5-1). The reduction in tolerance factor will alter the free energy configuration to improve anti-ferroelectricity in NN-based materials. However, those peaks were slightly weakened for 2.0CZ samples, which may be caused by the appearance of  $R$  phase and unstable phase structure at RT, and it will be analyzed later.



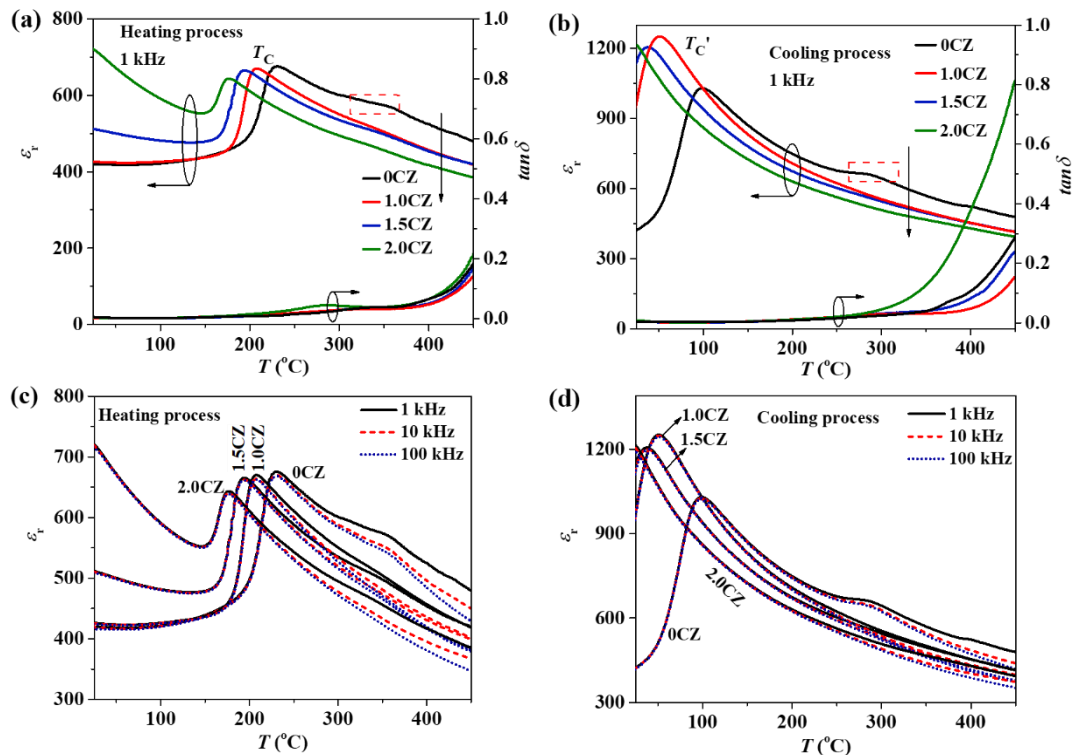
**Fig. 5-5** XRD patterns of 100zCZ ceramics for (a) 10-60°, (b) 45-49°, (c) (11 3/4) AFE superlattice diffraction, and (d) (21 3/4) AFE superlattice diffraction.

### 5.2.3 Dielectric and phase transition behavior of NN-LNM-CZ ceramics

Figure 5-6(a) represents the dielectric properties of 100zCZ ceramics as functions of temperature during heating process, while Fig. 5-6(b) displays the dielectric performance during cooling procedure. Evident peaks in dielectric constant ( $\epsilon_r$ )- $T$  curves were observed located at Curie temperature ( $T_C$ ). The observed dielectric characteristics were absolutely different from those of piezoelectric and relaxor-ferroelectric ceramics, which manifested as obvious thermal hysteresis in both  $\epsilon_r$  and  $\tan\delta$ . It is originated from the first-order AFE phase transition of NN ceramics. In non-doped samples, the other anomaly was detected above  $T_C$  (230 °C) during both heating and cooling processes (the red boxes in Figs. 5-6(a, b)). Nonetheless, as CZ was introduced, this anomaly absolutely disappeared. This may be due to the interaction of

macro- and micro-domains. Moreover, during the cooling process, the dielectric vertex temperature (defined as  $T_C'$ ) and  $T_C$  both decreased obviously as CZ content increased. That leads to an enlargement in temperature difference ( $\Delta T_C$ ) between  $T_C$  and  $T_C'$ , as shown in Fig. 5-6 and Table 5-1. These can be interpreted that CZ is beneficial for the stabilized AFE phase.

The RT  $\epsilon_r$  ( $\epsilon_{r(RT)}$ ) grew apparently with the increment in CZ amount, while RT  $\tan\delta$  occupied relatively low values ( $< 0.6\%$ ), especially for 1.0CZ and 1.5CZ ceramics, as shown in Table 5-1. This will be beneficial for improved polarization values and breakdown electric field strength. Differently,  $\epsilon_r$  at  $T_C$  exhibited a slight reduction as increasing CZ content, while that at  $T_C'$  displayed an increase-decrease trend and achieved the maximum value for 1.0CZ. In addition, the influences of frequency on dielectric performance are plotted in Figs. 5-6(c, d). Both  $T_C$  and  $T_C'$  were independent on frequency, which means no relaxor characteristics are observed for 100zCZ ceramics.



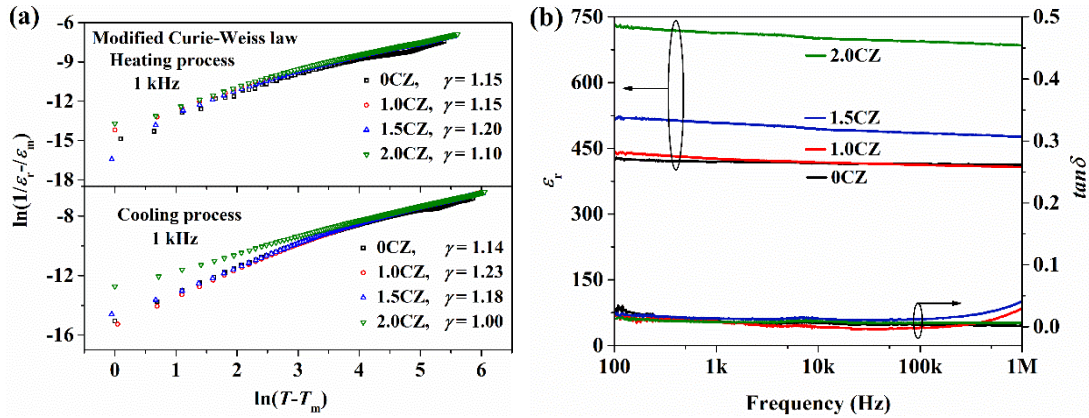
**Fig. 5-6** Dielectric properties of 100zCZ ceramics for (a) heating process at 1 kHz, (b) cooling process at 1 kHz, (c) frequency dependent  $\epsilon_r$ - $T$  curves during heating process, and (d) frequency dependent  $\epsilon_r$ - $T$  curves during cooling process.



**Table 5-1** Phase transition temperatures and RT dielectric properties at 1 kHz of 100zCZ ceramics.

Sample	$T_C$ (°C)	$T_C'$ (°C)	$\Delta T_C$ (°C)	$\varepsilon_{r(RT)}$ AT RT, 1 kHz	$\tan\delta$ (%)	$t$
0CZ	230	99	131	419	0.50	0.96551
1.0CZ	208	51	157	426	0.13	0.96550
1.5CZ	196	38	158	511	0.08	0.96471
2.0CZ	177	< 25	non	720	0.38	0.96444

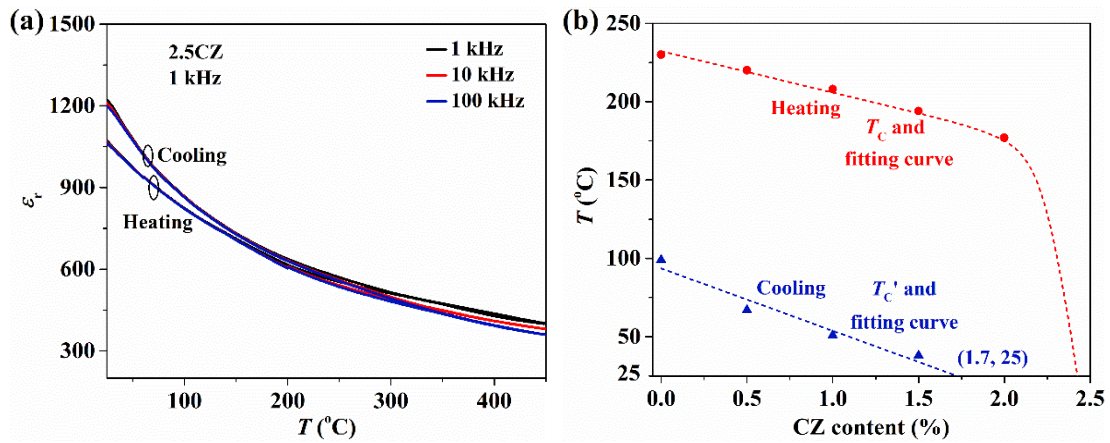
To support above analysis, the modified Curie-Weiss law is exploited in Fig. 5-7(a), in which the data were extracted from  $\varepsilon_r$ - $T$  curves measured at 1 kHz. When the diffuseness parameter ( $\gamma$ ) is close to 1, the sample deviates from relaxor behavior. Therefore, the smaller  $\gamma$  values (< 1.25) also indicate that no relaxor-ferroelectric phase was induced for all samples. Furthermore, Fig. 5-7(b) plots  $\varepsilon_r$  and  $\tan\delta$  as functions of frequency, the  $\varepsilon_r$  gradually reduced (< 9.0%) as increasing frequency, while the  $\tan\delta$  featured relatively low values (< 3%), illustrating attractive frequency stability.



**Fig. 5-7** 100zCZ ceramics for (a) Modified Curie-Weiss law at 1 kHz, (b) frequency-dependent  $\varepsilon_r$  and  $\tan\delta$  at RT.

Noticeably, as shown in Fig. 5-6,  $\varepsilon_{r(RT)}$  was dependent on the thermal effect for CZ-doped ceramics. After the dielectric measure process, the RT dielectric constant (defined as  $\varepsilon_{r(RT)'}^{\prime}$ ) was obviously enlarged. When  $T_C' > 25$  °C, the difference ( $\Delta\varepsilon_{r(RT)} = \varepsilon_{r(RT)} - \varepsilon_{r(RT)'}^{\prime}$ ) also grew apparently with the increase in CZ content, as displayed in

Table 4-2. Furtherly,  $\varepsilon_r$ - $T$  curves of 2.0CZ displayed unique features, accompanied with  $T_C' < 25$  °C. It implies that the thermal-induced phase transition becomes an irreversible process. As presented in Fig. 5-8(a),  $T_C$  suddenly dropped below 25 °C when CZ amount increased to 2.5%. It can be inferred that a new crystal structure is constructed at surrounding conditions when CZ exceeds an adding limitation. Therefore, Fig. 5-8(b) demonstrates the fitting curves of  $T_C$  and  $T_C'$  to describe this limit. As seen, the  $T_C'$  will be reduced to 25 °C when 1.7% CZ is applied. Considering the stability of crystal structure, the amount of CZ should be controlled to be 1.7%.



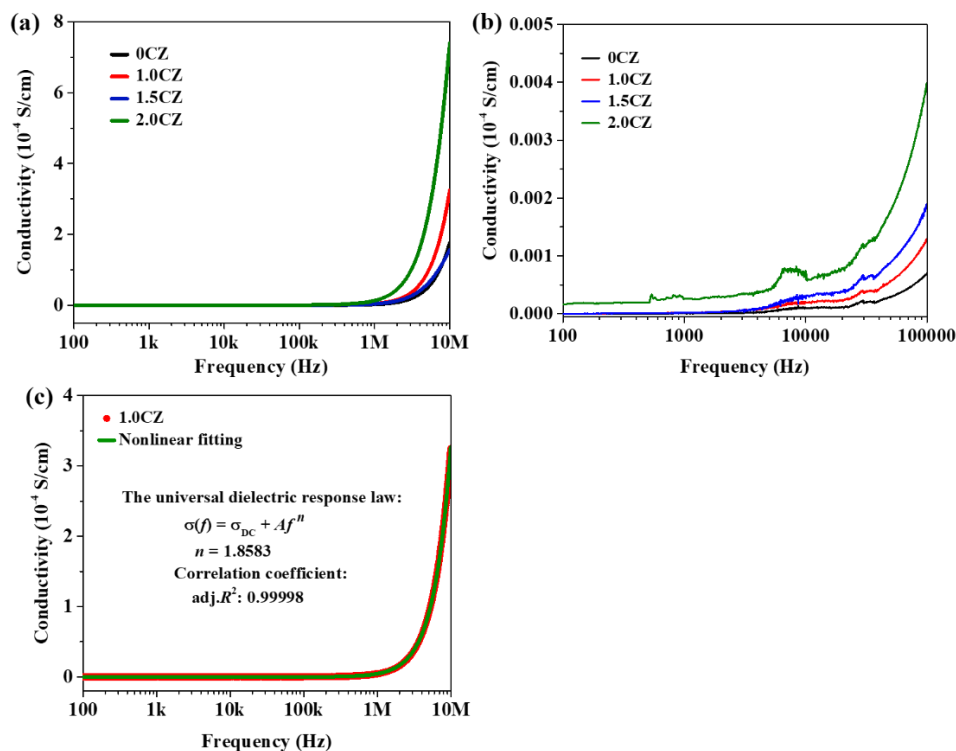
**Fig. 5-8** (a)  $\varepsilon_r$ - $T$  curves of 2.5CZ ceramics (b) compositional dependent phase transition temperature depicted from  $\varepsilon_r$ - $T$  curves (points in figure) and the fitting results (dotted line).

**Table 5-2** RT dielectric constant and the difference measured at 1 kHz before and after dielectric measurements.

Sample	$\varepsilon_{r(RT)}$	$\varepsilon_{r(RT)'}^*$	$\Delta\varepsilon_{r(RT)}$
0CZ	419	422	3
1.0CZ	426	970	544
1.5CZ	511	1140	629
2.0CZ	720	1215	495
2.5CZ	1071	1222	151

### 5.2.4 Energy storage performance of NN-LNM-CZ ceramics

Effects of CZ amount on conduction mechanism and conductivity ( $\sigma$ ) were studied, the  $\sigma$  values against frequency is presented in Fig. 5-9. The  $\sigma$  grew slightly as increasing frequency up to  $10^5$  Hz, and then it increased rapidly (Fig. 5-10(a)). The conductivity increased greatly in the whole frequency range when CZ was employed, especially for 2.0CZ ceramics (Figs. 5-9(a, b) and Table 5-3). It is presumably originated from the oxygen octahedral tilts of the unit cell. In addition, the interaction between composite defects can reduce the conductance activation energy, increasing the conductivity. A nonlinear fitting of the universal dielectric response law was applied to investigate the conduction mechanism, and the fitting result of 1.0CZ is revealed in Fig. 5-9(c). As displayed in Table 5-3, all samples presented ideal fitting models. The power exponents  $n$  are much larger than 1.0 for all samples, meaning the conduction and carrier motivation mechanism keeps unchanged. It exhibits a localized hopping conduction mechanism with a small hop in the specific area.



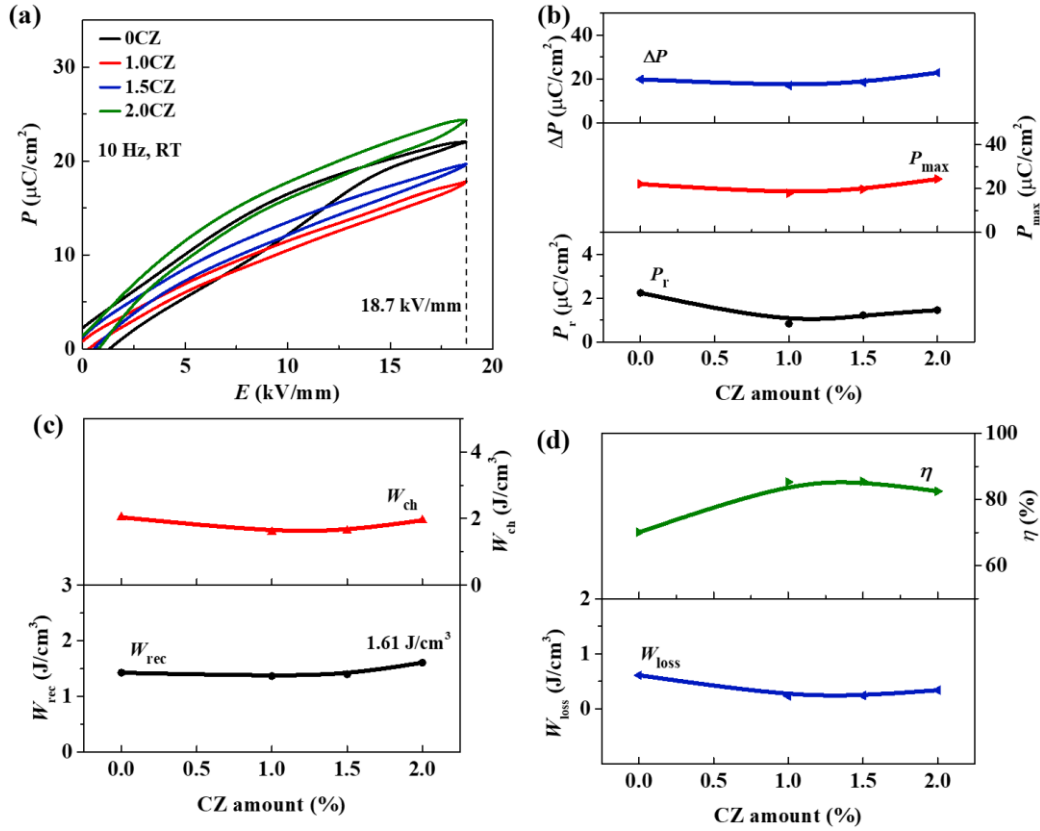
**Fig. 5-9** Room temperature conductivity of 100zCZ ceramics depends on frequency for (a) 100 Hz-10 MHz, (b) 100 Hz-100 kHz.

**Table 5-3** The RT conductivity ( $\sigma$ ) at 100 Hz, 100 kHz, and fitting results of the universal dielectric response law of 100zCZ ceramics.

Sample	$\sigma$ (100 Hz) ( $10^{-10}$ S/cm)	$\sigma$ (100 kHz) ( $10^{-7}$ S/cm)	$n$	adj. $R^2$
0CZ	0.40	0.99	1.88	0.99999
1.0CZ	2.75	1.70	1.86	0.99998
1.5CZ	1.95	1.95	1.48	0.99930
2.0CZ	169	4.79	1.65	0.99965

The room temperature energy storage performance of 100zCZ ceramics were measured at 18.7 kV/mm and 10 Hz, as displayed in Fig. 5-10. Figure 5-10(a) reveals that all  $P$ - $E$  loops are different from typical well-saturated FE behavior (large  $P_r$ ), demonstrating a coexistence of FE and AFE phase. The addition of CZ can break the long-range ordered regions and adjust the free energy to favour anti-ferroelectricity. Significantly, the reduced  $P_r$  and narrowed width of hysteresis loops (WHL) are beneficial for improved energy storage performance. The  $P$ - $E$  loops were narrowed obviously with the addition of CZ. The AFE-liked  $P$ - $E$  loops with suppressed  $P_r$  is caused by the competition between AFE and FE domains, including transition between macro-domains and micro-domains and interaction of popar and non-polar microdomains.

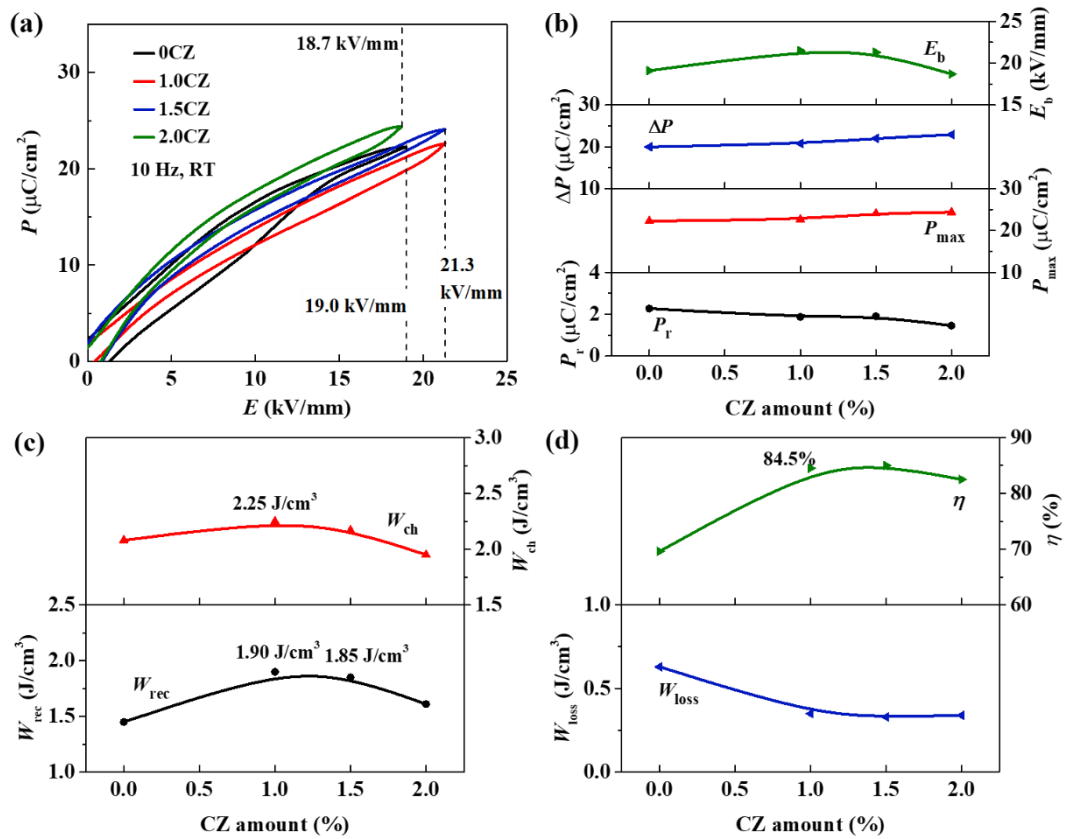
The polarization values, both  $P_r$ ,  $P_{\max}$  and  $\Delta P$  ( $P_{\max} - P_r$ ) varied slightly with the addition of CZ, achieving the largest values in  $P_{\max}$  and  $\Delta P$  for 2.0CZ (Fig. 5-10(b)). The variation of  $P_{\max}$  was more obvious than that of  $P_r$ , indicating that partially FE ordered regions can spontaneously transform into ordered AFE structure. As shown in Fig. 5-10(c),  $W_{\text{rec}}$  reached the maximum value ( $1.61 \text{ J/cm}^3$ ) for 2.0CZ, because  $W_{\text{rec}}$  was mainly related to  $\Delta P$  under the identical electric field. Profiting from the reduced WHL, all CZ-doped ceramics obtained superior  $\eta$  ( $> 80.0\%$ ) much higher than 0CZ ceramics (Fig. 5-10(d)). Also, the energy loss ( $W_{\text{loss}}$ ) decreased gradually with the addition of CZ, while the charge energy density ( $W_{\text{ch}}$ ) varied slightly.



**Fig. 5-10** Energy storage properties of 100zCZ ceramics at 18.7 kV/mm for (a)  $P$ - $E$  loops, (b) the  $P_r$ ,  $P_{max}$  and  $\Delta P$  values, (c) the  $W_{rec}$  and  $W_{ch}$   $\eta$  values, and (d) the  $W_{loss}$  and  $\eta$  values.

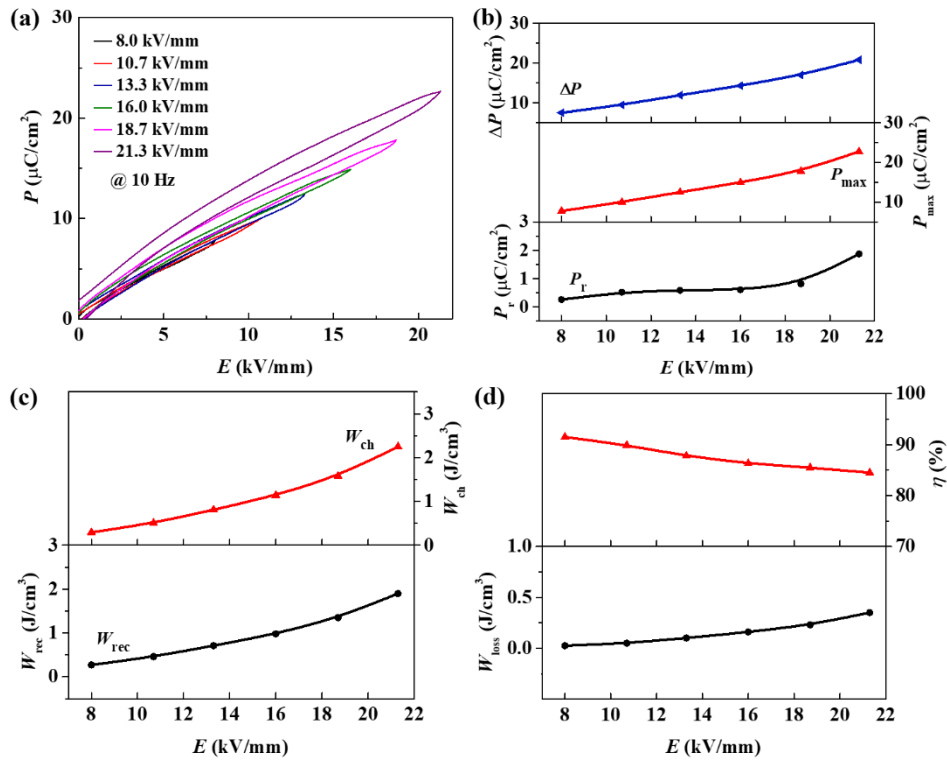
To detect the largest  $W_{rec}$ , the energy storage performance was measured under their respective optimum electric field, and the results are demonstrated in Fig. 5-11. All samples possessed reduced  $P_r$  and thin WHL, as displayed in Fig. 5-11(a), demonstrating AFE-like  $P$ - $E$  loops. The  $E_b$  increased gradually as CZ was employed when  $x \leq 1.5\%$ , while that of 2.0CZ reduced abruptly, as presented in Fig. 5-11(b). This may be caused by the unstable phase structure and larger conductivity at RT of 2.0CZ ceramics. Both  $P_{max}$  and  $\Delta P$  increased gradually with the increase in CZ amount, while  $P_r$  reduced overall. The enhanced anti-ferroelectricity and weakened ferroelectricity should be responsible for that. In addition, by reducing the sintering temperature and sodium content, CZ can affect the vacancy concentration. Reduced oxygen vacancy contributes to domain inversion under electric field, altering  $P_{max}$ . However, a small amount of polar nano regions (PNRs) leads to a near-zero  $P_r$ .

As displayed in Figs. 5-11 (c, d), take applied electric field into account,  $W_{\text{rec}}$  reached the optimum value of  $1.90 \text{ J/cm}^3$  with  $\eta = 84.5\%$  for 1.0CZ ceramics under  $21.3 \text{ kV/mm}$ . The energy storage properties for 1.5CZ ceramics were also attractive with  $W_{\text{rec}} = 1.85 \text{ J/cm}^3$ . However,  $W_{\text{rec}}$  for 2.0CZ showed a sharp reduction, which is probably caused by the unstable phase structure. It also keeps in line with above discussions. Significantly, all CZ-doped ceramics possessed large  $\eta$  values above 80%, which could compare with RFE and PE ceramics. As well known, a large  $\eta$  can not only improve  $W_{\text{rec}}$  but also inhibit breakdown process, which is essential for applications. The improved  $W_{\text{ch}}$  was also observed for 1.0CZ and 1.5CZ ceramics, while  $W_{\text{loss}}$  gradually decreased.



**Fig. 5-11** Energy storage performance of 100zCZ ceramics under the optimal electric field for (a)  $P$ - $E$  loops, (b) the  $P_r$ ,  $P_{\text{max}}$ ,  $\Delta P$ , and  $E_b$  values, (c) the  $W_{\text{rec}}$  and  $W_{\text{ch}}$  values, (d) the  $W_{\text{loss}}$  and  $\eta$  values.

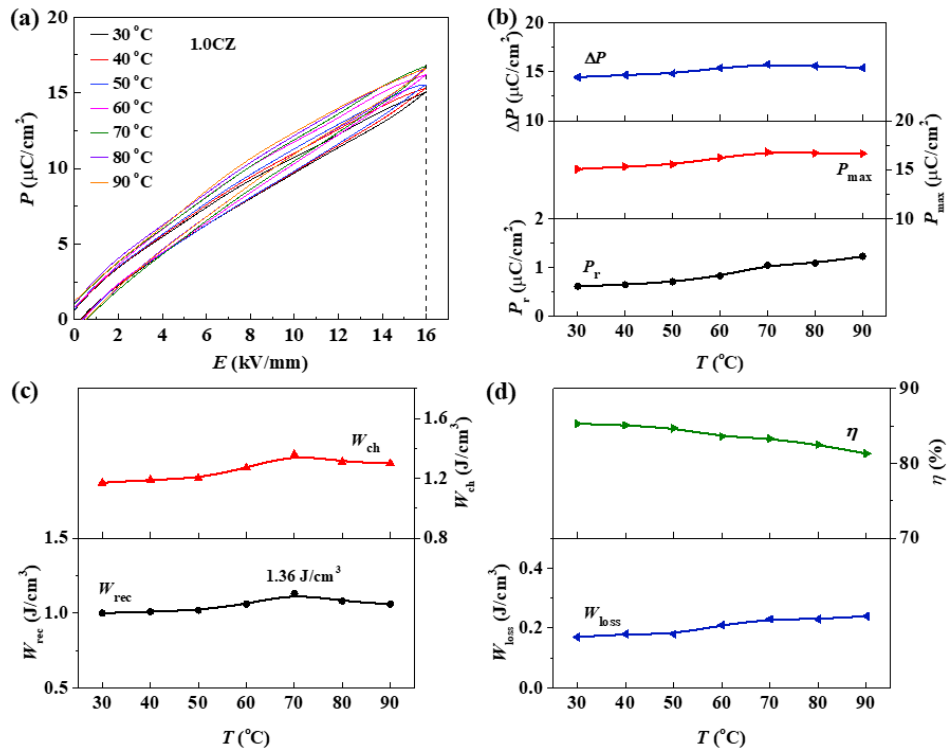
Figure 5-12 demonstrates the energy storage performance of 1.0CZ as a function of applied electric field. Although the  $P$ - $E$  loops were slightly broadened as electric field increased, the well-narrowed shape was maintained (Fig. 5-12(a)). Both  $P_{\max}$  and  $\Delta P$  increased linearly when external electric field rised, while  $P_r$  enlarged just a little, as shown in Fig. 5-12(b). As the electric field increased from 8.0 kV/mm to 21.3 kV/mm,  $P_r$  increased from 0.29  $\mu\text{C}/\text{cm}^2$  to 1.87  $\mu\text{C}/\text{cm}^2$  and  $P_{\max}$  increased from 7.74  $\mu\text{C}/\text{cm}^2$  to 22.3  $\mu\text{C}/\text{cm}^2$ . Hence,  $W_{\text{rec}}$  and  $W_{\text{ch}}$  increased obviously as increasing electric field, as shown in Fig. 5-12(c). Alternatively,  $W_{\text{loss}}$  grew slightly with the increase in electric field, while  $\eta$  reduced sharply (Fig. 5-12 (d)). However,  $\eta$  maintained a relatively high value of 84.5% even if the largest electric field (21.3 kV/mm) was applied.



**Fig. 5-12** Energy storage performance of 1.0CZ as a function of applied electric field for (a)  $P$ - $E$  loops, (b) the  $P_r$ ,  $P_{\max}$ ,  $\Delta P$  values, and (c) the  $W_{\text{rec}}$  and  $W_{\text{ch}}$  values, and (d)  $W_{\text{loss}}$  and  $\eta$  values.

The temperature-dependent energy storage properties of 1.0CZ were measured at 16.0 kV/mm, as plotted in Fig. 5-13. In the temperature range of 30-90  $^{\circ}\text{C}$ , all  $P$ - $E$  loops

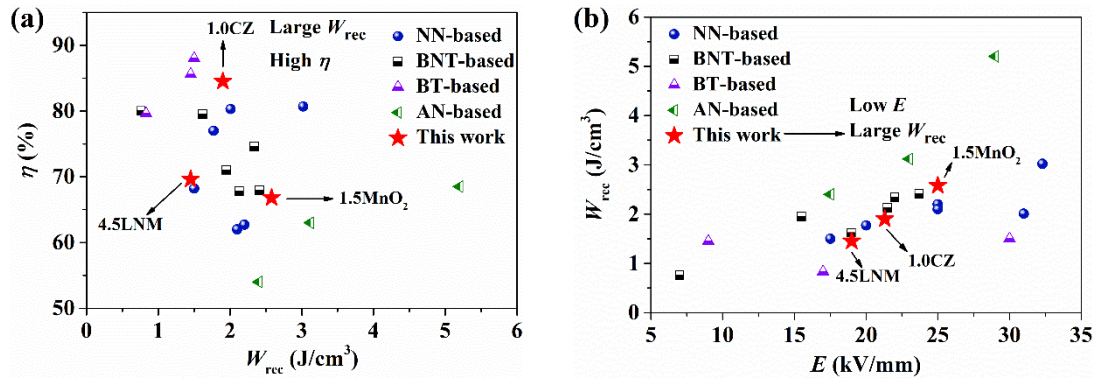
were well narrowed, demonstrating no FE features (Fig. 5-13(a)). However, the  $P$ - $E$  loops were widened slightly as temperature increased. Therefore, both  $P_{\max}$  and  $\Delta P$  grew gradually during 30-70 °C, and then they almost remained unchanged from 70 °C to 90 °C, as shown in Fig. 5-13(b). Conversely,  $P_r$  kept growing with the increase in temperature. This is the result of the combined effect of thermal motion of domains, enhanced anti-ferroelectricity and reduced PNRs. Correspondingly, influenced by  $\Delta P$  and the WHL,  $W_{\text{rec}}$  showed an increase-decrease trend as increasing temperature, reaching the maximum value of 1.36 J/cm<sup>3</sup> at 70 °C (Fig. 5-13(c)). Although  $\eta$  dropped gradually with the increase in temperature, it remained a considerable value of 81.3% even at a higher temperature (90 °C), as shown in Fig. 5-13(d). Simultaneously,  $W_{\text{ch}}$  showed a similar change with  $W_{\text{rec}}$ , while  $W_{\text{loss}}$  grew slightly with the increase in temperature. In addition, from 30 °C to 90 °C,  $\eta$  showed a reduction of 4.1%, while a fluctuation of 11.5% in  $W_{\text{rec}}$  was presented. It can be found that this system reveals attractive thermal stability.



**Fig. 5-13** Energy storage performance of 1.0CZ ceramics as a function of temperature for (a)  $P$ - $E$  loops, (b) the  $P_r$ ,  $P_{\max}$  and  $\Delta P$  values, (c) the  $W_{\text{rec}}$  and  $W_{\text{ch}}$ , and (d) the  $W_{\text{loss}}$  and  $\eta$  values.



To estimate the energy storage performance in our study, that of 0.955NN-0.045LNM (4.5LNM), 0.955NN-0.045LNM-1.5%MnO<sub>2</sub> (1.5MnO<sub>2</sub>), and 1.0CZ ceramics in this work and commonly-used lead-free energy storage ceramics in other reports is summarized. The  $\eta$  versus  $W_{\text{rec}}$  is displayed in Fig. 5-14(a), and  $W_{\text{rec}}$  under different electric field is shown in Figs. 5-14(b). A moderate  $W_{\text{rec}}$  of 1.45 J/cm<sup>3</sup> is achieved in 4.5LNM ceramics under a relatively low electric field (19.0 kV/mm), while 1.5MnO<sub>2</sub> reaches a superior  $W_{\text{rec}}$  of 2.58 J/cm<sup>3</sup> under a moderate electric field (25.0 kV/mm). In 1.0CZ ceramics, large  $W_{\text{rec}}$  of 1.90 J/cm<sup>3</sup> and superior  $\eta$  of 84.5% are obtained simultaneously under a low external electric field (21.3 kV/mm), which are superior to most promising lead-free ceramics. All above achievements satisfy the requirement of high energy storage performance under low electric fields and indicates the feasibility of the proposed design strategy in this work.

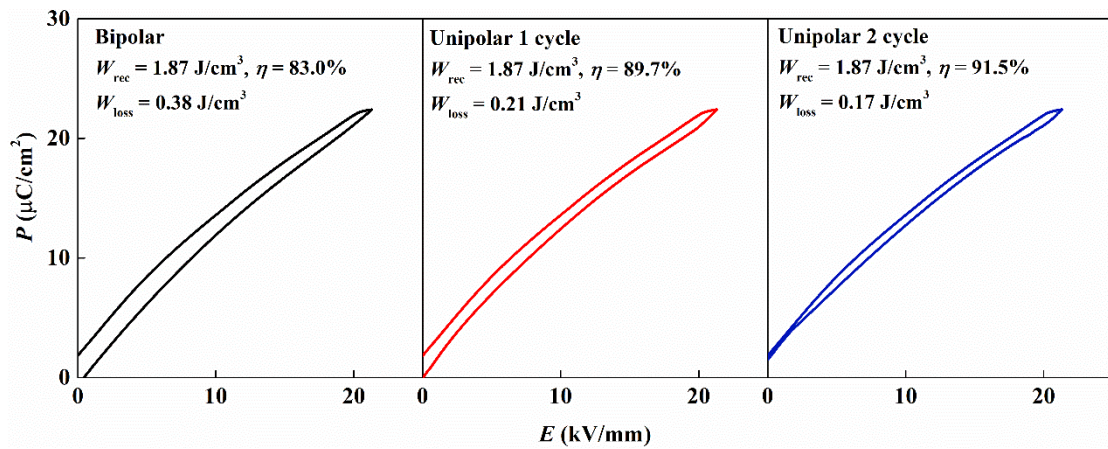


**Fig. 5-14** Comparisons of (a)  $\eta$  versus  $W_{\text{rec}}$ , (b)  $W_{\text{rec}}$  versus  $E$  between 4.5LNM, 1.5MnO<sub>2</sub>, 1.0CZ and reported NN-<sup>[2,4,6-9]</sup>, (Bi<sub>0.5</sub>Na<sub>0.5</sub>)TiO<sub>3</sub> (BNT)-<sup>[10-15]</sup>, BaTiO<sub>3</sub> (BT)-<sup>[16-18]</sup>, and AgNbO<sub>3</sub> (AN)-based<sup>[19-21]</sup> bulk lead-free ceramics.

### 5.2.5 Energy storage efficiency under unipolar electric field

In addition, the energy storage properties of 1.0CZ (not the same one as above) were respectively detected under unipolar and bipolar electric field at 21.3 kV/mm, as displayed in Fig. 5-15. It can be found that the  $\eta$  under unipolar condition was superior to that under bipolar cycle, while the  $W_{\text{rec}}$  was not significantly affected. Because under

the unipolar condition, there are fewer reverse dipoles, leading to less energy loss. Furthermore, after the second unipolar cycle, the  $P$ - $E$  loops became much slimmer with a non-zero starting point ( $P_r > 0$ ). As a result, the  $\eta$  was enlarged and could reach above 90%. The remaining energy loss may be caused by thermal losses and non-polar dipole steering. Compared with the bipolar cycle, the  $W_{\text{loss}}$  is reduced by about 50%, while the  $\eta$  is increased by about 8.1% under the unipolar (1 cycle) conditions. Overall, the application under unipolar conditions will provide elevated potential.



**Fig. 5-15** Energy storage behaviors of the 1.0CZ (not the same one as above) ceramics under 21.3 kV/mm as functions of cycle number.

### 5.3 Summary

The pure perovskite  $\text{NaNbO}_3\text{-La}(\text{Nb}_{1/3}\text{Mg}_{2/3})\text{O}_3\text{-CaZrO}_3$  ternary bulk ceramics with dense and uniform microstructure were successfully prepared through the conventional solid-state method. When CZ is introduced, the sintering temperature is decreased from 1270 °C to 1230 °C, and the dielectric properties are promoted with improved dielectric constant and suppressed dielectric loss. When the addition content is less than 1.7%, CZ is contribute to improve anti-ferroelectricity. In addition, as 1.5% CZ is applied, the phase transition temperatures  $T_C$  and  $T_C'$  are dropped to 196 °C and 38 °C, respectively. Energy storage performance is enhanced by the addition of CZ, the improved  $W_{\text{rec}}$  of 1.90 J/cm<sup>3</sup> and favourable  $\eta$  of 84.5% are obtained simultaneously

for 1.0CZ ceramics under a relatively low electric field of 21.3 kV/mm. Furthermore, unique thermal hysteresis behavior should also be attentioned because  $T_C$ ' also shows influences on electrical properties. Besides, the ceramics demonstrate elevated potential, especially large efficiency, for applications under unipolar electric fields. All presented results illustrate that this lead-free system is highly promising candidates for applications in pulsed power ceramic capacitors.

## References

- [1] F. Yan, H. B. Yang, Y. Lin and T. Wang. *Inorg. Chem.*, **56**, 13510, 2017.
- [2] J. M. Ye, G. S. Wang, X. F. Chen and X. L. Dong. *J. Materiomics*, **7**, 339, 2021.
- [3] M. Emmanuel, H. Hao, H. X. Liu, A. Jan and F. Alresheedi. *Acs Sustain. Chem. Eng.*, **9**, 5849, 2021.
- [4] Z. T. Yang, H. L. Du, L. Jin, Q. Y. Hu, S. B. Qu, Z. N. Yang, Y. Yu, X. Y. Wei and Z. Xu. *J. Eur. Ceram. Soc.*, **39**, 2899, 2019.
- [5] J. K. Liu, Y. Q. Ding, C. Y. Li, W. F. Bai, P. Zheng, J. J. Zhang and J. W. Zhai. *J. Mater. Sci.: Mater. El.*, **32**, 21164, 2021.
- [6] J. Q. Ma, Y. Lin, H. B. Yang and J. H. Tian. *J. Alloys Compd.*, **868**, 2021.
- [7] M. Zhou, R. Liang, Z. Zhou, S. Yan and X. Dong. *ACS Sustain. Chem. Eng.*, **6**, 12755, 2018.
- [8] Y. Z. Fan, Z. Y. Zhou, R. H. Liang and X. L. Dong. *J. Eur. Ceram. Soc.*, **39**, 4770, 2019.
- [9] J. T. Wang, X. R. Nie, Z. H. Peng, X. P. Lei, P. F. Liang, Z. P. Yang and X. L. Chao. *Ceram. Int.*, **47**, 28493, 2021.
- [10] Y. P. Pu, M. T. Yao, L. Zhang and M. Chen. *J. Alloys Compd.*, **702**, 171, 2017.
- [11] L. Zhang, Y. P. Pu, M. Chen and G. Liu. *J. Eur. Ceram. Soc.*, **38**, 5388, 2018.
- [12] H. B. Yang, F. Yan, Y. Lin and T. Wang. *Energy Technol.*, **6**, 357, 2018.
- [13] F. D. Zhang, X. S. Qiao, Q. Y. Zhou, Q. Q. Shi, X. L. Chao, Z. P. Yang and D. Wu. *J. Alloys Compd.*, **875**, 160005, 2021.
- [14] Y. H. Wan, N. J. Hou, P. R. Ren, F. X. Yan, Z. R. Li, M. Ma, K. X. Song and G. Y. Zhao. *J. Am. Ceram. Soc.*, **104**, 5138, 2021.
- [15] F. Yan, H. B. Yang, L. Ying and T. Wang. *J. Mater. Chem. C*, **6**, 7905, 2018.
- [16] C. Q. Zhu, Z. M. Cai, L. M. Guo, L. T. Li and X. H. Wang. *J. Am. Ceram. Soc.*, **104**, 273, 2021.
- [17] H. Y. Wang, M. H. Cao, C. Tao, H. Hao, Z. H. Yao and H. X. Liu. *J. Alloys Compd.*, **864**, 158644, 2021.

- [18] J. P. Ma, X. M. Chen, W. Q. Ouyang, J. Wang, H. Li and J. L. Fang. *Ceram. Int.*, **44**, 4436, 2018.
- [19] A. Z. Song, J. M. Song, Y. K. Lv, L. L. Liang, J. Wang and L. Zhao. *Mater. Lett.*, **237**, 278, 2019.
- [20] N. N. Luo, K. Han, L. J. Liu, B. L. Peng, X. P. Wang, C. Z. Hu, H. F. Zhou, Q. Feng, X. Y. Chen and Y. Z. Wei. *J. Am. Ceram. Soc.*, **102**, 4640, 2019.
- [21] N. N. Luo, K. Han, F. P. Zhuo, C. Xu, G. Z. Zhang, L. J. Liu, X. Y. Chen, C. Z. Hu, H. F. Zhou and Y. Z. Wei. *J. Mater. Chem. A*, **7**, 15450, 2019.

## Chapter 6

### Electrocaloric Effect and Phase Diagram

#### 6.1 Introduction

The complexity of thermal-induced phase structures in  $\text{NaNbO}_3$  (NN) ceramics has been confirmed by researchers, and there still exist debates on the specific phase transition process.<sup>[1]</sup> As well known, different chemical modifications can also alter the phase structure as well as affect the phase transition behavior.<sup>[2,3]</sup> In this work, binary  $\text{NaNbO}_3\text{-La}(\text{Nb}_{1/3}\text{Mg}_{2/3})\text{O}_3$  (NN-LNM) system and  $\text{NaNbO}_3\text{-La}(\text{Nb}_{1/3}\text{Mg}_{2/3})\text{O}_3\text{-CaZrO}_3$  (NN-LNM-CZ) ternary system are studied for the first time. Therefore, it is essential to describe the phase diagram for further studies and applications.

In addition, although NN-based materials have been studied for several decades, only a few reports have been focused on electrocaloric effect (ECE) of NN-based ceramics.<sup>[4]</sup> The ECE refers to the reversible adiabatic temperature change ( $\Delta T$ ) and/or isothermal entropy change ( $\Delta S$ ) of polar materials with the application or removal of an external electric field.<sup>[5]</sup> The most studied lead-free ECE ceramics are summarized in Table 6-1. It has attracted significant attention in recent years due to the increasing demand for cooling solutions for micro- and nano-electronic devices.<sup>[6]</sup> It usually presents the highest value near phase transition, especially at a temperature slightly above the phase transition temperature.<sup>[7]</sup> Thus, a mixed phase will benefit the changes in polarization and entropy to enhance the electrocaloric (EC) response. In this work, the typical compounds coexist as anti-ferroelectric (AFE) and ferroelectric (FE) phases, demonstrating promising potentials for EC applications.

**Table 6-1** ECE performances of commonly-studied lead-free bulk materials.

Sample	Category	$T$ (°C)	$\Delta S$ (J/kg·K)	$\Delta T$ (K)	$ \Delta T/\Delta E $ (K·mm/kV)	Ref.
(Na <sub>0.5</sub> Bi <sub>0.5</sub> )TiO <sub>3</sub> -based	ceramic	100	2.20	1.50	0.300	[8]
(Na <sub>0.5</sub> Bi <sub>0.5</sub> )TiO <sub>3</sub> -based	ceramic	60	2.52	1.64	0.330	[9]
(K, Na)NbO <sub>3</sub> -based	ceramic	77		0.51	0.128	[4]
BaTiO <sub>3</sub> -based	ceramic	130	1.78	1.64	0.234	[7]
BaTiO <sub>3</sub> -based	ceramic	85		2.33	0.058	[10]

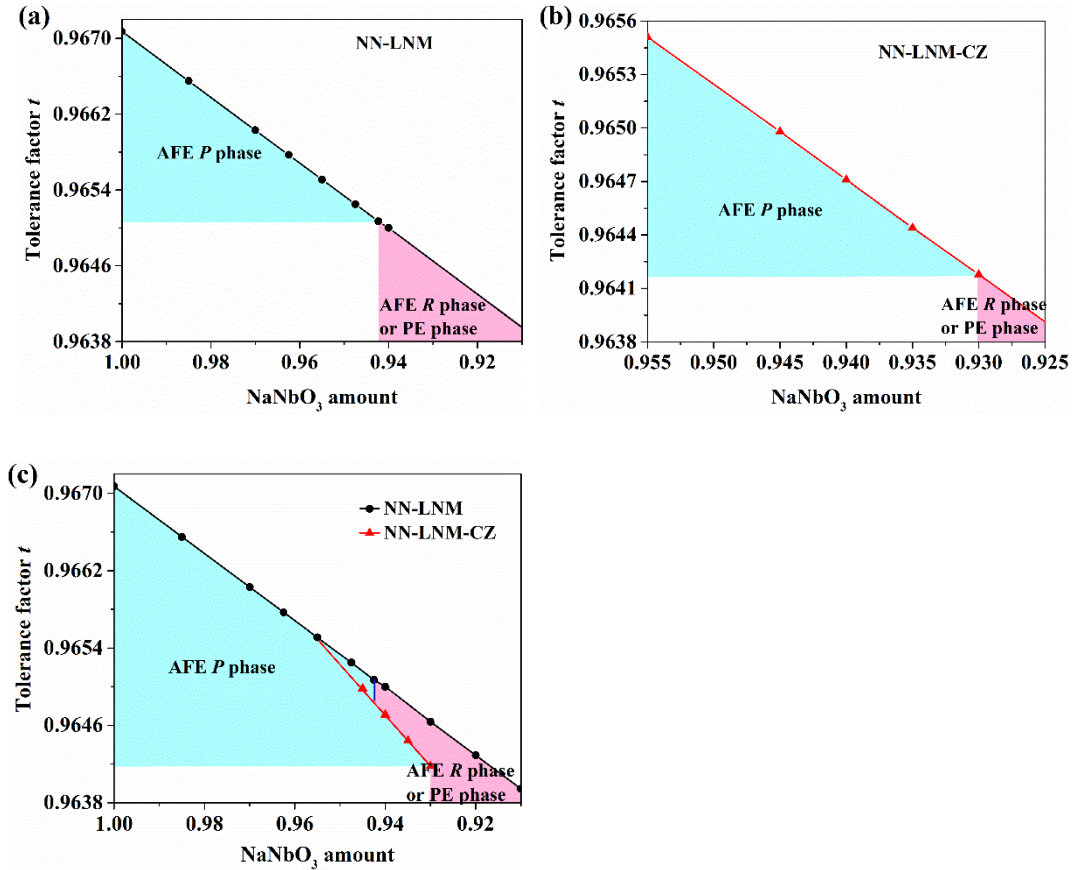
In this chapter, there exist two main purposes. One involves the construction of phase diagrams induced by chemical modifications as well as the decrease in tolerance factor  $t$ . The other is to study the ECE performance of NN-based ceramics.

## 6.2 Construction of Phase Diagram

According to above analysis, the addition of La(Nb<sub>1/3</sub>Mg<sub>2/3</sub>)O<sub>3</sub> (LNM) and CaZrO<sub>3</sub> (CZ) can effectively stabilize the nonpolar AFE phase in NN ceramics induced by a reduction in tolerance factor. Nevertheless, there exist phase boundaries between AFE  $P$  phase, AFE  $R$  phase and para-electric (PE) phase with the increase in additive amount. Therefore, it is essential to describe the influences of chemical dopants on phase structure and phase transition behavior.

The room temperature (RT) phase structure in proportion to NN amount and tolerance factor was constructed, which involves AFE and PE distortion structures, as shown in Fig. 6-1. Although the increase in LNM amount (reduced tolerance factor) can stabilize the AFE  $P$  phase in NN ceramics, an excessive addition will suddenly provoke an AFE  $R$  or PE phase instead of the AFE  $P$  phase. Figure 6-1(a) displays the phase structure distortions of NN-LNM systems, it can be found that the AFE  $P$  phase (blue area) was stabilized when LNM amount is below 5.75% ( $t \geq 0.96507$ ). However, it was transformed into AFE  $R$ /PE structure (red area) with a further increase in LNM amount, while the phase structure within the white rectangular area was not ensured. When the third component (CZ) was employed, the stabilized AFE  $P$  range was widened with additive (LNM and CZ) amount below 6.5%, as revealed in Fig. 6-1(b).

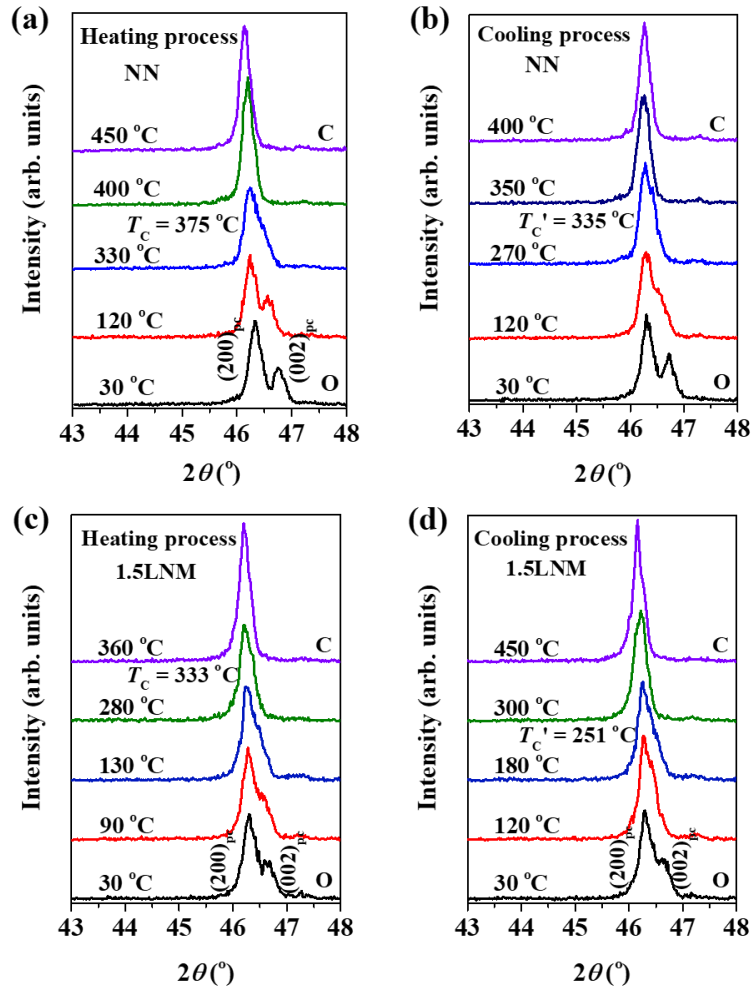
These two systems are integrated together in Fig. 6-1(c), the multivariate systems can effectively broaden the AFE *P* range. It can be inferred that the AFE *P* range may be further broadened when a fourth component is introduced.



**Fig. 6-1** The room temperature phase structure involves AFE and PE distortion in NN-based ceramics for (a) NN-LNM system, (b) NN-LNM-CZ system, and (c) NN-LNM and NN-LNM-CZ systems.

To construct the temperature-dependent phase diagram, high temperature X-ray diffraction (XRD) measures were carried out for NN and 0.985NN-0.015LNM (1.5LNM) ceramics, as displayed in Fig. 6-2. As temperature increased, the double diffraction peaks (or asymmetric single peaks) were changed into a symmetrical one. It reveals that the crystal structure was gradually transformed from orthorhombic (O) AFE *P* phase to AFE *R* phase,<sup>[11,12]</sup> and the phase transition temperatures ( $T_C$ ,  $T_C'$ ) were extracted from the dielectric measurements.



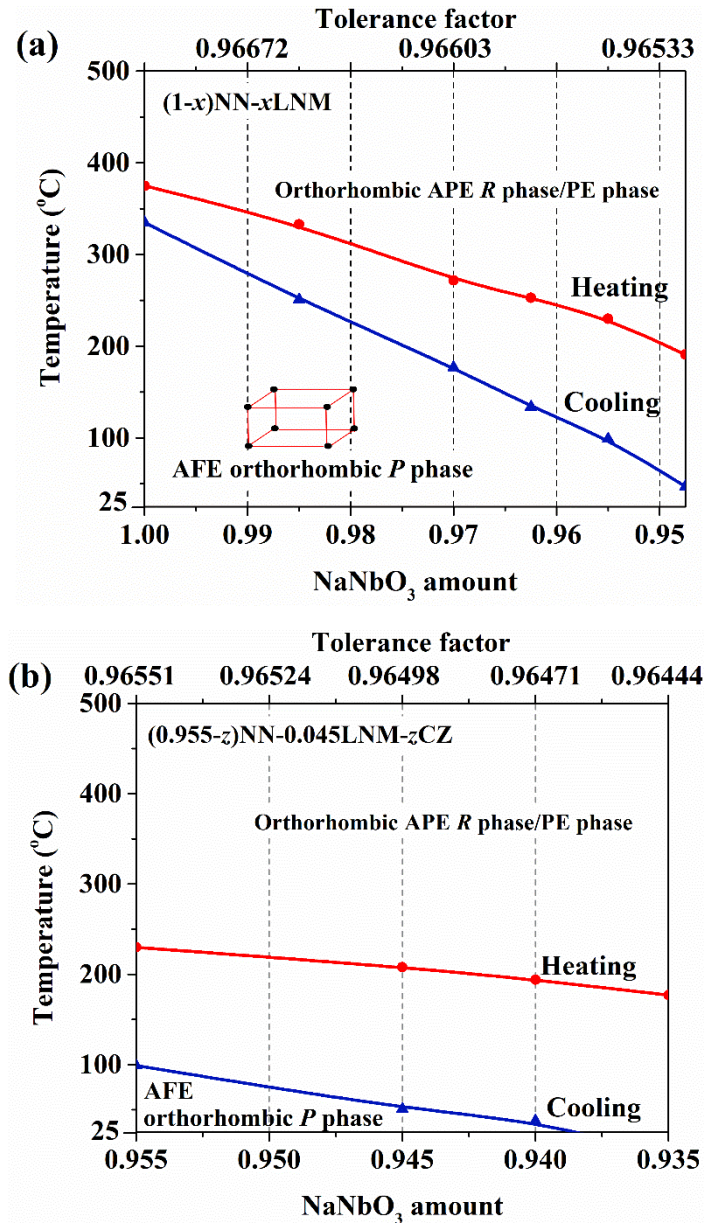


**Fig. 6-2** High temperature XRD patterns of (a, b) NN ceramics and (c, d) 1.5LNM ceramics.

Based on the XRD and dielectric analysis, the temperature-dependent phase diagram was constructed, as described in Fig. 6-3. To describe the influence of tolerance factor, it is also plotted on the horizontal axis as another parameter. Figure 6-3(a) demonstrates the phase transition behavior of binary  $(1-x)\text{NN}-x\text{LNM}$  system. As observed, the samples possessed an AFE *P* phase with O crystal structure, and it gradually approached AFE *R* phase. As temperature increased, the phase structure was also transformed into an AFE *R* phase and then changed into a PE phase, however the phase transition temperature between these two phases were not ensured. Alternatively, during cooling, the phase transition temperature ( $T_C'$ ) was much lower as compared with the heating process. The similar behavior was observed in ternary  $(0.955-z)\text{NN}-0.045\text{LNM}-z\text{CZ}$  system, while the AFE *P* was gradually turned into AFE *R* phase at RT,

as shown in Fig. 6-3(b). In addition, both  $T_C$  and  $T_C'$  decreased obviously with the reduction in NN amount and tolerance factor.

It can be concluded that the thermal hysteresis will suppress the AFE  $P$  range. Thus, during the construction of AFE phase in NN materials, equal attention should be given to the cooling process.



**Fig. 6-3** Temperature-dependent phase diagram of chemical modified NN ceramics for (a)  $(1-x)\text{NN}-x\text{LNM}$  binary system and (b)  $(0.955-z)\text{NN}-0.045\text{LNM}-z\text{CZ}$  ternary system.

### 6.3 Electrocaloric Effect of NaNbO<sub>3</sub>-Based Ceramics

In this section, the EC properties for 0.955NN-0.045LNM (4.5LNM), 0.955NN-0.045LNM-1.5%MnO<sub>2</sub> (1.5MnO<sub>2</sub>), and 0.945NN-0.045LNM-0.01CaZrO<sub>3</sub> (1.0CZ) were investigated. The ECE of all samples were calculated according to Eqs. (1-11) and (1-12) in Chapter 1. The temperature-dependent polarization  $P$ - $T$  data were extracted from above branches of temperature-dependent hysteresis  $P$ - $E$  loops, and the  $(\partial P/\partial T)_E$  values were obtained from the polynomial fitting of  $P$ - $T$  data.

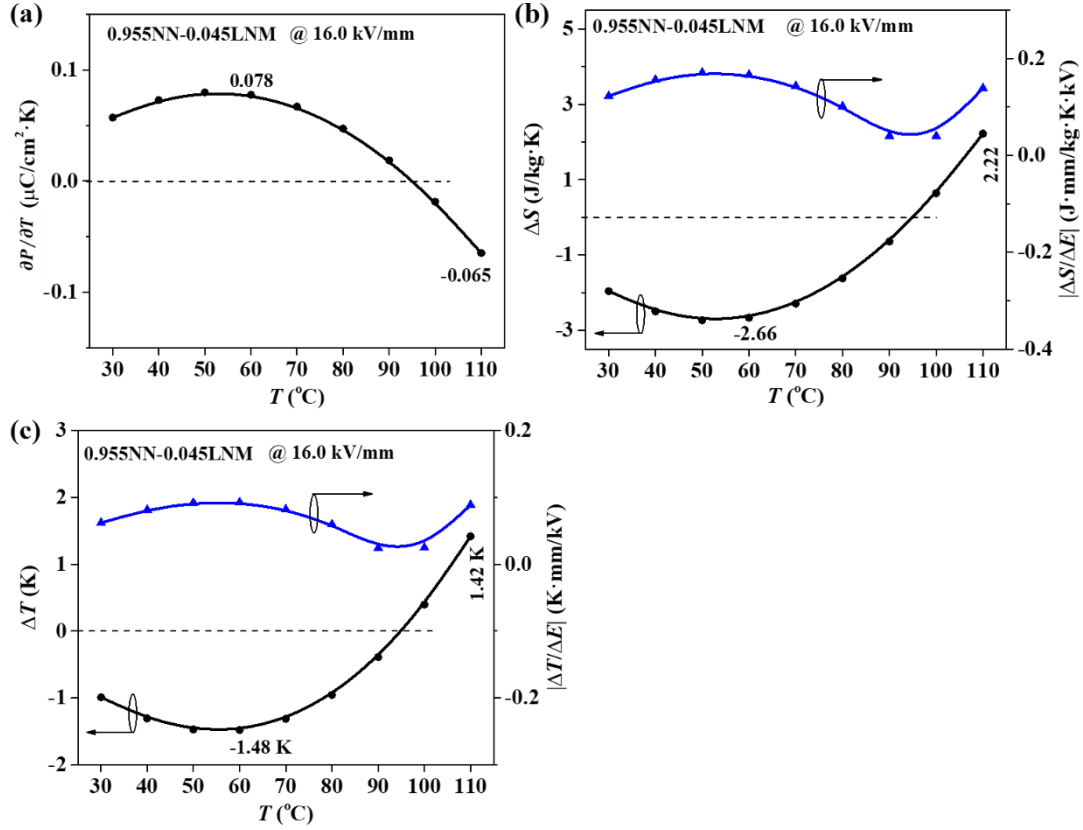
#### 6.3.1 Electrocaloric effect of 4.5LNM ceramics

The ECE performance of 4.5LNM ceramics shown in Fig. 6-4, which was measured at 16.0 kV/mm. In Fig. 6-4(a), the  $(\partial P/\partial T)_E$  increased from a positive value to the maximum positive value (0.078  $\mu\text{C}/\text{cm}^2\cdot\text{K}$ ) at 60 °C. And then it decreased, the negative values were obtained at 100 °C and 110 °C. The entropy change  $\Delta S$  and temperature change  $\Delta T$  are displayed in Figs. 6-4(b) and 6-4(c), respectively. As seen, positive ECE ( $\Delta S > 0$ ,  $\Delta T > 0$ ) and negative ECE ( $\Delta S < 0$ ,  $\Delta T < 0$ ) were simultaneously observed for 4.5LNM ceramics, which can strengthen the EC efficiency.<sup>[13]</sup> This originates from the mixed structure of AFE and FE phases as positive and negative ECE are usually obtained in FE and AFE materials, respectively.<sup>[14,15]</sup>

The optimum negative EC response was observed at 60 °C, achieving a high  $\Delta T$  of -1.48 K with  $\Delta S = -2.66$  J/kg·K. Considering the large applied electric field, the negative EC response should not be caused by thermal stimulating effect of dipole orientation that usually occurs at lower electric field, but as a result of the first-order phase transition.<sup>[7]</sup> In addition, an alluring positive ECE with  $\Delta T$  of 1.42 K,  $\Delta S$  of 2.22 J/kg·K was obtained at 110 °C. Noteworthy, this comparable  $\Delta T$  is of great potential for lead-free bulk ceramics.

The EC responsivity ( $|\Delta T/\Delta E|$ ) also shows an important effect on practical applications, which is superior for bulk ceramics as compared to thin films.<sup>[16-18]</sup> Therefore, it is also plotted in Fig. 6-4(c) as the other figure of merit, the largest  $|\Delta T/\Delta E|$  value of 0.092 K·mm/kV was observed at 60 °C, which is slightly lower than that of

lead-based ceramics.<sup>[19]</sup> This may be generated from different polarization responses under larger electric fields such as domain switching, domain transformation, field-induced phase transition, and dielectric polarization.<sup>[7]</sup>



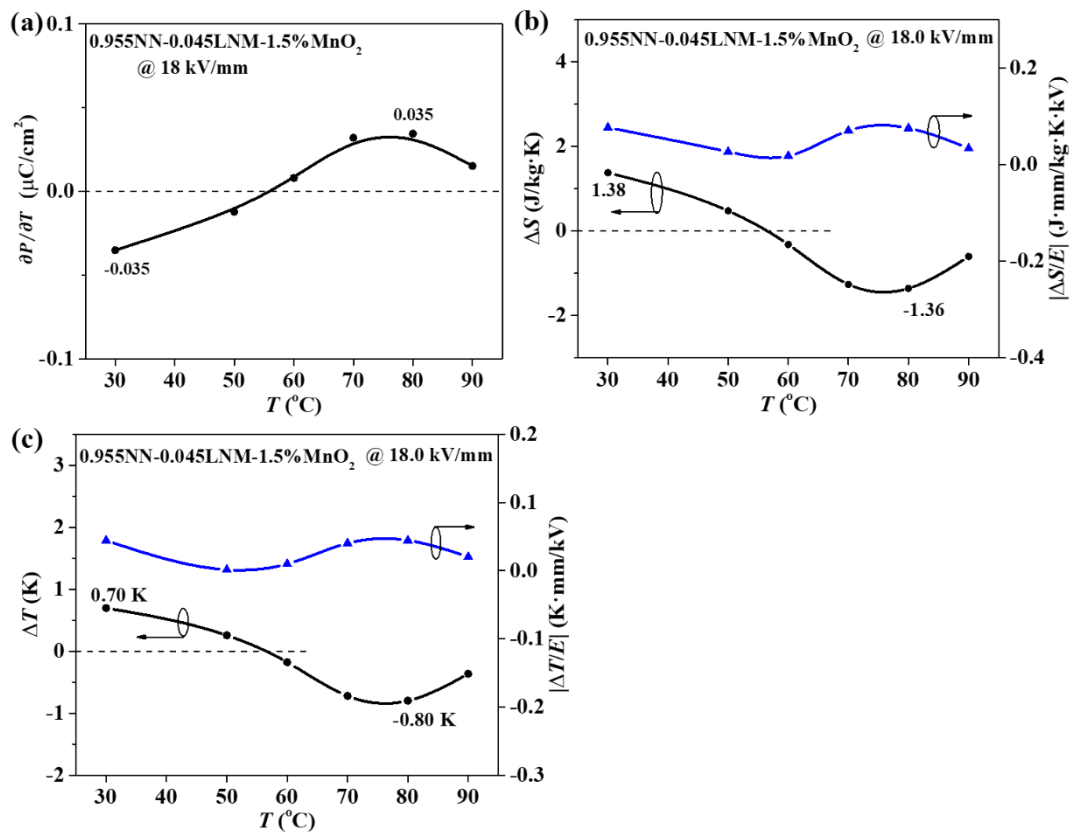
**Fig. 6-4** ECE performance of 4.5LNM ceramics for (a)  $\partial P/\partial T$  values, (b)  $\Delta S$  and  $|\Delta S/\Delta E|$ , and (c)  $\Delta T$  and  $|\Delta T/\Delta E|$ .

### 6.3.2 Electrocaloric effect of 1.5MnO<sub>2</sub> ceramics

The EC performance of 1.5MnO<sub>2</sub> ceramics is shown in Fig. 6-5. Observably, the  $(\partial P/\partial T)_E$  demonstrated the smallest value of  $-0.035 \mu\text{C}/\text{cm}^2\cdot\text{K}$  at 30 °C, and it increased to the maximum positive value of  $0.035 \mu\text{C}/\text{cm}^2\cdot\text{K}$  at 80 °C. Consequently, both  $\Delta S$  and  $\Delta T$  presented a decrease trend from 30 °C to 80 °C, and then increased, as displayed in Figs. 6-5(b, c). It also revealed a mixed behavior of positive ECE and negative ECE. The positive ECE was achieved at 30-50 °C, while it demonstrated

negative ECE from 60 °C to 90 °C. As a result, the maximum positive  $\Delta T$  of 0.70 K was obtained at 30 °C, while the optimum negative ECE was achieved at 80 °C with  $\Delta T$  of -0.80 K. Although the working temperature of 30 °C is very close to ambient conditions, the EC response is not sufficient for applications. As  $\text{MnO}_2$  was introduced, the thermal dependence of polarization was weakened, reducing the EC response.

Although an excellent ECE performance was not observed for 1.5 $\text{MnO}_2$  ceramics, the coexistence of positive and negative ECE is also attractive for further studies.



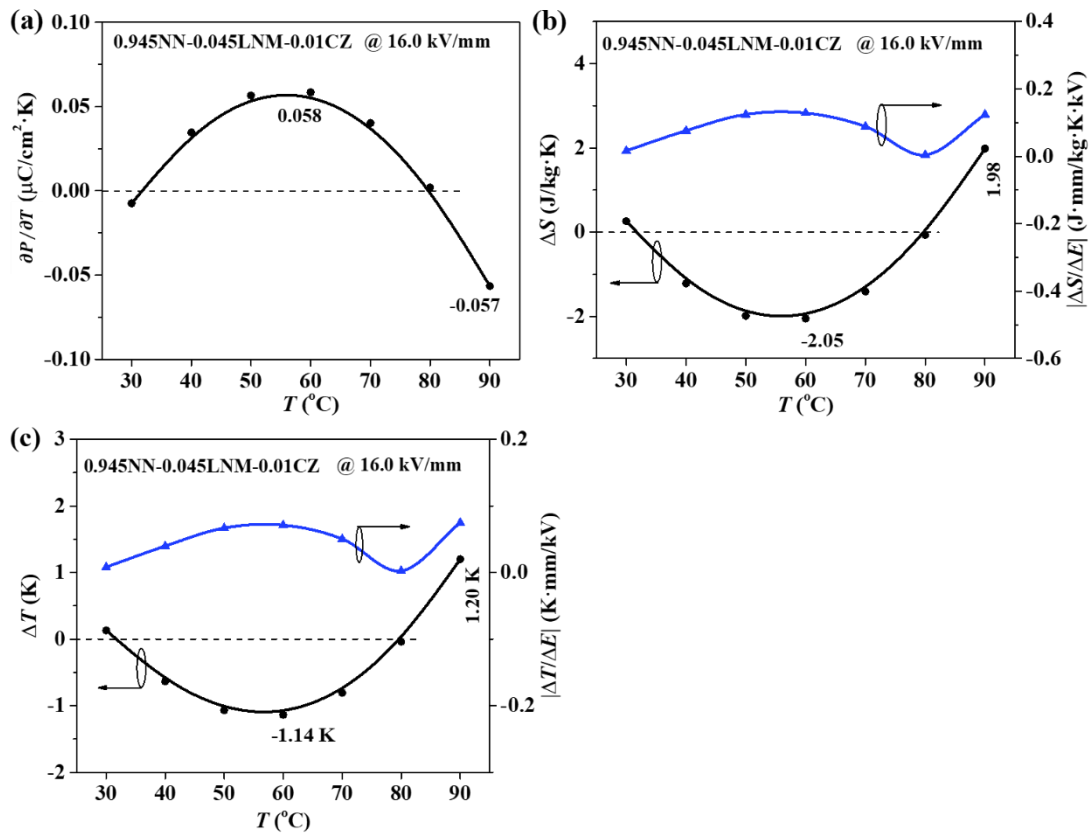
**Fig. 6-5** ECE performance of 1.5 $\text{MnO}_2$  ceramics for (a)  $\partial P/\partial T$  values, (b)  $\Delta S$  and  $|\Delta S/\Delta E|$ , and (c)  $\Delta T$  and  $|\Delta T/\Delta E|$ .

### 6.3.3 Electrocaloric effect of 1.0CZ ceramics

The EC response of 1.0CZ ceramics was also realized at 16.0 kV/mm within the temperature range of 30-90 °C, as revealed in Fig. 6-6. Significantly, 1.0CZ displayed

unique EC characteristics different from those of the 4.5LNM and 1.5MnO<sub>2</sub> ceramics. As shown in Fig. 6-6(a), the  $(\partial P/\partial T)_E$  values presented two negative segments at 30 °C and 90 °C, achieving the optimum negative value of of -0.057  $\mu\text{C}/\text{cm}^2\cdot\text{K}$  at 90 °C. Alternatively, the positive values were observed at 40-80 °C and it existed a maximum positive point of 0.058  $\mu\text{C}/\text{cm}^2\cdot\text{K}$  at 60 °C.

In Figs. 6-6(b, c), similar trends were observed for  $\Delta S$  and  $\Delta T$ , demonstrating a decrease-increase change. The coexistence of positive ECE and negative ECE was also presented, existing positive ECE at 30 °C and 90 °C, while a negative EC response was observed in a temperature range of 40-80 °C. As a result, the optimum negative ECE,  $\Delta T = -1.14$  K,  $\Delta S = -2.05$  J/kg·K,  $|\Delta T/\Delta E| = 0.071$  K·mm/kV, was obtained at 60 °C. The largest positive  $\Delta T$  of 1.20 K with  $\Delta S = 1.98$  J/kg·K,  $|\Delta T/\Delta E| = 0.075$  K·mm/kV was achieved at 90 °C. Although the  $|\Delta T/\Delta E|$  only presented a moderate level, both the negative  $\Delta T$  and positive  $\Delta T$  are worthy of further academic and industrial studies.



**Fig. 6-6** ECE performance of 1.0CZ ceramics for (a)  $\partial P/\partial T$  values, (b)  $\Delta S$  and  $|\Delta S/\Delta E|$ , and (c)  $\Delta T$  and  $|\Delta T/\Delta E|$ .

In contrast, the ECE performance of 4.5LNM, 1.5MnO<sub>2</sub>, and 1.0CZ ceramics are summarized in Table 5-2. As discussed above, the introduction of MnO<sub>2</sub> and CZ can improve the thermal stability, which is adverse to EC response. Hence, it can be concluded that the EC parameters are reduced with the addition of CZ and MnO<sub>2</sub>, while the slight reduction in working temperature is magnetic. Significantly, all three samples displayed a unique mixed positive and negative ECE. A negative ECE indicates that the materials are cooled upon the application of an external electric field, whereas they heat up when the electric field is withdrawn. This effect may enlarge the EC family and enhance the cooling efficiency. It is known that  $|\Delta T/\Delta E|$  can be employed to compare ECE performances for different materials.<sup>[20]</sup> The addition of MnO<sub>2</sub> and CZ leads to a reduction in  $|\Delta T/\Delta E|$ , demonstrating adverse effects.

**Table 6-2** ECE performance of 4.5LNM, 1.5MnO<sub>2</sub>, 1.0CZ ceramics.

Sample	$T$ (°C)	$\Delta E$ (kV/mm)	$\Delta S$ (J/kg·K)	$\Delta T$ (K)	$ \Delta T/\Delta E $ (K·mm/kV)
4.5LNM	60	16.0	-2.66	-1.48	0.092
	110	16.0	2.22	1.42	0.089
1.5MnO <sub>2</sub>	30	18.0	1.38	0.70	0.044
	80	18.0	-1.36	-0.80	0.045
1.0CZ	60	16.0	-2.05	-1.14	0.071
	90	16.0	1.98	1.20	0.075

## 6.4 Summary

The RT phase diagram and temperature-induced phase diagram according to NN amount and tolerance factor are constructed involving the AFE *P*, AFE *R*, and PE phases. A stabilized AFE *P* phase can be constructed when LNM amount is lower than 5.75% in binary NN-LNM system, while this range can be extended to 6.5% of additive amount in ternary NN-LNM-CZ system. Simultaneously, the phase transition temperatures are reduced with the addition of additives, so the equal attention should

be given to the cooling process. These offer a feasible method to improve anti-ferroelectricity in NN-based ceramics with a reduced tolerance factor. In addition, the EC performance of 4.5LNM, 1.5MnO<sub>2</sub>, and 1.0CZ ceramics shows an attractive behavior. They demonstrate a coexistence of positive ECE and negative ECE, which can improve refrigeration efficiency. A superior EC performance is observed for 4.5LNM ceramics, presenting the optimum negative ECE at 60 °C with  $\Delta T$  of -1.48 K as well as improved positive ECE at 110 °C with  $\Delta T$  of 1.42 K.



## References

- [1] M. Tyunina, A. Dejneka, D. Rytz, I. Gregora, F. Borodavka, M. Vondracek and J. Honolka. *J. Phys.: Condens. Mat.*, **26**, 125901, 2014.
- [2] J. G. Wu, D. Q. Xiao and J. G. Zhu. *Chem. Rev.* **115**, 2559, 2015.
- [3] X. P. Wang, J. G. Wu, D. Q. Xiao, J. G. Zhu, X. J. Cheng, T. Zheng, B. Y. Zhang, X. J. Lou and X. J. Wang. *J. Am. Chem. Soc.*, **136**, 2905, 2014.
- [4] X. Wang, J. Wu, B. Dkhil, B. Xu, X. Wang, G. Dong, G. Yang and X. Lou. *Appl. Phys. Lett.*, **110**, 063904, 2017.
- [5] S. P. Alpay, J. Mantese, S. Trolier-McKinstry, Q. Zhang and R. W. Whatmore. *MRS Bull.*, **39**, 1099, 2014.
- [6] Y. V. Sinyavsky, G. E. Lugansky and N. D. Pashkov. *Cryogenics*, **32**, 28, 1992.
- [7] X. Nie, S. Yan, S. Guo, F. Cao, C. Yao, C. Mao, X. Dong and G. Wang. *J. Am. Ceram. Soc.*, **100**, 5202, 2017.
- [8] W. P. Cao, W. L. Li, D. Xu, Y. F. Hou, W. Wang and W. D. Fei. *Ceram. Int.*, **40**, 9273, 2014.
- [9] W. P. Cao, W. L. Li, X. F. Dai, T. D. Zhang, J. Sheng, Y. F. Hou and W. D. Fei. *J. Eur. Ceram. Soc.*, **36**, 593, 2016.
- [10] J. Wang, T. Yang, S. Chen, G. Li, Q. Zhang and X. Yao. *J. Alloys Compd.*, **550**, 561, 2013.
- [11] S. K. Mishra, R. Mittal, V. Y. Pomjakushin and S. L. Chaplot. *Phys. Rev. B*, **83**, 134105, 2011.
- [12] A. Tian, R. Z. Zuo, H. Qi and M. Shi. *J. Mater. Chem. A*, **8**, 8352, 2020.
- [13] X. Nie, S. Yan, X. Chen, S. Guo, F. Cao, C. Yao, C. Mao, X. Dong and G. Wang. *Phys. Status Solidi A*, **215**, 1700971, 2018.
- [14] W. P. Geng, Y. Liu, X. J. Meng, L. Bellaiche, J. F. Scott, B. Dkhil and A. Q. Jiang. *Adv. Mater.*, **27**, 3165, 2015.
- [15] P. F. Zhao, S. B. Wang, H. Tang, X. D. Jian, X. B. Zhao, Y. B. Yao, T. Tao, B. Liang and S. G. Lu. *Scripta Mater.*, **200**, 113920, 2021.

- [16] X. S. Qian, H. J. Ye, Y. T. Zhang, H. M. Gu, X. Y. Li, C. A. Randall and Q. M. Zhang. *Adv. Funct. Mater.*, **24**, 1300, 2014.
- [17] B. L. Peng, H. Q. Fan and Q. Zhang. *Adv. Funct. Mater.*, **23**, 2987, 2013.
- [18] M. H. Park, H. J. Kim, Y. J. Kim, T. Moon, K. D. Kim, Y. H. Lee, S. D. Hyun and C. S. Hwang. *Adv. Mater.*, **28**, 7956, 2016.
- [19] V. V. Shvartsman, E. D. Politova. *Ferroelectrics*, **257**, 75, 2001.
- [20] F. L. Goupil, R. McKinnon, V. Koval, G. Viola, S. Dunn, A. Berenov, H. Yan and N. M. Alford. *Sci. Rep.*, **6**, 28251, 2016.

## Chapter 7

### Conclusions

With the concern for human health and environmental protection requirements, the development of lead-free energy storage ceramics has become an essential. In this work, modified  $\text{NaNbO}_3$  (NN) ceramics were investigated for energy storage as one of the most promising substitutes for lead-based ceramics due to its anti-ferroelectric (AFE) phase structure.

To enhance the energy storage properties in NN-based ceramics,  $\text{La}(\text{Nb}_{1/3}\text{Mg}_{2/3})\text{O}_3$  (LNM) was introduced to enhance anti-ferroelectricity at room temperature (RT) with a decrease in tolerance factor. The AFE structure was stabilized with orthorhombic  $P$  phase, and it was gradually transformed into AFE  $R$  phase with the increase in LNM amount. The dielectric constant was efficiently improved with the addition of LNM, coupled with a localized hopping conduction mechanism. When 5.25% LNM was employed, the phase transition temperature ( $T_C$ ) decreased from 375 °C to 192 °C, while that ( $T_C'$ ) of cooling process reduced from 335 °C to 47 °C. The 0.955NN-0.045LNM exhibited optimum energy storage properties with recoverable energy storage density ( $W_{\text{rec}}$ ) of 1.45 J/cm<sup>3</sup> and efficiency ( $\eta$ ) of 69.6% under a lower electric field of 19.0 kV/mm. And a fluctuation of 11.5% in  $W_{\text{rec}}$  and 8.0% reduction in  $\eta$  were observed in a temperature range of 30-110 °C. This scheme provides a route for improving energy storage performance and strengthening anti-ferroelectricity in NN-based ceramics, which has rarely been investigated.

A sintering aid,  $\text{MnO}_2$ , was employed to improve sintering performance and dielectric properties in 0.955NN-0.045LNM binary ceramics. The addition of  $\text{MnO}_2$  was beneficial to densify ceramics, which is caused by a liquid phase sintering reaction. Therefore, the optimum sintering temperature was reduced from 1270 °C to 1210 °C. Less volatilization led to an improvement in dielectric performance, demonstrating as

improved dielectric constant and suppressed dielectric loss at RT. Furthermore, the anti-ferroelectricity was maintained with orthorhombic AFE *P* crystal structure when MnO<sub>2</sub> amount was less than 2.0%. As a result, superior energy storage properties were achieved under 25.0 kV/mm as 1.5% MnO<sub>2</sub> was doped, producing  $W_{\text{rec}}$  of 2.58 J/cm<sup>3</sup> and  $\eta$  of 66.8%. In addition, it presented an attractive thermal stability for energy storage. The  $W_{\text{rec}}$  reduced by 4.86%, while  $\eta$  only reduced by 2.75% within a temperature range of 30-60 °C. The energy storage performance is superior to most lead-free ceramics, which is highly promising in electrostatic energy storage devices.

To simultaneously improve  $W_{\text{rec}}$  and  $\eta$ , CZ was employed to tighten the hysteresis *P-E* loops in (0.955-*z*)NN-0.045LNM-*z*CZ ceramics. As CZ content increased, the dielectric properties were promoted with larger dielectric constant as well as lower dielectric loss at RT. The CZ could enhance the AFE behavior with orthorhombic AFE *P* phase when CZ content was controlled within 1.7%. As 1.5% CZ was employed, the  $T_C$  and  $T_C'$  dropped to 196 °C and 38 °C, respectively. Energy storage performance, especially  $\eta$ , had been significantly improved influenced by the narrowed *P-E* loops. Under a low electric field of 21.3 kV/mm, the optimum  $W_{\text{rec}}$  of 1.90 J/cm<sup>3</sup> and favourable  $\eta$  of 84.5% were obtained for 0.945NN-0.045LNM-0.01CZ ceramics. The higher  $\eta$ , improved  $W_{\text{rec}}$  as well as low applied electric field make a great contribution to practical applications. In addition, the ceramics can offer great potential for applications under unipolar electric fields.

The brand-new phase diagrams of binary NN-LNM system and ternary NN-LNM-CZ system were first constructed involving the AFE *P*, AFE *R*, and para-electric (PE) phases. A stabilized AFE *P* phase can be constructed in binary NN-LNM system when additive amount was below 5.75%. While this range could be broadened to 6.5% additive amount in ternary NN-LNM-CZ system. Above this limitation, it was transformed into AFE *R* and PE phase. This provides a valuable guideline for energy storage in NN-based materials involving a reduction in tolerance factor. In addition, the attractive electrocaloric effect (ECE) of 0.955NN-0.045LNM, 0.955NN-0.045LNM-1.5%MnO<sub>2</sub>, 0.945NN-0.045LNM-0.01CZ ceramics was demonstrated. All these samples presented a coexistence of positive ECE and negative ECE, which is rarely

observed in lead-free materials. The vintage ECE was obtained for 0.955NN-0.045LNM ceramics, displaying as best negative ECE with  $\Delta T = -1.48$  K at 60 °C and improved positive ECE with  $\Delta T$  of 1.42 K at 110 °C. The EC response of 0.945NN-0.045LNM-0.01CZ is also attractive with  $\Delta T$  of -1.14 K at 60 °C and  $\Delta T = 1.20$  K at 90 °C. The mixed positive and negative ECE as well as larger  $\Delta T$  possess great attraction for solid refrigeration.

Based on the theoretical research, there exists the orthorhombic AFE phase at RT, which can be stabilized by chemical modification. Although the double hysteresis  $P$ - $E$  loops are not observed in this work, the AFE-liked slim  $P$ - $E$  loops and other AFE characteristics display improved anti-ferroelectricity and attenuated ferroelectricity. With the development of technology, the AFE domains and phase transition behaviors are worthy of in-depth study in the future.

## **Acknowledgements**

First of all, I would like to express my sincere gratitude to my supervisor, Professor Tomoaki Karaki, for his valuable suggestions in the academic researches and continuous support in my daily life. In the preparation of this thesis, he has paid much attention to guiding me and providing me with intelligent advice. Without his patient instruction and insightful criticism, the completion of this thesis would not have been possible. In the course of this research and thesis writing, I not only learned professional knowledge from the tutor, but also learned the innovative way of thinking in scientific research, as well as the academic excellence and continuous work style. I also gratefully acknowledge Professor Tadashi Fujii for his continuous support in my study and guidance for this thesis.

Second, I also owe a special debt of gratitude to Professor Takaaki Tsurumi, Professor Tadashi Fukuhara, Professor Manabu Iwai for their serious review and valuable suggestions in my thesis. I am also greatly indebted to Dr. Yao Lu for his help in my study and life when I first arrived in Japan. I wish to thank Liqiang Liu, Nan Wei, Yiqin Sun, Yi Zhu, Zhuangkai Wang, Kiyoto Ito as well as other members of the laboratory. Thanks for their assistance and stimulating discussions about my research and for all the fun we have got together in the last several years.

Finally, I would like to express my gratitude to my beloved parents who have always been giving me all the love and supporting without a word of complaint. I should express special appreciation to Xiaoyu Ren for the kindness and patience.

## List of Publications

1. **Tao Zhang**, Tomoaki Karaki and Tadashi Fujii, Effect of  $\text{La}(\text{Nb}_{1/3}\text{Mg}_{2/3})\text{O}_3$  addition on phase transition behavior and energy storage properties of  $\text{NaNbO}_3$  ceramics. **Jpn. J. Appl. Phys.**, 60, SFFC05, 2021.
2. **Tao Zhang**, Tomoaki Karaki and Tadashi Fujii, The preparation of  $\text{MnO}_2$ -doped  $\text{NaNbO}_3$ -based lead-free ceramics with enhanced energy storage performance and attractive electrocaloric effect. **Jpn. J. Appl. Phys.**, 61, SB1028, 2022.
3. **Tao Zhang**, Tomoaki Karaki and Tadashi Fujii, Energy storage performance and electrocaloric effect of lead-free  $\text{NaNbO}_3$ - $\text{La}(\text{Nb}_{1/3}\text{Mg}_{2/3})\text{O}_3$ - $\text{CaZrO}_3$  ceramics. **J. Ceram. Soc. JAPAN**, 130, 875, 2022.